

Coupled Thermal-Hydraulic-Chemical Modelling at the Soultz-sous-Forêts HDR Reservoir (France)

A dissertation submitted to the
SWISS FEDERAL INSTITUTE OF TECHNOLOGY ZURICH
For the degree of

Doctor of Natural Sciences

Presented by

Dominique Bächler
Dipl. Natw. ETHZ
Born July 13, 1975
Citizen of Lenk i/S (BE)

Accepted on the recommendation of

PD Dr. Thomas Kohl, examiner
Prof. Dr. Ladislaus Rybach, co-examiner
Prof. Dr. William Lowrie, co-examiner
Dr. François-David Vuataz, co-examiner
Dr. Albert Genter, co-examiner

ACKNOWLEDGEMENTS

This work would not have been accomplished without the help of many people whom I would like to thank.

First, I would like to thank Thomas Kohl, my supervisor for his guidance and support throughout the project. I greatly benefited much from his wide experience of numerical modelling. At the same time I am much obliged to Prof. Ladislaus Rybach for initiating the Swiss Federal Office for Education and Science (BBW) project, taking over the project co-ordination (until 2001), the generous opportunities I profited from as well as his supportive advice on the interpretation of the results and the nice time in the orchestra. I also thank François Vuataz for refereeing the thesis, taking over the BBW project co-ordination (2001-2004) and the friendly and helpful co-operation. Albert Genter is gratefully acknowledged for accepting to be co-referent and the valuable comments on geology. Also many thanks are given to Prof. William Lowrie for refereeing the thesis.

This study could not have been done without Pierre Durst's work. I appreciated the fruitful co-operation during the common modelling. I also thank Vero Rabemanana for the friendly collaboration. Further, Robert Hopkirk, Keith Evans and Thomas Mégel are warmly acknowledged for the stimulating discussions during the Swiss HDR R&D group meetings.

This work is part of a study funded by the Swiss Federal Office for Education and Science BBW (project no. BBW 98.0008-1 and 00.0453). I would like to thank P. Berlincourt of the BBW for continuous support.

II

I am obliged to Stephen White for providing CHEMTOUGH and his friendly assistance during my stay at Industrial Research Limited (IRL) in New Zealand. In the mean time I thank Nona and Ray Richards very much for the friendly hosting.

Michael Kühn is acknowledged for the support in SHEMAT and the steady exchange of new ideas and results. I thank Sebastian Geiger for his helpful advise in numerical modelling.

I thank in particular D. Pribnow and R. Schellschmidt from the Institute for Joint Geoscientific Research GGA (Hanover, Germany) and SOCOMINE for providing data.

Special thanks are given to Sibylle Steimen for her moral support throughout our mutual years of study. She was always a good listener to any problem.

I would like to thank Sarah Signorelli, Nathalie Andenmatten, Markus Kurmann and Ueli Schärli for the good discussions and for keeping the spirits high in our research group. Significant support was also coming from the technical and administrative personnel of the institute. Special thanks are given to André Blanchard and Elisabeth Läderach as well as to Christoph Bärlocher who kindly supported me in computer problems. Bernard Curtis is warmly acknowledged for proof-reading the thesis.

I thank my parents for their never-ending moral and financial support during my whole studies.

Finally, I thank Nicolas Schwotzer. I am deeply grateful for his support and love.

TABLE OF CONTENTS

<u>ACKNOWLEDGEMENTS</u>	<u>I</u>
<u>1 INTRODUCTION</u>	<u>1</u>
1.1 Geothermal energy	1
1.2 Enhanced Geothermal Systems (EGS)	2
1.3 Aim of this study	6
<u>2 SOULTZ-SOUS-FORÊTS HOT DRY ROCK PROJECT</u>	<u>7</u>
2.1 History and current status of the HDR project	7
2.1.1 Phase 1987-1997	7
2.1.2 Phase 1998-2001	9
2.1.3 Tasks of the current phase 2001-2004	10
2.2 Geological outline	12
2.2.1 Regional geology of the Rhine Graben	12
2.2.2 Structure of the Soultz site	12
2.3 Temperature data, flow field and heat flow	14
2.3.1 Regional temperature- and flow field	14
2.3.2 Temperature- and flow field at Soultz	16
2.4 Geochemical conditions	17
2.4.1 Granitic host rock	17
2.4.2 Composition of reservoir fluid	18
<u>3 IMPACT OF GRABEN-PARALLEL FAULTS ON HYDROTHERMAL CONVECTION – RHINE GRABEN CASE STUDY</u>	<u>21</u>
3.1 The Landau geothermal anomaly	21
3.2 Analytical descriptions of convection in vertical faults	22
3.2.1 Application to Γ -fault in the Landau region	24
3.3 Comparison of analytical solutions and numerical results	27
3.3.1 General considerations	27
3.3.2 Numerical models	28
3.3.3 Results	29
3.4 Numerical model of the Landau geothermal anomalies along the Γ -fault	31
3.4.1 Numerical model	32
3.4.2 Results	34
3.4.3 Discussion	35
3.5 Conclusions and outlook	37

4	CHEMICAL MODELLING	39
4.1	Chemical thermodynamics	39
4.1.1	The equilibrium constant K	40
4.1.2	The saturation index SI	41
4.1.3	pH and alkalinity	41
4.1.4	Activity coefficient	41
4.2	Chemical kinetics	43
4.2.1	Effect of temperature on rates	44
4.3	Thermodynamic model of the Soultz system	45
4.3.1	Calculation of the activity coefficients	45
4.3.2	Modelling of the Soultz formation fluid	46
4.3.3	Mineral formation equations	47
4.4	Kinetic model of the Soultz system	48
4.4.1	Calcite dissolution and precipitation	48
4.4.2	Dolomite dissolution and precipitation	49
4.4.3	Quartz dissolution and precipitation	50
4.4.4	Pyrite dissolution and precipitation	51
5	THE COUPLED CODE FRACHEM	53
5.1	Aim of coupling	53
5.1.1	Governing processes and equations	53
5.1.2	Coupling method	55
5.1.3	Previous fluid-rock interaction studies at Soultz	56
5.1.4	Existing THC coupled codes	57
5.2	FRACTure	58
5.2.1	General	58
5.2.2	Numerical implementation	58
5.3	CHEMTOUGH	60
5.3.1	Original CHEMTOUGH	60
5.3.2	Modified CHEMTOUGH/geochemical FRACHEM module	61
5.4	Coupling FRACTure and CHEMTOUGH to FRACHEM	64
5.4.1	Extension of WinFra	65
5.4.2	Interface	66
5.4.3	FRACHEM	68
5.5	First findings using FRACHEM	70

5.5.1	Thermodynamic calculation of reaction potential of the system	70
5.5.2	1D fracture model with the geochemical module of FRACHEM	70
5.5.3	2D fracture models with FRACHEM	71
6	<u>SENSITIVITY ANALYSES</u>	73
6.1	Numerical model	73
6.1.1	Model geometry, initial- and boundary conditions	73
6.1.2	Hydraulic and thermal model parameters	75
6.1.3	Simulation mode	77
6.2	Model 1: TH coupling	78
6.2.1	Basic model results	78
6.2.2	Geometrical- and time step sensitivity	81
6.3	Model 2: partial THC coupling at equilibrium	82
6.4	Model 3: partial THC coupling	83
6.4.1	Basic model results	83
6.4.2	Sensitivity to time steps	85
6.4.3	Refining the model	87
6.5	Model 4: full THC coupling	88
6.5.1	Basic model results	88
6.5.2	Sensitivity to the amount of fluid flow through the fracture	90
6.6	Conclusions	91
7	<u>BENCHMARK WITH SHEMAT</u>	93
7.1	General	93
7.2	Chemical module of SHEMAT	94
7.3	Numerical implementation	94
7.4	Comparison between FRACHEM and <i>SHEMAT</i>	95
7.4.1	Temperature and pressure field	95
7.4.2	Equilibrium calculations	97
7.4.3	Kinetics	99
7.5	Conclusions	102
8	<u>LONG-TERM RESERVOIR MODEL</u>	105
8.1	Numerical model	105
8.2	Temperature evolution	106
8.3	Chemical processes	107
8.3.1	Carbonate dissolution and precipitation	107

8.3.2	Quartz precipitation	110
8.3.3	Pyrite precipitation	110
8.3.4	Amount of dissolved and precipitated minerals	111
8.4	Evolution of porosity and permeability	114
8.5	Pressure evolution and fluid velocity	116
8.6	Application to 1997 circulation test	117
8.7	Conclusions	120
9	CONCLUSION AND OUTLOOK	123
	REFERENCES	129
	APPENDIX A	139
	FRACHEM MANUAL	141
	Format and building of FRACHEM input files	141
	Input.dat	141
	chem.dat	142
	chem_input.dat	143
	Format of FRACHEM output files	143
	output.dat	143
	disX.dat	143
	advX.dat and hflX.dat	143
	chem_output.dat	144
	mon_node_elX.dat	144

Table A: Alphabetical list of used variables and their units. The chapter number is indicated for variables that are used in different context.

acronym	description	unit	chapter
A	constant depending on temperature and the dielectric constant of the solvent; ~ 0.51 in water at 25°C .	-	
A_i	interface area between two neighbouring elements	m^2	
a_k	fracture aperture	m	
a_i	activity of a species i	-	
B(I)	second virial coefficient	-	
Cr	Courant number	-	
c_{pf}	fluid heat capacity	J/kgK	
c_{pm}	matrix heat capacity	J/kgK	
C_i	concentration of a species i	mol/kg	
D_i	diffusion coefficient	m^2/s	
E_{act}	activation energy	J	
∇F_{in}	variation of $Q_{t_{in}}$ due to transport	-	
g	gravity constant	m/s^2	
G	geothermal gradient	K/m	3
ΔG	variation of Gibbs free energy of reaction	J	4
ΔG°	variation of standard Gibbs free energy	J	4
ΔH	variation of enthalpy of reaction	J	4
ΔH°	variation of standard enthalpy	J	4
H	fracture height	m	3
i	name of a species	-	
I	ionic strength	-	
k_B	Boltzmann's constant ($1.380658 \cdot 10^{-23}$)	J/K	
K	equilibrium constant	-	4
K	hydraulic conductivity	$\text{m}^2/\text{Pa} \cdot \text{s}$	5,6,7,8
K_k	hydraulic conductivity of the fracture	$\text{m}^2/\text{Pa} \cdot \text{s}$	
k	permeability	m^2	

acronym	description	unit	chapter
ΔL	length of an element	m	
L	fracture depth	m	3
L	fracture length	m	3
$M_{i,E}$	amount of dissolved or precipitated mineral i in element E	kg	
m	empirical constants	-	4
m	number of convection cells in x direction	-	3
m_i	mole fraction	-	
MW	molecular weight	kg/mol	
n	number of convection cells in z direction	-	3
n^*	number of convection cells in z direction at Rc^*	-	3
n	empirical constant	-	4
n	norm of the element interface	-	5
N	number of the species	-	
Pe	Peclet number	-	
P	pressure	Pa	
pH	pH value	-	
∇P	pressure gradient	Pa/m	
q_{tot}	total fluid production rate	m^3/s	
q_{inj}	fluid injection rate	m^3/s	
q_i	chemical source	-	
q_H	heat source	W/m^3	
Q	reaction quotient	-	
$Q_{t_{in}}$	quantity of component i (water, steam, gas or heat)	-	
qr_{in}	variation of $Q_{t_{in}}$ due to reactions	-	
R	ideal gas constant (8.31451)	J/mol*K	4
R	Rayleigh number	-	3
R_c	critical Rayleigh number	-	3
R_c^*	minimal critical Rayleigh number	-	3
r	reaction rate	mol/m^3*s	

acronym	description	unit	chapter
r_d	dissolution rate	$\text{mol/m}^3 \cdot \text{s}$	
r_p	precipitation rate	$\text{mol/m}^3 \cdot \text{s}$	
$r_{i,n}$	reaction rate of mineral i at time n	$\text{mol/m}^3 \cdot \text{s}$	
SI	saturation index	-	
S_c	storativity	1/Pa	
ΔS_r	entropy of reaction	J/K	
ΔS_r°	standard entropy of reaction	J/K	
s	mineral surface	m^2/m^3	
T	temperature	$^\circ\text{C}$	
t_D	delay time	s	
T_0	initial temperature	$^\circ\text{C}$	
T_{inj}	injection temperature	$^\circ\text{C}$	
ΔT	temperature difference	$^\circ\text{C}$	
t	time	s	
Δt	time step	s	
t_0	initial time	s	
t_{tot}	total time	s	
Tr_{tot}	total transmissivity	$\text{m}^3/\text{Pa} \cdot \text{s}$	
Tr	transmissivity	$\text{m}^3/\text{Pa} \cdot \text{s}$	
Tr_k	fracture transmissivity	$\text{m}^3/\text{Pa} \cdot \text{s}$	
v	velocity	m/s	
v_f	fluid velocity	m/s	
v_a	buoyancy velocity	m/s	
v_i	stoichiometric coefficients of the reaction	-	
V_E	volume of element E	m^3	
W_w	water mass	kg/mol	
W	fault width	m	3
z	depth	m	
z_i	charge of ionic species i	-	
α	thermal expansion coefficient	1/K	3
β_f	the thermal expansion coefficient	1/K	
γ	activity coefficient	-	

acronym	description	unit	chapter
γ_i	activity coefficient of a species i	-	
κ_m	porous medium thermal diffusivity	m^2/s	
κ_r	porous medium thermal diffusivity	m^2/s	
λ	thermal conductivity	$\text{W}/\text{m}\cdot\text{K}$	
λ_r	rock thermal conductivity	$\text{W}/\text{m}\cdot\text{K}$	
λ_f	fluid thermal conductivity	$\text{W}/\text{m}\cdot\text{K}$	
λ_m	matrix thermal conductivity	$\text{W}/\text{m}\cdot\text{K}$	
μ	dynamic viscosity	$\text{Pa}\cdot\text{s}$	
μ_i	chemical potential of species i	-	
μ_i°	standard chemical potential of species i	-	
ρ_0	initial fluid density	kg/m^3	
ρ	density	kg/m^3	
ρ_f	fluid density	kg/m^3	
ρ_m	matrix density	kg/m^3	
τ	tortuosity of the medium		
Φ	porosity	-	5,6,7,8
Φ	heat transfer function	-	3
ω	convection growth rate	$1/\text{s}$	
$\Psi(\text{I})$	third virial coefficient	-	

Abstract

The present study is part of the European concerted action for the support of the HDR geothermal energy R&D activities at Soultz-sous-Forêts (Alsace, France) from 1998-2001 and 2001-2004 representing one of the Swiss HDR R&D group's contributions. It was funded by the Swiss Federal Office for Education and Science and carried out in close co-operation with the Centre of Hydrogeology at the University of Neuchâtel (CHYN) in Switzerland. The aim of the study was to investigate thermal-, hydraulic- and chemically coupled processes and their impact on the Soultz HDR reservoir.

The regional and local temperature distribution in the Rhine Graben was investigated, in order to link the Soultz HDR site to a wider geological context. The study highlights the impact of the graben-parallel faults on the hydrothermal convection. In addition, it was found that the graben-perpendicular fluid flux is negligible compared to the graben-parallel flux. This has to be taken into account when investigating temperature anomalies in the Rhine Graben. Moreover, such graben-wide features are important when delineating the general framework for HDR energy use at Soultz.

The numerical code *FRACHEM* was developed, to simulate coupled thermal-, hydraulic- and chemical processes, accounting for the Soultz specific conditions such as the high salinity of the reservoir fluid and the high temperatures. This was based on the codes *FRACTure* and the geochemical module of *CHEMTOUGH*. *FRACTure* calculates the thermal and hydraulic and the geochemical module the chemical processes. An interface links both parts. According to the characteristics of the Soultz HDR reservoir, the geochemical module was modified: 1) the Debye-Huckel approach was replaced by the Pitzer formalism to calculate the activity coefficients, accounting for the high salinity of the fluids. 2) New kinetic laws for calcite, dolomite, quartz and pyrite were implemented. These also required modifying the calculations of the reaction surface. 3) The porosity-permeability relation was replaced by a new relation for fractured rock. 4) The possibility of re-injecting the produced fluid was implemented. The sequential-non-iteration approach (SNIA) was used to couple transport and reactions.

Sensitivity analyses that were conducted to test the numerical behaviour of *FRACHEM*, proved its proper functionality but highlighted the sensitivity of the SNIA approach to time steps. To quantify the *FRACHEM* results, a comparative

simulation with the code *SHEMAT* was conducted, which validated *FRACHEM*: setting up appropriate numerical models results in comparable fluid velocities and temperature behaviour as well as thermodynamic equilibrium concentrations, indicating that the Pitzer approach is well implemented. Assuming an adequate initial calcite reaction rate in the *SHEMAT* model results in a good fit. The only major difference between the two codes is the implemented porosity-permeability models resulting different porosity and permeability values.

Coupled thermal-, hydraulic- and chemical processes in a fractured zone in the Soultz reservoir at 3'500 m ($T_{ini}=165^{\circ}\text{C}$), which occur due to the injection of fluid ($T_{inj}=65^{\circ}\text{C}$) at one end of the zone and the production at the other end, were modelled for 2 years. Calcite and dolomite are dissolved and quartz and pyrite are precipitated near the injection point. Calcite precipitates towards the production point. In the whole reservoir ($\sim 560'000\text{ m}^3$) a total of 990 kg (3.6% of the initial amount) calcite are dissolved and 1'180 kg (4.3% of the initial amount) are precipitated during 2 years. 100 kg (1.5% of the initial amount) dolomite is dissolved. Only 0.05 kg quartz and 0.01 kg pyrite are precipitated. Calcite is the most reactive mineral and therefore, the porosity and permeability evolution, results from the calcite reactions: near the injection point, the porosity and the permeability increase and near the production well they decrease. At the end of the simulation, the maximum porosity is 14.8 % and the minimum is 6.8 %, down from initially 10 %. The maximum permeability after 2 years is $2.1 \cdot 10^{-11}\text{ m}^2$ and the minimum is $3 \cdot 10^{-12}\text{ m}^2$, down from initially $6.8 \cdot 10^{-12}\text{ m}^2$. The system seems to be very close to steady state. Therefore, it can be demonstrated, that mineral dissolution and precipitation during the circulation of the fluid in the reservoir do not represent a limiting factor on the HDR reservoir (at 3'500 m depth) performance at the Soultz site. To test the results of the long-term model, the numerical transmissivity was compared to the transmissivity of the 1997 circulation test. The fact that the transmissivity decreases during the circulation test, when thermo-mechanical effects are factored out, points to geochemical processes in the reservoir such as the precipitation of calcite. The pressure evolution in the reservoir is therefore the result of interactions between thermo-mechanical and geochemical processes. These findings highlight the importance of thermal, hydraulic and chemically coupled HDR reservoir models. The integration of geochemical considerations is therefore indispensable for integrated simulations of HDR systems and predictions of its performance.

Zusammenfassung

Die vorliegende Studie wurde im Rahmen der europäischen R&D Aktivitäten zwischen 1998-2001 und 2001-2004 des HDR Projekts bei Soultz-sous-Forêts im Elsass in Frankreich durchgeführt. Finanziert wurde die Arbeit durch das Bundesamt für Bildung und Wissenschaft (BBW). Sie ist Teil der Beiträge der Schweizer HDR R&D Gruppe und entstand in enger Zusammenarbeit mit dem Zentrum für Hydrogeologie der Universität Neuenburg (CHYN) in der Schweiz. Das Ziel der Studie war die Untersuchung der thermisch-, hydraulisch- und chemisch gekoppelten Prozesse und deren Einfluss auf das HDR Reservoir bei Soultz.

Um den HDR Standort Soultz in einen grösseren geologischen Zusammenhang zu bringen, wurde die regionale und lokale Temperaturverteilung im Rheingraben untersucht. Die Studie zeigt den grossen Einfluss der graben-parallelen Brüche auf die hydrothermale Konvektion. Zusätzlich verdeutlicht sie, dass der graben-normale Fluidfluss gegenüber dem graben-parallelen Fluss vernachlässigbar ist. Dies muss bei zukünftigen Untersuchungen von Temperaturanomalien im Rheingraben mit in Betracht gezogen werden. Überdies erweisen sich solche graben-umspannende Eigenschaften als wichtige Rahmenbedingungen für die HDR Energieerzeugung.

Für die Simulation thermisch-, hydraulisch- und chemisch gekoppelter Prozesse wurde der numerische Code *FRACHEM* entwickelt, basierend auf dem Code *FRACture* und dem geochemischen Modul aus dem Code *CHEMTOUGH*. Eine Schnittstelle verbindet die beiden Teilstücke. Das geochemische Module aus *CHEMTOUGH* wurde angepasst, um den hohen Temperaturen und Salinitäten der Soultz Fluide Rechnung zu tragen: 1) Zur Berechnung der Aktivitätskoeffizienten hochsaliner Fluide der Debye-Huckel Ansatz durch die Pitzer Gleichungen ersetzt worden. 2) Neue kinetische Gesetze für Kalzit, Dolomit, Quarz und Pyrit wurden eingeführt. 3) Das herkömmliche Porosität-Permeabilität Modell wurde ersetzt durch eines für geklüftetes Gestein. 4) Zusätzlich ist die Möglichkeit vorgesehen, gefördertes Fluid wieder zu injizieren. Die Kopplung von Transport und Reaktion wurde mittels sequentiell, nicht iterativen Ansatz (SNIA) realisiert.

Um das numerische Verhalten von *FRACHEM* zu testen, wurden Sensitivitätsanalysen durchgeführt. Die Resultate bestätigen die korrekte Funktionsweise des Codes und unterstreichen die Sensitivität des SNIA Ansatzes gegenüber Zeischrittgrössen. Zur quantitativen Bestimmung der *FRACHEM* Resultate

wurde ein Vergleichstest mit dem Code *SHEMAT* durchgeführt. Dieser validierte *FRACHEM*: Mit dem passenden numerischen Modell resultieren vergleichbare Fluidgeschwindigkeiten, Temperaturen und thermodynamische Gleichgewichtskonzentrationen, was die korrekte Einführung der Pitzer Gleichungen bezeugt. Auch die kinetischen Berechnungen werden bestätigt, wenn die anfänglichen Reaktionsraten angemessenen sind. Der einzige grosse Unterschied in den beiden Codes sind die Porosität-Permeabilität Modelle, die zu unterschiedlichen Porositäten und Permeabilitäten führen.

Thermisch-, hydraulisch- und chemisch gekoppelte Prozesse in einer geklüfteten Zone im Soultz Reservoir in 3'500 m Tiefe ($T_{ini}=165^{\circ}\text{C}$), hervorgerufen durch Fluidinjektion ($T_{inj}=65^{\circ}\text{C}$) am einen Ende der Zone und Produktion am anderen Ende, wurden für einen Zeitraum von 2 Jahren simuliert. Bei der Injektion werden Kalzit und Dolomit aufgelöst, während Quarz und Pyrit ausgefällt werden. In Richtung Produktion wird Kalzit ausgefällt. Im ganzen HDR Reservoir ($\sim 560'000\text{ m}^3$) wird in den 2 Jahren total 990 kg (3.6% der anfänglichen Menge) Kalzit aufgelöst und 1'180 kg (4.3% der anfänglichen Menge) ausgefällt. 100 kg (1.5% der anfänglichen Menge) Dolomit wird aufgelöst. Nur 0.05 kg Quarz und 0.01 kg Pyrit werden ausgefällt. Kalzit ist das reaktivste Mineral und ist daher verantwortlich für die Entwicklung der Porosität und der Permeabilität: Bei der Injektion nehmen Porosität und Permeabilität zu und bei der Produktion verringern sie sich. Am Ende der Simulation ist die Porosität maximal 14.8% und minimal 6.8% ($\Phi_0=10\%$), während die Permeabilität maximal $2.1 \cdot 10^{-11}\text{ m}^2$ und minimal $3 \cdot 10^{-12}\text{ m}^2$ ist ($K_0=6.8 \cdot 10^{-12}\text{ m}^2$). Das System scheint nahe dem Gleichgewichtszustand zu sein. Es steht daher fest, dass die Auflösungs- und Ausfällungsreaktionen während der Fluidzirkulation im Reservoir (in 3'500 m Tiefe) für das HDR System keine limitierende Faktoren sind. Zur Überprüfung der Resultate, wurde die numerisch berechnete Transmissivität mit der Transmissivität vom Zirkulationstest von 1997 verglichen. Wird von den thermo-mechanischen Prozessen abgesehen, ist die Abnahme der Transmissivität in den Messdaten ein Hinweis auf geochemische Prozesse im Reservoir. Die Druckentwicklung im Reservoir ist daher das Resultat der Kombination von thermo-mechanischen und geochemischen Prozessen. Die Integration geochemischer Prozesse ist demzufolge für ganzheitliche Untersuchungen von HDR Systemen und deren Verhalten unerlässlich.

1 INTRODUCTION

1.1 GEOTHERMAL ENERGY

Energy stored in the earth in the form of heat is called geothermal energy. The heat originates from different sources: the decay of natural radioactive isotopes, original heat from the formation of the earth and gravitational energy released during the formation. On an average, the temperature increases 3 °C for each 100 m from the surface towards earth's centre. Since 99 % of the earth is hotter than 1000 °C, it provides a virtually inexhaustible heat potential.

Where hot thermal sources of vapour naturally appear on the earth's surface, geothermal energy has been used for a long time. Nowadays, thanks to different specifically developed techniques, geothermal energy can be used in many places, for numerous applications. Figure 1-1 shows different geothermal systems: Borehole Heat Exchangers (BHE) extract heat from ambient rock formation by circulating water in the shallow subsurface (<300 m depth). Such systems are used for house heating or cooling and hot water supply. Heat exchanger pile systems are employed where 'soft' foundation soil requires piles to support the construction load. Equipped with a channel system to circulate fluid within the subsurface, the foundation piles exchange heat with the surrounding ground for heating or cooling. Aquifer systems extract heat from geothermal groundwater at greater depth (~3 km) and are utilized for district heating of whole housing areas, fish farm heating, greenhouse heating and process heat. Heat is extracted to produce power by Enhanced Geothermal Systems (EGS). In the next chapter, these systems are discussed in more detail.

Compared to conservative energy sources, the use of geothermal energy has numerous advantages: it is always and everywhere available. No CO₂ or dust particles are released during the operation of geothermal systems and therefore they are a valid

substitute for fossil fuels. In addition, no radioactive waste is produced. Furthermore, geothermal installations only need little space and keep a low profile on the earth surface. Thus, geothermal energy is a vital part of a sustainable future.

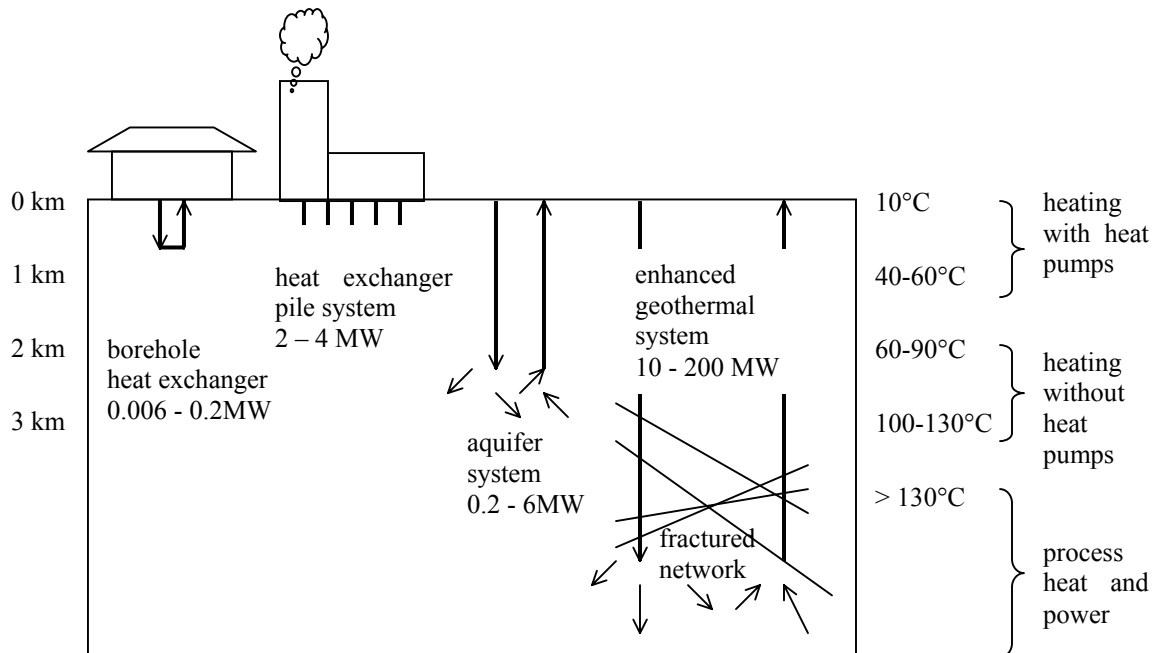


Figure 1-1: Geothermal systems: borehole heat exchanger, heat exchanger pile system, aquifer system and enhanced geothermal system.

1.2 ENHANCED GEOTHERMAL SYSTEMS (EGS)

Only a very small part of the earth's respectable geothermal potential is used for power generation. The 'World Energy Conference' estimates the potential for geothermal power production to be 10^{12} MWh. This is tenfold the world's annual energy consumption. Yet power production from geothermal energy is only a tiny fraction of the global production. Conventional geothermal power generation is restricted to areas where the earth's crust is relatively thin, water is available in rock formations and sufficient hydraulic pressure present (i.e. Iceland, Western USA, New Zealand and Italy). Under such conditions geothermal energy production is already economic now. To make geothermal heat accessible for less privileged regions too, a new technology comes into operation: the Hot Dry Rock (HDR) Technology. At the beginning HDR technology was invented with the objective of injecting fluid into dry fractured rock systems. The lack of formation fluids turned out to be disadvantageous. In today's target rock systems, formation fluid is present and the technology is

therefore more often called Hot Wet Rock (HWR), Hot Fractured Rock (HFR) or Enhanced Geothermal Systems (EGS). Below, the term HDR is used throughout.

The principles of an HDR system are illustrated in Figure 1-2. An injection pump squeezes water through a deep well into an artificially enhanced fractured rock system. The fluid is heated, depending on the depth and the dominant temperature, up to about 200°C and a production pump pulls it up to the surface again. The heat exchanger extracts the energy from the hot fluid to produce power via a steam turbine. The excess heat remaining can be used in a district-heating network. A cooling system operates after the generator to condensate the steam. The HDR process is a closed system where the produced fluid is re-injected and therefore only little fluid has to be replaced from a reservoir.

To reach a reasonable degree of efficiency (turbine) the rock temperature has to be at least 200°C and therefore, the fluid temperature at the wellhead reaches 180°C. Thus, depending on the local temperature gradient, the injection and the production well have to be drilled accordingly (~5 km). The fractured rock system is created by hydraulic stimulation: water is injected at a high pressure (several MPa) into the wells. This can cause pre-existing but closed fractures to open and also new fractures to develop. Existing shear stress displaces rocks and thus, the fractures also stay open after injection. Seismic signals released during the fracturing are continuously monitored through observation wells and give information on the development of the heat reservoir in space and time. Further injection and production wells can then be drilled accordingly.

HDR technology is still under development and at present, there is no system in operation. Therefore, only rough assumptions can be given on the reservoir size: usually, an average heat exchanging area of around 1.5 km² and a reservoir volume of about 5*10⁸ m³ is assumed. Such a system is estimated to generate 3 MW_{el} and 20 MW_{th} power and correspondingly 20'000 MWh_{el} and 90'000 MWh_{th} energy per year. This corresponds to an energy demand of around 5'000 one-family houses. Figure 1-3 shows the energy flow chart. The system should run for around 20-30 years. Clearly, these values depend on the reservoir geometry and the flow field and vary with each site.

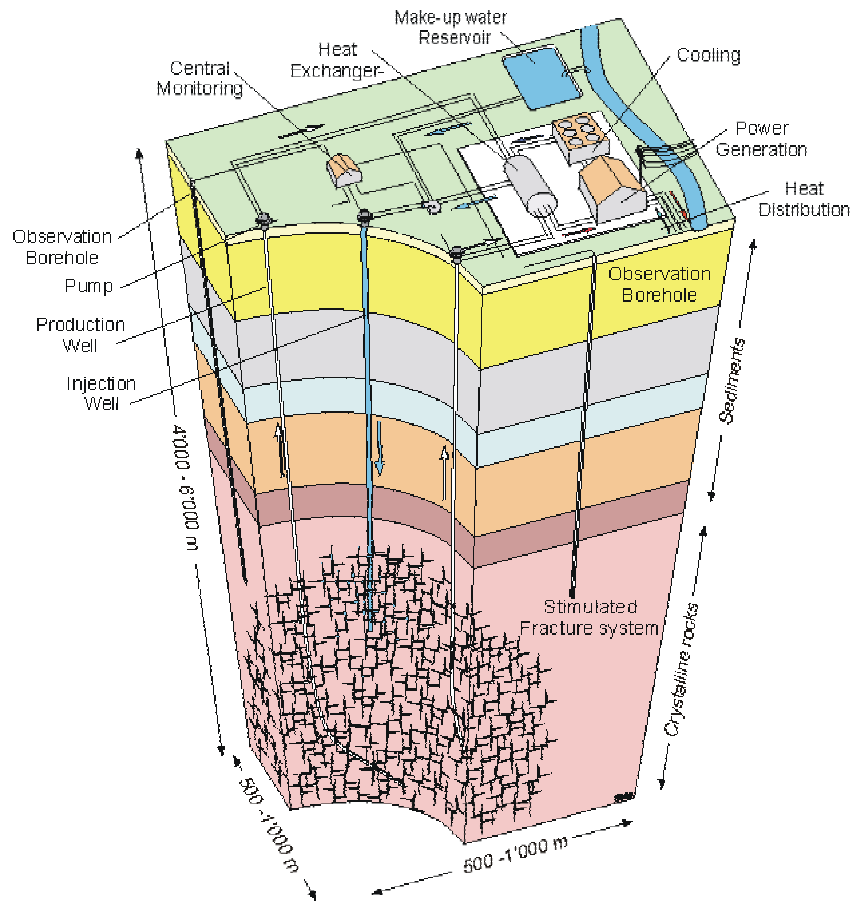


Figure 1-2: Schematic illustration of a HDR system (from www.dhm.ch).

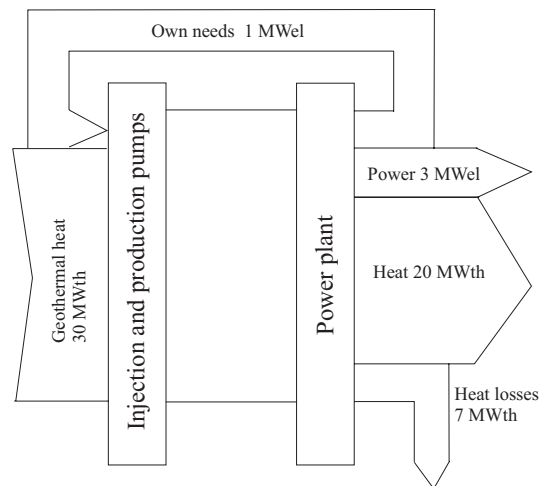


Figure 1-3: Energy flow chart of a HDR system.

The first HDR project started in 1970 in Fenton Hill, USA. The site was located in a caldera with very high temperature gradients (60 K/km). The project was running till 1996 when it was stopped due to the lack of funding. However, the feasibility of the

HDR technology was proved during this project: a running system was developed consisting of two 3.6 km deep wells 380 m apart. Connection of the two wells was achieved through hydraulic stimulation. Several tests showed that there is only a minor loss of fluid during circulation, flow resistances are low, temperatures are high enough for power generation and no significant temperature decrease occurs. The UK-project at the Rosemanowes Quarry in Cornwall in a granitic pluton, which ran from 1977 to 1992, was the second such project to be initiated and has produced a lot of new information about deep crystalline rock masses and techniques to investigate them. However, because the geological situation was not qualified for the commercial use of geothermal energy, the project was stopped. Several minor projects followed, such as the ones at Le Mayet de Montagne in France (1978-1989), at Fjällbacka in Sweden (1984-1990), at Ogachi and Hijiori (1987-2002) in Japan and at Falkenberg (1978-1983) and Bad Urach in Germany (1977-1990). Most of these projects stopped because of lack of funding. They provided a lot of very important information, which will be helpful for the future projects.

At present there are projects at Soultz-sous-Forêts in France, at Basel in Switzerland and in the Hunter Valley in Australia, which is still in the planning phase. The Soultz project began in 1987 and is the most successful site. Since this site is the target of this study it is discussed separately in the next chapter. In 1996 the Swiss HDR project called Deep Heat Mining (DHM) started. A HDR system consisting of one injection and two production wells is planned. Since centres of population, such as the city of Basel, are nearby, excess heat remaining after power generation will be fed into existing heat distribution networks. Drilling operations for a first exploration borehole started in 1999. Unfortunately, successive drilling problems stopped the penetration at 1537 m. A new drilling programme has been set up, including a more powerful drilling rig, as well as larger borehole and casing diameters. In June 2001 the crystalline basement was reached at 2755 m. Temperature logs revealed a geothermal gradient of 40 K/km, which is slightly above the forecast. As soon as new funding is found, a 5000 m deep borehole will be drilled. The production of power will start in 2009.

Until now there is no HDR site commercially running. Although the feasibility has been shown, further scientific investigations such as the present study have to be undertaken to improve the technology.

1.3 AIM OF THIS STUDY

Geothermal reservoir fluids are often highly saline (i.e. Wairakei geothermal field, New Zealand; Salton Sea geothermal field, California USA) leading to mineral precipitation at the earth's surface during power generation due to temperature and pressure changes. Thus, an important consequence of the storage and transport of heat and fluids in rocks is that they may give rise to significant coupling between thermal, hydrological and chemical (THC) processes. Such coupled processes can significantly affect the performance of structures and engineering operations in rocks. Dissolution and precipitation of minerals are affected by temperature and hydraulics, and can result in significant changes in permeability and solute transport. Understanding of these couplings is important for geothermal reservoir engineering. This study aims at predicting the long-term behaviour of the HDR reservoir at Soultz by investigating these coupled processes.

In chapter 2 the Soultz HDR test site is introduced. The development of the project is summarised and geology, thermal, hydraulic and geochemical conditions are described. To link the Soultz HDR site to a wider context, the local and regional temperature distribution in the Rhine Graben is investigated. In particular its typical north-south permeability structures and their impact on hydrothermal convection are detailed and described in chapter 3. A basic introduction into geochemistry is given in chapter 4. The development of the new code FRACHEM to simulate coupled processes is discussed in chapter 5. To test the code's capability, sensitivity studies are carried out and a comparison with another similar code called SHEMAT is undertaken (chapter 6 and 7). Chapter 8 investigates the results of the Soultz reservoir long-term behaviour taking into account thermal, hydraulic and chemical processes. Finally, chapter 9 summarises the main results and makes some suggestions of the future work.

This study is part of the European concerted action for the support of the HDR geothermal energy R&D activities at Soultz-sous-Forêts from 1998-2001 and 2001-2004 (EC contracts no. JOR3-CT98-0313 and ENK5-CT2000-00301) representing one of the Swiss HDR R&D group's contributions. It was funded by the Swiss Federal Office for Education and Science (no. 98-0008-1 and 00.0453) and carried out in close co-operation with the Centre of Hydrogeology at the University Neuchâtel (CHYN) in Switzerland.

2 SOULTZ-SOUS-FORÊTS HOT DRY ROCK PROJECT

2.1 HISTORY AND CURRENT STATUS OF THE HDR PROJECT

The European HDR research site at Soultz-sous-Forêts started in 1987. The site was selected because high heat flow was observed during former oil exploration in this region (Gérard & Kappelmayer, 1989). France, Germany and the European Commission (EC) funded the Soultz HDR project. Organisations from other countries such as Italy, Sweden, United Kingdom and Switzerland were also involved. The company SOCOMINE managed the project until 2001, when the European Economic Interest Grouping E.E.I.G (BESTEC (G), Electricité de France (F), Electricité de Strasbourg (F), Ente Nazionale per l'Energia Elettrica (I), Pfalzwerke AG (G), Shell International Exploration and Production B.V. (NL)) took over the management under a new contract with the European Commission for the period of 2001-2004.

2.1.1 Phase 1987-1997

The following list gives an overview on main activities during 1987-1997¹.

1987-1989 The first well GPK1 was drilled to a depth of 2000 m. Crystalline basement was encountered at 1400 m depth. The bottom hole temperature was 140.3°C. In the sedimentary cover high temperature gradients (100 K/km) and heat flow values were measured (176 mW/m²). In the granitic basement the values are decreased (30 K/km, 82 mW/m²) (Schellschmidt & Schulz, 1991).

¹ Detailed information can be found at <http://www.soultz.net>

- 1989-1991 EPS1, an old oil well, was re-opened and deepened to 2230 m. A continuous core was drilled, which provided important information especially on the joint network and the mineralogy.
- 1992-1993 GPK1 was extended to 3590 m. During, and after the drilling, numerous geophysical measurements were carried out to assess rock conditions. Also large-scale hydraulic tests, microseismic logging and fluid sampling were carried out (Baria, 1995).
- 1994 GPK1 was put on production to measure the productivity and the injection properties after the massive injections in 1993 (Baria, 1995). The information gained was used to target a second well GPK2 about 450 m south of GPK1. Temperatures $>168^{\circ}\text{C}$ were measured at the bottom of the well at 3890 m. Figure 2-1 illustrates an aerial view of the platform of GPK2. The GPK1 platform is also seen in the background.
- 1995-1996 GPK2 was stimulated with a maximum flow of 78 l/s to improve the injectivity (Gérard et al., 1997). A total volume of $28'000\text{ m}^3$ of fluid was injected between 3200 m and 3600 m in three steps (24, 45 and 78 l/s). At 78 l/s a maximum wellhead pressure of 13 MPa resulted.
- 1997 A forced circulation test of four months duration was carried out. This demonstrated that it is possible to circulate, continuously between GPK1 and GPK2 in a depth range of 3200 m to 3700 m, about 25 l/s of fluid at a temperature $>140^{\circ}\text{C}$ without any fluid losses and requiring only 250 kWe pumping power compared with the thermal output of 10 MWth. The pressure difference between injection- and production point was $\sim 6\text{ MPa}$ (see chapter 8).

All activities during this phase led to an extended improvement of knowledge and required technologies at the scale of the performed tests such as:

- Economical drilling performance through hard, hot and deep rocks
- Stimulation and development of hot and very large volumetric reservoirs
- Engineering for development/production adapted to Hot Dry Rock exploitation.

Even though the performance obtained at Soultz is a significant advance on results achieved within the framework of previous experiments at other sites, they have relied

on the continuous transfer of know-how from teams involved in earlier work and who now form part of the Soultz group.

Based on the encouraging results of the circulation test of 1997, the programme for the subsequent phase 1998-2001 was defined.



Figure 2-1: Aerial view of the platform of GPK2/3/4 with the actual drilling activities. A part of the GPK1 platform is seen in the background (credit photo, Jean-Luc Nachbauer, Les films de l'Europe).

2.1.2 Phase 1998-2001

The 1997 circulation test yielded excellent results. But to produce electricity at an economic rate, the reservoir fluid should achieve a temperature of $\sim 200^{\circ}\text{C}$. Therefore, it was decided to extend GPK2 to 5000 m where temperatures of 200°C were expected. The following activities were undertaken during 1998-2001:

1999 GPK2 was successfully deepened to 5084 m depth. This also included the removal of the existing casing, cementing, reaming out from 6.25" to 8.5" and anchoring the 4200 m casing. New high temperature cement and new metal packers allowed a successful completion of the new GPK2. The target temperature of 200°C was measured at a depth of 4950 m. A bottom hole core was taken at 5048-5051 m depth. To measure the in situ stress a pilot hole was drilled from 5051-5084 m depth. An additional microseismic monitoring well OPS4 was deepened to 1500 m depth and instrumented to improve the accuracy of microseismic event locations.

2000-2001 Hydraulic stimulation tests were performed. The measurement of the initial, natural injectivity of around 0.2 l/MPas in the new deep part of GPK2 was consistent with the observations in the depth range of 3200-3800 m and indicated that a reservoir could possibly be developed at a depth of 4500-5000 m.

The stimulation of the new GPK2 in 2000 showed the following results:

- Starting the stimulation at high flow rates and heavy brines initiated and developed fluid inlets/exits at the greatest possible depth in GPK2
- The overpressure needed to create the large reservoir was lower than anticipated
- The new reservoir at 5000 m showed closer boundaries compared to the upper reservoir at 3000-3600 m
- No leak-off to the upper reservoir was detected
- The reservoir extends along NNW/SSE, about 500 m wide, 1500 m long and 1500 m high.

GPK2 is planned as a production well for the scientific pilot plant. The fact that the majority of the fluid left the open hole during stimulation at the bottom is very encouraging, since it can be anticipated that most of the produced fluid enters the well at around 195-200°C.

2.1.3 Tasks of the current phase 2001-2004

The planned scientific pilot plant module is a 3-well system consisting of one injector and two producers, one on each side of the injector. All wells are drilled from a single platform using the existing deep well GPK2 as one of the producers. Figure 2-2 illustrates the future HDR system. The predominant operational tasks of the current phase are:

Task 1: Drilling of GPK3	Drilling of the deviated well GPK3 starting 6 m from the wellhead of GPK2 to 5000 m depth into a target zone selected from the stimulation carried out in 2000. The bottom of this new well will be separated from the bottom of GPK2 by around 600 m.
--------------------------	--

- | | |
|-----------------------------|--|
| Task 2: Stimulation of GPK3 | Stimulation of the bottom part of GPK3 (and if necessary GPK2) to extend the existing reservoir of GPK2 by an overlapping volume of enhanced permeability. |
| Task 3: Drilling of GPK4 | Drilling of the deviated well GPK4 from the same platform as GPK2 and GPK3 to 5000 m depth into a target zone selected from the stimulation of GPK3. The bottom of this new well will be separated from the bottom of GPK3 also by around 600 m. |
| Task 4: Stimulation of GPK4 | Stimulation of the bottom part of GPK4 to extend the existing reservoir of GPK2 and GPK3 by an overlapping volume of enhanced permeability. |

Beside these activities hydraulic, thermal and geochemical measurements, as well as modelling of coupled processes, will be carried out to help characterise the reservoir and its performance.

The present project status is still task 1. Drilling operations for GPK3 were finished in November 2002. Bore hole televiwer (BHTV) logs were done showing that the new reservoir is highly fractured. Further logs will be measured until March 2003, when stimulation of GPK3 is planned.

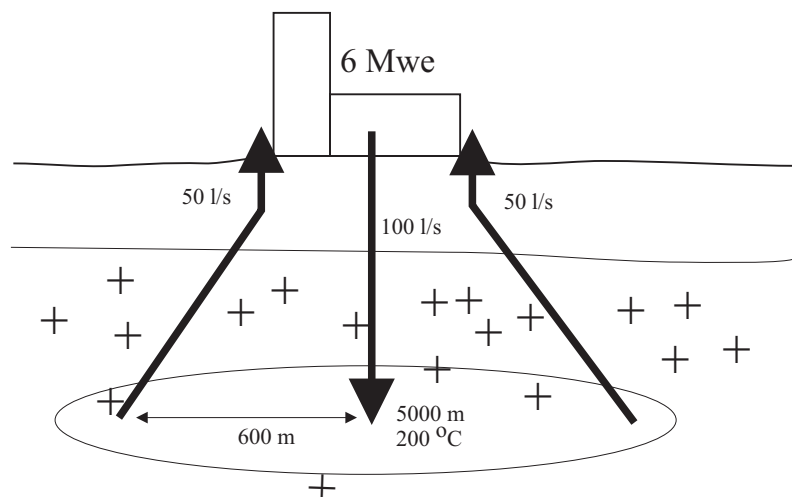


Figure 2-2: Schematic illustration of future HDR system at Soultz.

2.2 GEOLOGICAL OUTLINE

2.2.1 Regional geology of the Rhine Graben

Soultz-sous-Forêts is located about 50 km north of Strasbourg in the NNE-SSW striking Rhine Graben between the Vosges and Black Forest mountains to the East and West, respectively (Figure 2-3). The Rhine Graben forms the central part of the great Western European rift zone from the Mediterranean to the North Sea and Scandinavia. It extends northward 300 km from Basel (Switzerland) to Frankfurt (Germany) with a width of 30 to 40 km. The structure was formed in the Tertiary about 45-60 Ma ago by up-doming of the crust-mantle boundary due to magmatic intrusions at 80-100 km depth (Illies, 1965). This formation was accompanied by extensive escarpment erosion and sedimentation of that eroded material into the Graben trough. The Graben's tectonic structure is characterized by prominent north-south striking faults and kilometre wide horsts and grabens. Its major faults reach into the crystalline basement (Rousset et al., 1992) and follow the lateral borders of the Graben.

2.2.2 Structure of the Soultz site

The targeted heat exchanger, the porphyritic granite basement, has its top at Soultz at 1400 m depth (Gérard & Kappelmeyer 1991). It is of Visean age (~350 Ma) and directly overlain by Buntsandstein sandstone, Muschelkalk limestone and a thick pile of less permeable sediments (Keuper, Jurassic, Oligocene). Within a wide depth range the granite is highly fractured and permeable (Kohl et al., 1999) and natural as well as injected fluids are circulating within the fractured zones (Genter & Traineau, 1992).

Figure 2-4 shows the lithology in a geological cross section.

The Soultz site corresponds to a local horst structure (Genter & Traineau, 1996) with a lateral elevation of ~500 m. The topmost part of the horst and its cover are traversed by several large fault systems parallel to the Graben shoulder, which are well known from oil exploration wells and partly even visible on the surface morphology.

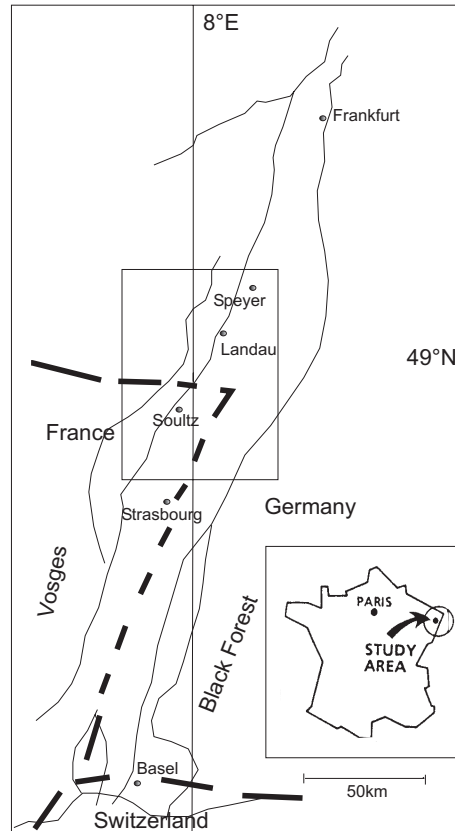


Figure 2-3: Location of Soutz in the Rhine Graben. The black lines mark the major fault and the dashed lines the borderlines (modified after Brinkmann, 1972). The locations of the faults are extracted from Illies (1965)). The rectangular area is shown in Figure 2-5.

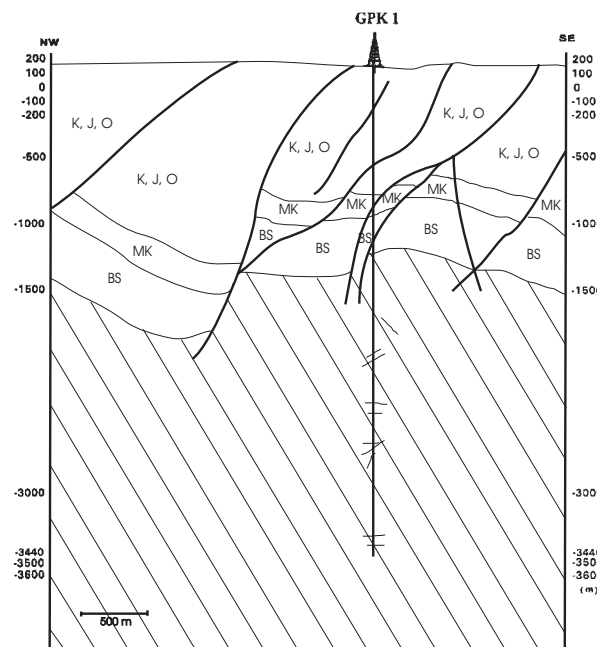


Figure 2-4: Geological cross section of the Soutz site (modified after Menjor et al., 1988). The crosshatched area is the granitic basement, BS Buntsandstein, MK Muschelkalk and K, J, O Keuper, Jurassic and Oligocene sediments.

2.3 TEMPERATURE DATA, FLOW FIELD AND HEAT FLOW

2.3.1 Regional temperature- and flow field

The Rhine Graben is one of the largest anomalies of surface heat flow in central Europe yielding an average value of 80 mW/m^2 . Due to former oil exploration, a large quantity of temperature data is available on the sedimentary cover of the Rhine Graben. The Institute for Joint Geoscientific Research (GGA) in Hannover maintains a temperature database for Germany. It comprises 52'000 temperature data points from almost 10'000 boreholes (for detailed information see Schulz & Schellschmidt, 1991 and Pribnow & Schellschmidt, 2000). The data used in Figure 2-5 and chapter 3 originate from an irregular 3D set of data points consisting of Bottom-Hole-Temperature (BHT) measurements and continuous logs. BHT were recorded just after drilling and temperature values are therefore corrected through methods after Leblanc et al. (1982), Fertl & Wichmann (1977) and Lachenbruch & Brewer (1959). Continuous temperature logs were measured when boreholes were in temperature equilibrium. The accuracy is estimated to be $\pm 3^\circ\text{C}$ for BHT values and $\pm 0.01^\circ\text{C}$ for continuous logs. The temperatures were then interpolated using the Kriging method of Davis (1986). We estimate a maximum error of $\pm 5^\circ\text{C}$ in the temperature data, assuming $\pm 2^\circ\text{C}$ inaccuracy introduced by the applied Kriging method and $\pm 3^\circ\text{C}$ associated with the BHT measurements. In chapter 3, the data will be referred to as 'interpolated temperature values'.

Figure 2-5 shows temperature isotherms at 500 m depth in the central part of the Rhine Graben. There are three major thermal anomalies in this part of the Graben: at Soultz, Landau and near Speyer. All anomalies are confined to the border of the Graben, a typical location where thermal anomalies accompany major Graben faults (Meier et al., 1979, Illies, 1965, Parini, 1981). It is evident that all anomalies lie near the western border of the Graben. Two different processes have been identified to explain this asymmetry: firstly, due to the different elevation of the Graben shoulders (the Black Forest is $\sim 200 \text{ m}$ higher than the Vosges) and a high permeability contrast, a general east-west regional groundwater flow with internal convection is postulated by Gérard et al. (1984), Clauser & Villinger (1990) and Flores-Marquez & Royer (1993). Such flow system could build up more pronounced thermal anomalies on the west. And secondly, since the depth to the crystalline basement increases from west to east, the western heat flow is enhanced by radiogenic heat production. Therefore, the

surface heat flow decreases across the Graben from 150 mW/m^2 in the west (Soultz, Landau) to 70 mW/m^2 in the east, north of Strasbourg.

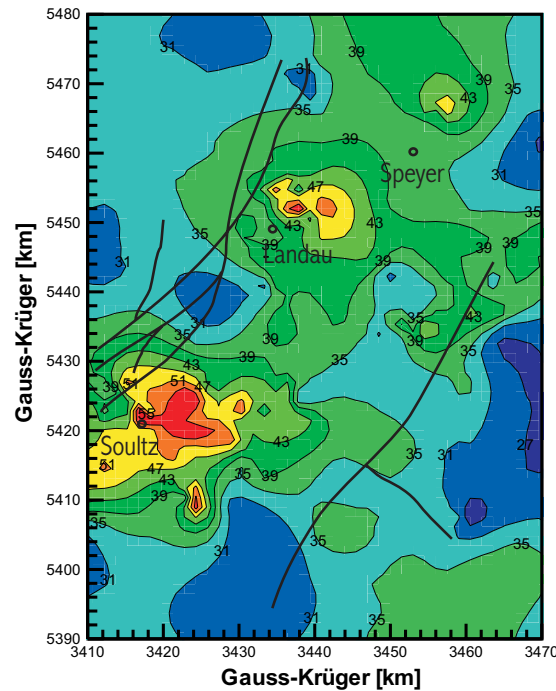


Figure 2-5: Temperatures [$^{\circ}\text{C}$] at 500m depth in the central part of the Rhine Graben. The black lines mark the major faults. The equidistance of the isotherms is 5°C . The temperature data before contouring are from a large database (Pribnow and Schellschmidt, 2000); the locations of the faults are extracted from Illies (1965)).

Several authors have tried to explain the origin of such thermal anomalies. Werner (1975), Parini (1981), Elsass (1995), Pribnow & Schellschmidt (2000) concluded that the heat is redistributed by convection in the upper crust, since observed lateral temperature variations can be explained neither by non-homogeneous distribution of heat production and thermal conductivity, nor by thermal effects such as erosion, uplift or paleo-climate. They also pointed out that the temperature anomalies are not correlated to crustal thickness, which agrees with the deep seismic profile of the ECORS program (Rousset et al., 1992). Detailed studies investigated the convective system at Soultz (Clauser, 1988, Clauser & Villinger, 1990, Flores-Marquez, 1992, Le Carlier et al., 1994, Benderitter & Elsass, 1995, Kohl et al., 2000, Pribnow & Schellschmidt, 2000) through numerical models of coupled fluid flow and heat transport equations. A study by Werner & Parini (1980) explained the thermal anomaly at Landau by advective heating of an aquifer. All authors assumed 2D flow along east-west cross-sections of the Rhine Graben, perpendicular to the Graben

shoulders. However, these conventional models ignore the north-south striking major Graben faults, which might imply north-south convection pattern due to the fault's higher permeability. Chapter 3 addressed a typical local thermal anomaly, focusing especially on these north-south permeability structures to investigate the impact of graben-parallel faults on hydrothermal convection.

2.3.2 Temperature- and flow field at Soultz

As stated before, the Soultz area is in a zone of particularly high temperatures within the general anomaly of the Upper Rhine Graben (Figure 2-5). Geothermal gradients reach 100 K/km down to 1000 m depth but decrease in the basement. In GPK1 and GPK2 a strong variation of vertical heat flow was measured. It drops from 150 mW/m² at the surface to <25 mW/m² at 2000-3000 m depth and recovers at greater depth ($z > 4000$ m) to ~70 mW/m² (Pribnow et al., 1999).

Figure 2-6 shows the temperature increase with depth at GPK2 after deepening the well. At 5000 m depth, formation temperatures of 200°C were reached. The drilling was finished by the end of May 1999. At the beginning of July the borehole was not yet in thermal equilibrium again. Therefore, the temperature log from the 14th of September 1999 yields higher temperatures. Kohl et al., 2000 showed that the local temperature field could be explained by a convective flow pattern, which develops in the domain with the highest degree of fracturation. The convection cell can be localised between the top of the Buntsandstein at ~1000 m and a depth of ~3700 m in the granitic basement. This is also seen in the figure: the temperature gradient in the sediments is high, between 1000 m and 3700 m depth it is lower due to the convection and with greater depth it increases again. The temperature decrease between 1800 m to 2200 m and between 3200 m to 3800 m is due to the stimulation activities and intensive re-injection of cold fluid (~65°C) during the circulation test.

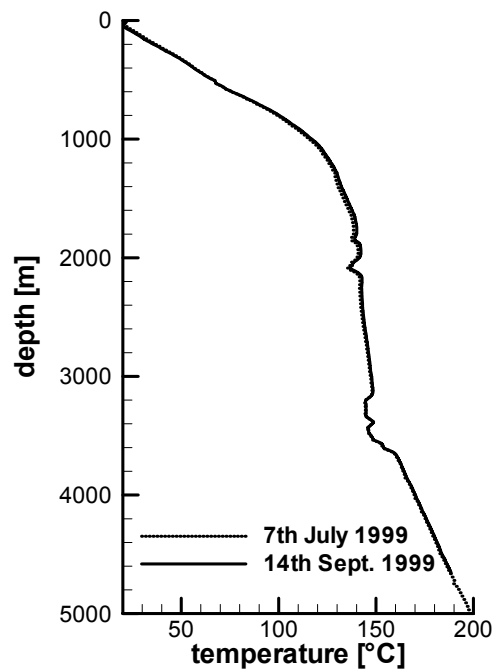


Figure 2-6: Temperature log of GPK2 after drilling (Schellschmidt & Pribnow, 2000).

2.4 GEOCHEMICAL CONDITIONS

2.4.1 Granitic host rock

The granitic host rock at Soultz has been intensively investigated since the drilling of GPK2 (Genter, 1990; Traineau et al., 1991; Azaroual, 1992; Jacquot, 1998). The granite underwent an early pervasive alteration stage, which is widespread in the massif. Transformation of primary minerals (biotite, hornblende, plagioclase) has given way to the secondary assemblages, where chlorite is the most common phase. Later vein alteration related to fluid-rock interactions developed in the fracture system. Three different granitic host rock facies were distinguished via synthetic calculations by Jacquot (1998): unaltered granite, hydrothermalized granite and vein alteration. Table 2-1 lists the mineral assemblage of the different granitic facies and the mineral percentage of the different minerals within the facies. The term ‘hydrothermalized’ refers to hydrothermal alteration in general (result of several phases).

The unaltered granite has a fracture density close to zero and therefore plays a minor role in the fluid rock interaction processes. The hydrothermalized granite consists of blocks partly cemented by alteration products, which mainly consist of clay minerals

and carbonates. This facies is the most porous (Genter et al., 1997) and plays a major role in the fluid rock interaction processes. The fracture density in the vein alteration facies is the highest. The granite is highly altered. The only remaining minerals are those that best resist alteration, which is mainly quartz. Clay minerals, carbonates and secondary quartz veins cement these minerals. The reservoir fluid is not in contact with fresh granite, because of its low fracture density, but with the hydrothermalized granite and the vein alteration Jacquot (1998).

2.4.2 Composition of reservoir fluid

The reservoir fluids originate from brines within Triassic sediments on the border of the Rhine Graben. They became diluted by meteoric water, which dissolved micas and sulphates in the Triassic Buntsandstein and in the granitic basement (Pauwels, 1993; Aquilina et al., 2000). Due to percolation of the fluid into the fractured granitic basement, plagioclases were dissolved and secondary minerals such as quartz, illite, montmorillonite, calcite, dolomite and pyrite were precipitated in fractures.

During past circulation and production tests several fluid samples were taken. In this study we use the data from analyses of fluid samples from GPK2 collected throughout the 1997 production test and assume that the production fluid samples represent the 3500 m deep reservoir fluids. The total amount of dissolved solids (TDS) is greater than 100g/l. This means that the reservoir fluids are brines with a ionic force of 1.6. The fluid sample we are referring to is KP3-97-600 and was collected at the surface of the production site on 16th November 1997. Table 2-2 lists the fluid parameters of this sample. The chemical analyses were done by the Centre de Géochimie de la Surface CGS in Strasbourg. For detailed information on the sampling procedure as well as on the methods of the chemical analyses see Jacquot (2000).

Table 2-1: Synthetic and qualitative mineral assemblage from different granitic facies (after Jacquot, 1998). Percentages are given in volume percentages.

unaltered granite	mineral percentage
quartz	24.2
k-feldspar	23.6
plagioclase	42.5
biotite	4.2
hornblende	3.1
chlorite	2.0
calcite	0.3
hydrothermalized granite	mineral percentage
quartz	24.8
k-feldspar	12.6
chlorite	0.4
illite	27.7
montmorillonite	10.0
calcite	1.6
dolomite	0.3
pyrite	1.4
galena	0.8
vein alteration	mineral percentage
quartz	43.9
illite	40.2
montmorillonite	9.6
calcite	4.3
dolomite	0.7
pyrite	1.0
galena	0.3

Table 2-2: Fluid parameters of sample KP3-97-600 collected at the wellhead of GPK2. The pH value is the one at 33°C. The electric charge of the species is left out. Alk. refers to the Alkalinity of the fluid (chapter 4.1.3) and is given in méq/kg.

species	concentration [mol/kg]	species	concentration [mol/kg]
Na	1.10	As	$1.49 \cdot 10^{-4}$
K	$8.67 \cdot 10^{-2}$	Rb	$2.65 \cdot 10^{-4}$
Ca	$1.67 \cdot 10^{-1}$	Cs	$1.13 \cdot 10^{-4}$
Mg	$4.96 \cdot 10^{-3}$	Al	$1.11 \cdot 10^{-6}$
Cl	1.61	Fe	$4.14 \cdot 10^{-3}$
SO ₄	$2.30 \cdot 10^{-3}$	Ni	$2.98 \cdot 10^{-6}$
Alk.	3.60	Cu	$2.83 \cdot 10^{-7}$
SiO ₂	$2.36 \cdot 10^{-3}$	Co	$6.10 \cdot 10^{-7}$
Br	$2.89 \cdot 10^{-3}$	Cr	$2.88 \cdot 10^{-7}$
B	$3.06 \cdot 10^{-3}$	Cd	$7.77 \cdot 10^{-8}$
F	$2.05 \cdot 10^{-4}$	Zn	$4.89 \cdot 10^{-5}$
Sr	$4.39 \cdot 10^{-3}$	Ag	$4.63 \cdot 10^{-9}$
Li	$1.81 \cdot 10^{-2}$	Ti	$2.67 \cdot 10^{-6}$
Mn	$2.69 \cdot 10^{-4}$	Pb	$1.40 \cdot 10^{-6}$
Ba	$2.12 \cdot 10^{-5}$		
temperature	165°C	pH	5

3 IMPACT OF GRABEN-PARALLEL FAULTS ON HYDROTHERMAL CONVECTION – RHINE GRABEN CASE STUDY

This study addressed a typical local thermal anomaly, focusing especially on the typical north-south permeability structures in the Rhine Graben (chapter 2.3.1) to investigate their impact on hydrothermal convection. First, fault properties and extensions were determined by analytical solutions for convective flow in vertical faults. The solutions were then compared to 3D numerical model results. Finally, the convective fluid flow pattern was investigated in detail using a representative 3D model of such an anomaly (Bächler et al., 2003).

3.1 THE LANDAU GEOTHERMAL ANOMALY

The regional temperature field in the Rhine Graben and its anomalies were discussed in chapter 2.3.1. In the following the focus is on one geothermal anomaly and its local faults. The Landau anomaly was chosen for its high horizontal and vertical density of temperature data. Figure 3-1 shows the detailed temperature distribution at Landau at 500 m and 1000 m depth, respectively. The anomaly mainly consists of two north-south regions of alternatively higher and lower temperatures. These anomalies follow the two prominent faults, Ω and Γ , in the Landau geothermal field: those in the west follow the Ω -fault and those in the east follow the Γ -fault. This pattern suggests north-south convection systems and high permeability values within the Ω - and Γ -faults. The anomalies along the Γ -fault are more concise, perhaps from a different temperature data density or the more complex fault geometry of the Ω -fault. For simplicity, the eastern anomaly series following the Γ -fault is focused. There, the average distance between the temperature maxima is 1800 m. Below, the model is

discussed, which was set up to explain the anomaly pattern along the Γ -fault through a north-south striking convection system.

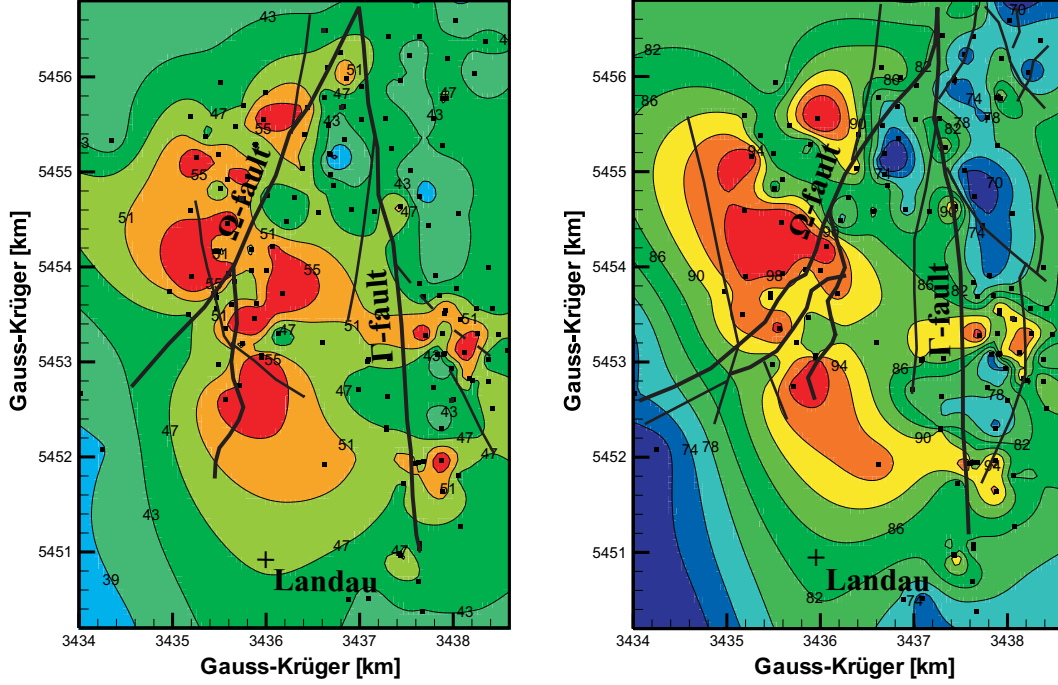


Figure 3-1: Isotherms [$^{\circ}\text{C}$] at 500 m (left) and 1000 m depth (right) for the Landau region. The equidistance of the isotherms is 4°C . The black lines mark the major faults in the region. The squares represent the locations of the data points. The temperature data before contouring are from a large database (Pribnow & Schellschmidt, 2000) and the locations of the faults are taken from Parini (1981).

3.2 ANALYTICAL DESCRIPTIONS OF CONVECTION IN VERTICAL FAULTS

Convection in homogeneous porous media heated from below has been intensively investigated. Horton & Rogers (1945), Lapwood (1948) and Katto & Matsuoka (1967) treated horizontally layered systems with impervious upper and lower boundaries and fixed temperatures. The critical Rayleigh number R_c describing the onset of convection is $4\pi^2$. However, fluid convection in a vertical fault is influenced not only by heat transport processes within the fault but also by lateral heat transfer to and from the surrounding rock mass. Murphy (1979) developed analytical solutions for convection in vertical faults having specific initial and boundary conditions. He assumed a porous fault of given vertical height H , length L , and width W embedded in infinitely extending impermeable rock. Initially, the fluid and rock are in equilibrium and temperature and pressure gradients in the fault are constant. At time

$t = 0^+$, small temperature perturbations ΔT are introduced. If the fault permeability is high enough for convection to set in, the cells take the form of rolls about axes perpendicular to the fault. Darcy's law, Boussinesq approximation, mass conservation and thermal energy equations are used to describe this convection. For a single convection cell, the temperature anomaly ΔT can be described by

$$\Delta T = T_0 \exp(\omega t) \sin\left(\frac{m\pi z}{H}\right) \cos\left(\frac{n\pi x}{H}\right)$$

Equation 3-1

and the in situ Rayleigh number R by

$$R = \frac{\rho g \alpha k W^2 G}{\mu \kappa_m} = \frac{m^2 + n^2}{n^2} \left[\frac{\omega H^2}{\kappa_m} + \left\{ 2 \frac{\lambda_r}{\lambda_m} \left(\frac{H}{W} \right)^2 \Phi \right\} + \pi^2 (m^2 + n^2) \right].$$

Equation 3-2

In the above equations T_0 is the amplitude, ω the convection growth rate, n and m the number of convection cells in x and z directions, respectively (i.e. along L and H of the fault), ρ the fluid density, g the gravitational constant, α the thermal expansion coefficient, k the permeability, G the geothermal gradient, μ the viscosity, κ_m the porous medium thermal diffusivity, λ_r the rock thermal conductivity, λ_m the porous medium thermal conductivity and Φ the heat transfer function. The expression in the curly brackets is also called the *heat transfer grouping*.

The stability of the convection is characterised by ω : $\omega = 0$ describes *neutral stability* (steady-state) with $R = R_c$ and $\omega > 0$ describes *unstable growth* with $R > R_c$. Throughout this study neutral stability ($\omega = 0$) was assumed (see discussion below). R_c depends on the time of the convective onset: if convection sets in immediately at $t = 0^+$ *spontaneous stability* happens. But an initially subcritical convective motion that may become critical with time, if fostered by other forces like fault shifting or displacement, is called *delayed stability*. For faults under spontaneous stability $R_c = 12$ (Murphy, 1979). Under delayed stability R_c is given by

$$R_c(t > 0) = 2 \frac{\lambda_r}{\lambda_m} \frac{W}{(\pi \kappa_r)^{0.5}}$$

Equation 3-3

where κ_r is the rock thermal diffusivity.

Murphy (1979) stated that under neutral stability, the minimal Rayleigh number R_c^* (the star indicates the minimum) occurs when $m = 1$, that is when the convection cell

is of maximum height H . The value of n at which R_c is minimal depends upon Φ . To determine Φ , the rock and the water energy equations must be solved simultaneously. Under neutral stability Φ is given by

$$\Phi = \frac{\beta \lambda_m \left[\exp\left(\frac{\beta^2 \lambda_m^2 \kappa_r t}{(W \lambda_r)^2}\right) \operatorname{erfc} \sqrt{\left(\frac{\beta^2 \lambda_m^2 \kappa_r t}{(W \lambda_r)^2}\right)} \right]}{\lambda_r}$$

Equation 3-4

where β is a constant between 5 and 6.

n can now be interpreted as the height-to-length ratio and the value of n at R_c^* is n^* .

$$n^* = \left[1 + \frac{2 \lambda_r}{\pi^2 \lambda_m} \left(\frac{H}{W} \right)^2 \Phi \right]^{0.25}$$

Equation 3-5

3.2.1 Application to Γ -fault in the Landau region

The analytical solutions discussed above were applied to realistic conditions in graben faults. With a model based on the parameters of the Γ -fault, the goal was to identify the fault's permeability, state of stability and fault geometry that would lead to the observed temperature pattern (Figure 3-1).

Only wide, very permeable faults could be spontaneously unstable. With $R_c = 12$ (see Equation 3-2) and the parameter values from Table 3-1, a minimum fault permeability of $k = 4.8 \cdot 10^{-14} \text{ m}^2$ results in spontaneous convection within the Γ -fault. According to studies by Clauser & Villinger (1990), Flores-Marquez (1992) and Kohl et al. (2000), this value seems characteristic for the Rhine Graben. Thus, the physical situation of the Γ -fault favours spontaneous convection. Otherwise, Equation 3-2 and Equation 3-3 can be used to calculate the time after which delayed convection would set in. Taking the parameter values of Table 3-1 and $k = 4.8 \cdot 10^{-14} \text{ m}^2$ and assume that $\kappa_m = \kappa_r$ and $\lambda_m = \lambda_r$, the delay time $t_D = 7 \cdot 10^8 \text{ sec} = 22 \text{ y}$. Compared to geological time scales, such considerations are negligible.

Table 3-1: Parameter values for the Γ -fault.

W	H	ρ	α	μ	κ_m	g	G	T_0
[m]	[m]	[kg/m ³]	[1/°C]	[Pas]	[m ² /s]	[m/s ²]	[K/m]	[°C]
200	3500	1000	10^{-3}	10^{-4}	$4.7 \cdot 10^{-7}$	9.81	0.03	30

To identify the convection cell geometry, different R_c were evaluated from Equation 3-2 and shown in Figure 3-2 as a function of n , t and the heat transfer grouping. Also shown is the locus of the R_c^* . Low values of R_c (at low heat transfer grouping values) have distinct minima in the curves leading to strongly preferred values of n . Figure 3-2 shows that the longer t_D , the smaller the preferred height-to-length ratio. With given W and H preferred height-to-length ratios of convection cells in faults can be determined. W was chosen based on a study by Werner & Parini (1980). H was estimated from the temperature data in Figure 3-1: assuming a surface temperature of 10°C and a temperature gradient of 30 K/km in pure conductive regimes, the temperatures at 500 m and 1000 m would be 25°C and 40°C , respectively. The temperatures in the Landau region are $20\text{-}40^\circ\text{C}$ higher. Taking the highest measured temperature value along Γ , which is 98°C at 1000 m depth, it was concluded that the minimum source depth of the fluid must be 3000 m (basement, compare Table 3-3). Therefore, the fault must reach at least to that depth. Assuming that the fluid cools on its way to the surface, the source depth must lie even deeper. Therefore, H was estimated to be 3500 m . Unfortunately, due to the depth-limited database, it was not possible to fix the depth of the anomalies. Figure 3-2 shows for the Γ -fault at $t = 7 \cdot 10^8\text{ sec} = 22\text{ y}$, $H = 3500\text{ m}$, $W = 200\text{ m}$, the locus of $R_c^* = 2900$ and $n^* = 4$. At large $(H/W)^2$ ratios (Equation 3-5) the curve becomes flat so that small parameter value changes result in appreciable changes to n^* . The n developed in the fault will be affected by nonideal conditions like local width and lithological variations. This interaction may lead to local changes in convection pattern geometry and thus variable wavelength of the anomaly series.

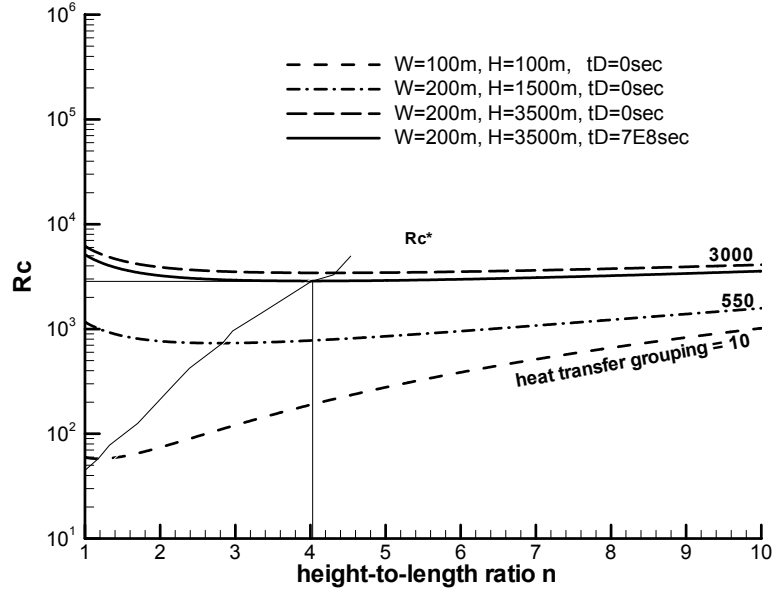


Figure 3-2: Critical Rayleigh numbers as a function of the cell height-to-length ratio, the heat transfer function and the time at neutral stability (modified after Murphy, 1979).

For the calculated n^* , ΔT was then calculated (Equation 3-1) using an initial temperature disturbance of 30°C . Under the given conditions, two cells separate at distances of 1800 m (Figure 3-3). This distance is the average wavelength of the temperature anomaly series found in the Landau region. Therefore, the total fault length L was estimated by

$$L = i * 1800m$$

Equation 3-6

where i is an integer.

With the chosen parameter values the geometry of the Landau temperature anomalies can be reproduced through analytical calculations. However, such solutions are strongly restricted by assumed boundary conditions. The real geology cannot be so simplified. In addition temperature disturbance is forced through fluids heated from a basal heat flow rather than through local temperature disturbances. It needs to be noted that the analytical solutions are aimed at small fault widths with important contributions of lateral heat conduction from or to nearby rock walls. In the porous fault considered here, the time required for the influence of the rock to be felt can be estimated by the thermal length as $t = (0.5 * W)^2 / \kappa_m \sim 700$ years (Carslaw & Jaeger, 1959). Compared to the parameters of the system and time required to reach steady-

state (which will be shown below), the needed time for a diffusive front to penetrate the fault's centre is therefore important. These considerations show that analytical solutions only roughly approximate real conditions. To overcome these limitations, numerical solutions were used below.

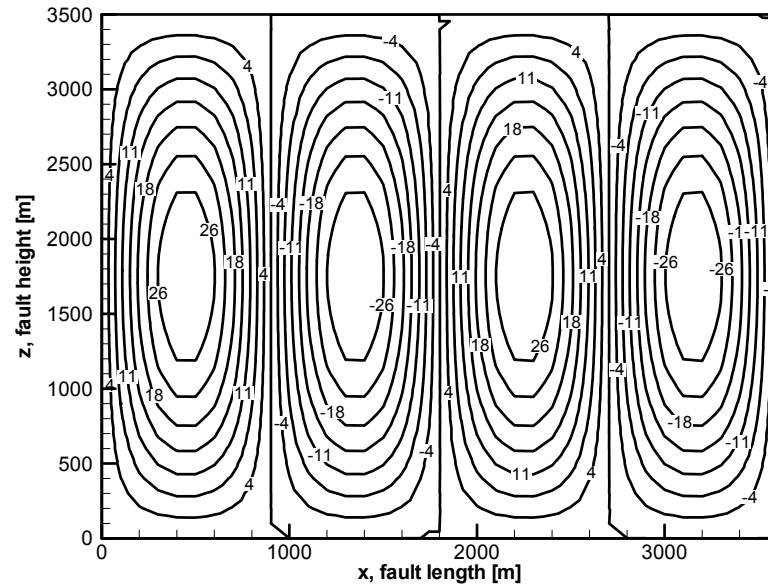


Figure 3-3: Analytically calculated temperature disturbance [°C] in the fault.

3.3 COMPARISON OF ANALYTICAL SOLUTIONS AND NUMERICAL RESULTS

3.3.1 General considerations

Numerical simulations of convective systems are delicate because they tend to numerical oscillations (i.e. Brooks & Hughes, 1982). Coupled calculations require careful treatment, since numerical oscillations in one physical process can be interpreted as perturbation in the other. The numerical result is especially sensitive to the effect of large time steps. Sensitivity analyses have demonstrated that time steps up to $t = 10^6$ seconds can be used. Further analyses showed that the investigated fault system could be regarded as stationary if there has been no change for 10'000 years.

Usually transmissivity T_r ($T_r = k \cdot W / \mu$) is used to describe hydraulic processes in physical systems. Given the variable lateral influence of the matrix on temperature evolution in the fault and in agreement with Murphy's (1979) analytical solutions, permeability, rather than transmissivity, was used in the following.

3.3.2 Numerical models

The *TOUGH2* code (Pruess, 1991) is used for numerical modelling. A detailed description of *TOUGH2* is given in chapter 5.3.1. Two different numerical models were treated and the results were compared to the analytical results. Model 1 compared analytical solutions with the numerical model using identical geometry, boundary conditions and an initial temperature perturbation of 30°C. More realistic conditions were investigated in model 2, applying a basal heat flow of 0.1 W/m² at the lower model boundary.

Both models used the same model geometry, consisting of a fault ($H = 3500$ m, $W = 200$ m) and surrounding matrix. The fault length is 3600 m (i.e. $2 \cdot 1800$ m) extending along the x-axis. Subject to sensitivity analyses (see below), the surrounding matrix thickness is 600 m and extends along the y-axis. Identical parameter values were used in comparing the numerically simulated results with analytical calculations. The boundary was assumed to be impermeable and its temperature constant. Convection in the matrix was ignored. The top boundary was fixed at a constant temperature of 10°C and a pressure of 10^5 Pa. Preliminary tests showed that the permeability has to be $k \geq 5 \cdot 10^{-13}$ m² for the onset of convection. At the beginning of the simulation, constant temperature (30 K/km) and pressure gradients (10^4 Pa/m) were assumed. The parameter values of the model are listed in Table 3-2.

Table 3-2: Parameter values for the numerical model 1 and 2.

unit	density	porosity	permeability	heat	heat capacity
	ρ	Φ	k	conductivity λ	c_p
	[kg/m ³]	[%]	[m ²]	[W/mK]	[J/kgK]
matrix	2650	1	10^{-18}	3	1000
fault	2000	10	$5 \cdot 10^{-13}$	2	1000

3.3.3 Results

In model 1 four convection cells develop in the 3600 m fault zone agreeing with analytical calculations. Figure 3-4 shows the temperature distribution and the convection cells at steady-state. Figure 3-5a illustrates the temperature distribution at 1000 m depth at four different time steps. Initially only two convection cells develop in the fault; then two other cells develop and grow until they extend over the whole fault height at steady-state. Note that one temperature peak equals two convection cells (see Figure 3-4). As soon as all convection cells are built, the number of the cells remains constant. Fluid velocity within the fault is between 10^{-10} m/s and 10^{-9} m/s. Convective onset is 100 years later than in the analytical study, perhaps due to the inertness of the numerical model's slowness in reacting to temperature disturbance. The geometry of the convection cells could be reproduced with this numerical model, which means that for this specific case the numerical methods and analytical solutions lead to identical results. Thus, the numerical procedure was verified, which will be extended below to more complex cases.

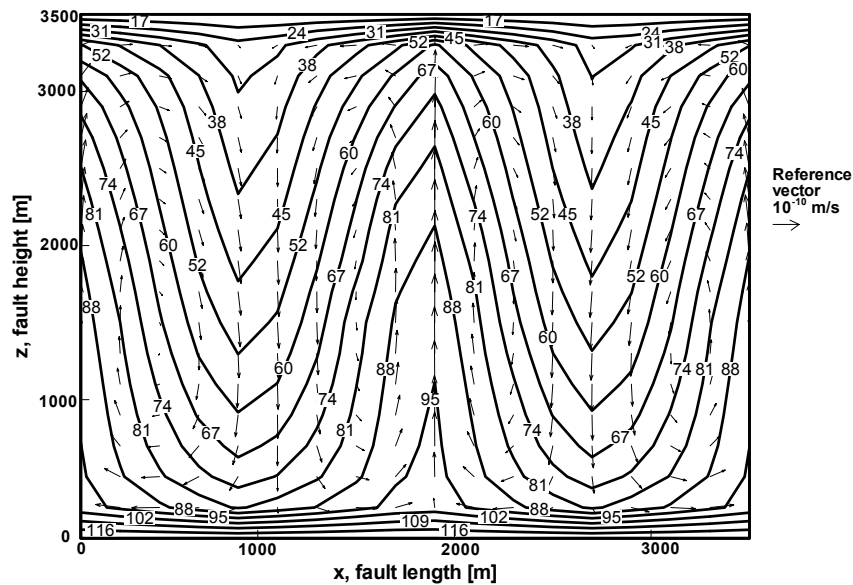


Figure 3-4: Temperature distribution [$^{\circ}$ C] and convection cells in the fault for model 1 at steady-state (17'440 years).

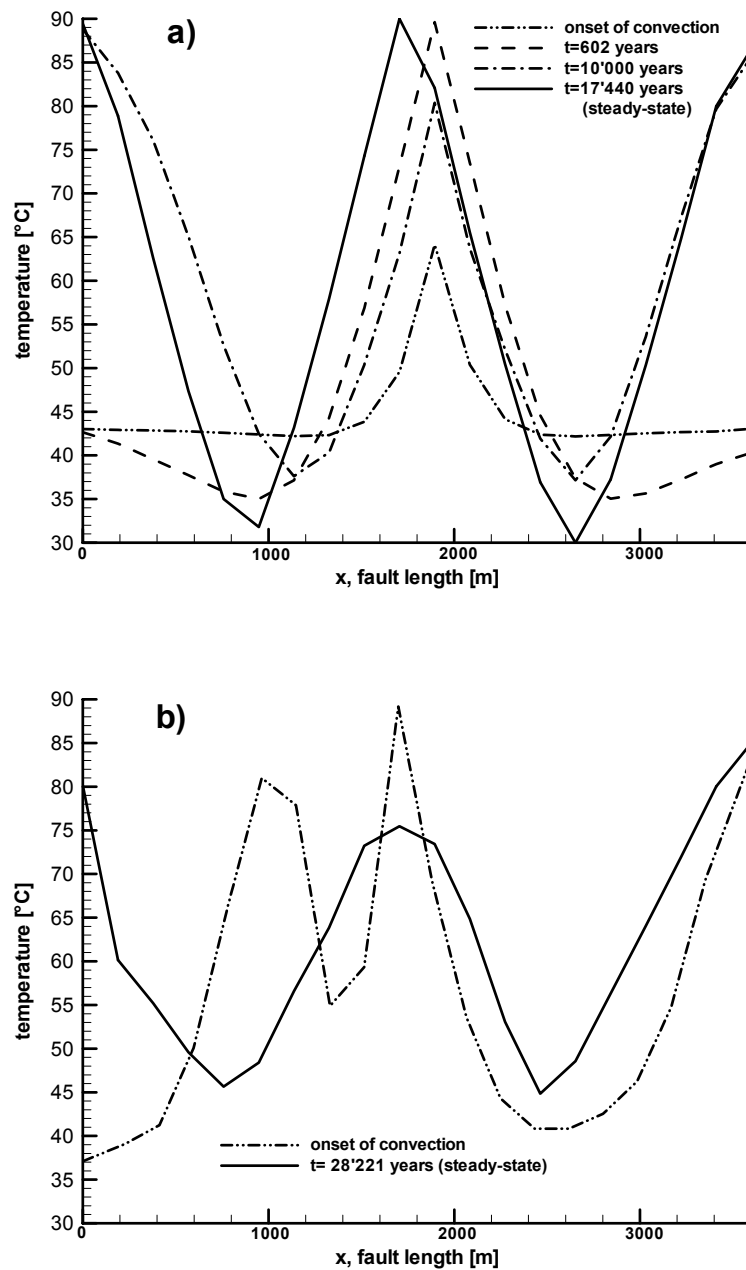


Figure 3-5: a) Temperature distribution at 1000 m depth for model 1 at four different time steps. b) Temperature at 1000 m depth for model 2 at the beginning of the convection and at steady-state.

To verify the results, sensitivity analyses for model 1 were performed:

- Refining the model did not change the result.
- Models of 1800 m and 5400 m fault length were tested to see if boundary effects influence the resulting number of convection cells. As expected from Equation 3-6, the resulting number of convection cells was two and six, respectively.

- Changing the fault permeability did not influence the number as long as permeability was high enough to stimulate convection: increased fault permeability decreased the time steps taken by *TOUGH2* and decreased permeability ($<5 \cdot 10^{-13} \text{ m}^2$) hindered convection.
- Matrix thickness adjacent to the fault had no impact on the number of convection cells.

Figure 3-5b shows the simulation results for model 2 at the beginning of convection and at steady-state. In contrast to model 1, many irregular convection cells develop at the beginning of the simulation. With increased simulation time, the number of cells gradually decreases and eventually four cells result as in model 1. This time dependency already appeared in the analytical solutions (Figure 3-2). The fluid velocity in the fault is the same as in model 1. Due to the continuous basal heat flow, a larger amount of heat is introduced, making the time needed to reach steady-state longer than in model 1.

Sensitivity analysis showed, however, that matrix thickness influences the number of convection cells. This is in contrast to models with temperature disturbance stimulation, where matrix thickness did not affect the geometry of convection cells. The same cell geometry as in the analytical calculations was reproduced, assuming matrix thickness of 600 m.

In summary, analytical solutions are useful for simple vertical fault models and when the same initial conditions (i.e. stimulation through temperature disturbance) are assumed, numerical simulation perfectly reproduces these results. Since no analytical solutions exist for models with more realistic geology, numerical simulations can provide necessary information. Due to the large number of parameters that might influence the resulting convection field, no general rules can be given and each site has to be investigated individually.

3.4 NUMERICAL MODEL OF THE LANDAU GEOTHERMAL ANOMALIES ALONG THE Γ -FAULT

So far, only the convective pattern geometry has been investigated and the temperature distribution was ignored. The following presents a more complex numerical model, which also addresses the temperature distribution along the Γ -fault.

3.4.1 Numerical model

This model represents a simplified discretization of the geology along the Γ -fault from 5451.2-5454.8 km (see Figure 3-1) and is based on a cross-section of Doebl (1970). Figure 3-6 shows the model geometry, which extends 3600 m along the Graben (x-axis, i.e. fault length), 7400 m across the Graben (y-axis), and to depth of 5000 m (z-axis). The discretization is 200 m along the Graben, 100 m across the Graben, and 100 m in depth, except in the intervals $z = 500$ to 600 m and $z = 4000$ to 4100 m, where 50 m was used. The model consists of $\sim 70'000$ elements. In this section of the Graben, the Γ -fault has a steep west-east inclination. To the west of the Γ -fault the crystalline basement is at ~ 1400 m depth; to the east it is at ~ 2200 m due to a fault offset. The geometry of this steeply inclined fault was simplified as a vertical structure ($W = 200$ m). In agreement with Doebl (1970) such a 'fault' is considered as a strongly fractured zone rather than a single major fracture. To highlight the impact of the Γ -fault in the selected region, all other faults in the region were neglected. Following the geological description of Illies (1965), Buntsandstein and crystalline basement layers were included at the bottom of the model. Geologic units of similar permeability and heat conduction were merged to a single unit: Quarternary graben fill, Tertiary and Keuper were lumped into one unit and Muschelkalk and Buntsandstein into a second. The granitic basement and the fault zone are separate units. The parameter values for the different units were taken from Parini (1981) and Clauser & Villinger (1990). Table 3-3 lists the assumed parameter values for these different units. Again, constant temperature (30 K/km) and pressure gradients (10^4 Pa/m) are assumed at the beginning of the simulation. The top boundary was fixed at a constant temperature of 10°C and a pressure of 10^5 Pa. The lateral boundaries are no-flow boundaries and at the bottom a constant basal heat flow of 0.1 W/m^2 was assumed. This value accounts for the Landau anomaly, which is 0.02 W/m^2 above the average value in the Rhine Graben. Heat production was ignored and surface elevations were not taken into account.

Table 3-3: Parameter values for the Γ -fault model.

unit	density	porosity	permeability	heat conductivity	heat capacity
	ρ	Φ	k	λ	c_p
	[kg/m ³]	[%]	[m ²]	[W/mK]	[J/kgK]
Graben fill	1800	1	$5 \cdot 10^{-18}$	3	1000
Muschelkalk & Buntsandstein	2400	1	10^{-16}	4	1000
Basement	2650	1	10^{-20}	2	1000
Fault	2000	10	$5 \cdot 10^{-13}$	2	1000

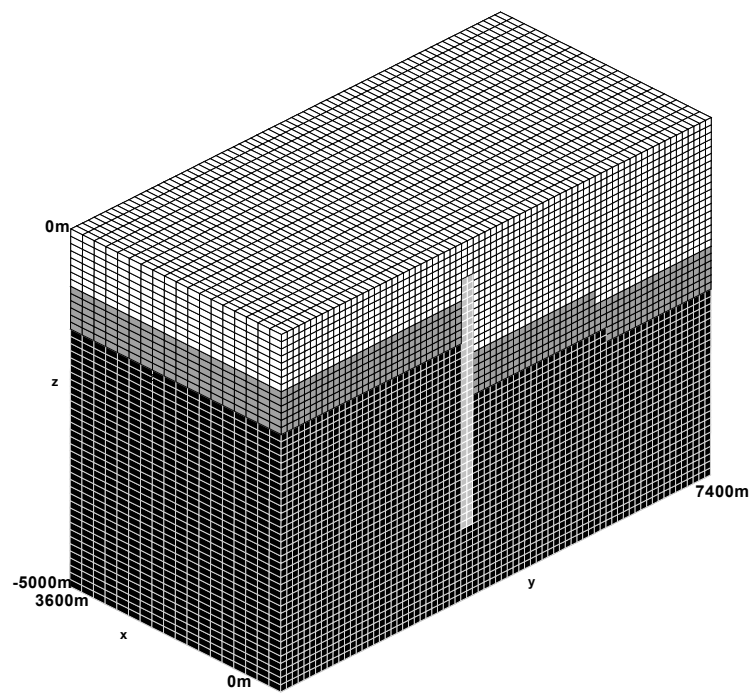


Figure 3-6: Model geometry of the Γ -fault and surroundings. The white area represents the Quarternary graben fill, Tertiary and Keuper, the grey area the Muschelkalk and the Buntsandstein, the black area the granitic basement, and the highlighted white area the fault zone.

There are contradicting statements on the salinity distribution within faults: Schad (1962) claims that there are fresh water zones near the prominent fault and Wyllie (1963) states that high resistivity anomalies occur near the faults indicating fresh water circulation. In contrast, at Soultz highly saline fluids in the fault zones are observed (i.e. Pauwels et al., 1992; Elsass et al., 1995). The present model approach assumes a homogeneous salinity distribution in the fault. Thus, convection occurs due to differences in temperatures and not in salinity, no matter if the fluid is highly saline or fresh water.

3.4.2 Results

To compare the simulation results with the real temperature distribution in the fault, temperature values were extracted from Figure 3-1 along the Γ -fault (Figure 3-7). Several models were tested with different upper and lower fault boundaries. The simulation results show that the model with the permeable zone of the fault between 550 m and 4050 m ($H = 3500$ m) best fits the interpolated temperatures both at 500 m and at 1000 m depth within the $\pm 5^\circ\text{C}$ accuracy (Figure 3-7). Again a time-dependent development in the number of convection cells was found as shown in the analytical calculations and the numerical simulations (model 2): at the beginning of the simulation, many convection cells develop that gradually converge. At steady-state four cells with a distance of 1800 m between their maxima remain, in agreement with analytical results. However, convection sets in at $t_D = 850$ years, which is later than calculated by the analytical solutions. This may be attributed to the inertness of the numerical model to temperature disturbance like in the previous models. Steady-state is reached at $t = 77'000$ years, the minimum age of the anomaly. The fluid velocity in the fault is between 10^{-9} to 10^{-10} m/s. Thus, the presented model allows reproduction of the convection pattern geometry and the temperature distribution.

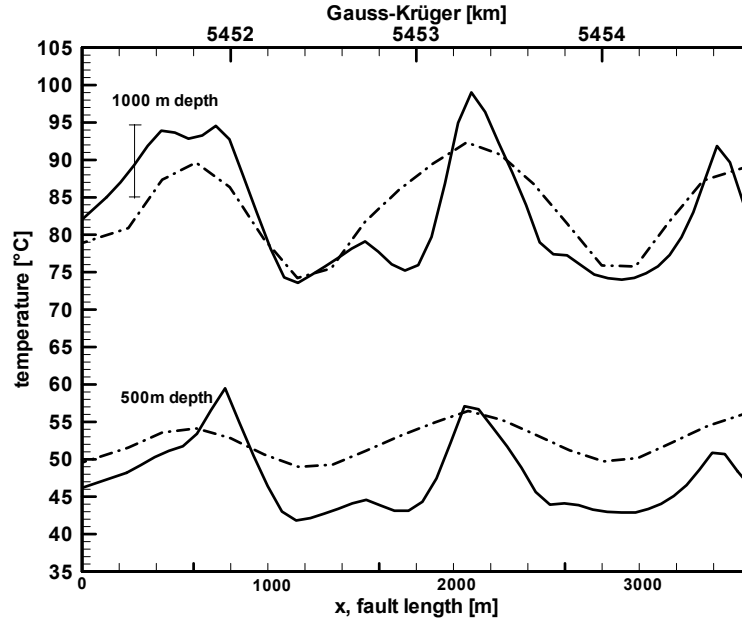


Figure 3-7: Measured temperatures (solid lines) along the Γ -fault at Landau and numerically calculated temperatures (dashed lines) at steady-state in the fault at 500 m and 1000 m depth, respectively. The error bar shows the estimated error of $\pm 5^\circ\text{C}$ in the temperature.

3.4.3 Discussion

The numerical results allow us to verify assumptions made for analytical calculations. Firstly, the numerical simulations also confirmed the 3500 m height of the fault's permeable zone assumed in the analytical calculations. Secondly, since a steady-state is reached, the simulation implies that no supercritical growth sets in and the assumption of neutral stability holds true. Thirdly, the assumption of spontaneous stability is validated because the convective onset is relatively fast regarding the time till steady-state. And finally, the chosen permeability is high enough for spontaneous convection.

The presented results can be extrapolated from the 3600 m model to larger fault systems extending over regional scale for similar geological structures. Such structures can potentially explain the numerous observed sequences of temperature anomalies in the Landau region. However, due to non-ideal conditions such as local width, lithological variations and displacements of faults, the observed wavelength of the anomalies can vary locally. Analytical considerations have shown that such variations occur easily because the curve for the preferred height-to-length ratio value flattens at large $(H/W)^2$ ratios (Figure 3-2).

Sensitivity studies were performed to test the influence of fault width on convection pattern and temperature distribution in the fault. Two additional models with different fault widths (100 m and 400 m) were investigated. To compare their results with the previous model, the transmissivity value was kept identical and therefore, the permeability values were adapted to $k = 10^{-12} \text{ m}^2$ (100 m model) and to $k = 2.5 \cdot 10^{-13} \text{ m}^2$ (400 m model). Figure 3-8 shows the temperature distribution at steady-state in the fault at 500 m and 1000 m depth, respectively, for the two models compared to the original. The model results indicate that the lower the permeability (the wider the fault), the longer it takes to reach steady-state. The 100 m model reaches steady-state at $t = 50'000$ years and the 400 m model at $t = 200'000$ years (as compared to the original model at $t = 77'000$ years). Analytical considerations showed that the wavelength is very sensitive to the fault width (Figure 3-2): the larger W , the smaller n and the longer the wavelength. The numerical results however, do not reveal such dependency. At 500 m depth, the convection pattern is identical for all models and the temperature distribution diverges only slightly. Since the upper fault boundary is at 550 m, the temperature distribution is dominated by diffusive heat transport. Variation in the fault width has therefore no major effect at this depth. At 1000 m depth, the temperature distribution and convection pattern of the 100 m model fits the original model and in the 400 m model the temperature differs slightly ($\sim 7^\circ\text{C}$) and the wavelength is only a little longer. This finding indicates that permeability has a bigger influence on convection pattern and temperature distribution in the fault than fault width. The lower permeability in the 400 m model results in a more diffusive dominated system leading to lower temperature values. In the 100 m model the lateral influence of the matrix dampens the temperature variation in the fault resulting in a smaller difference between the maximal and minimal temperatures.

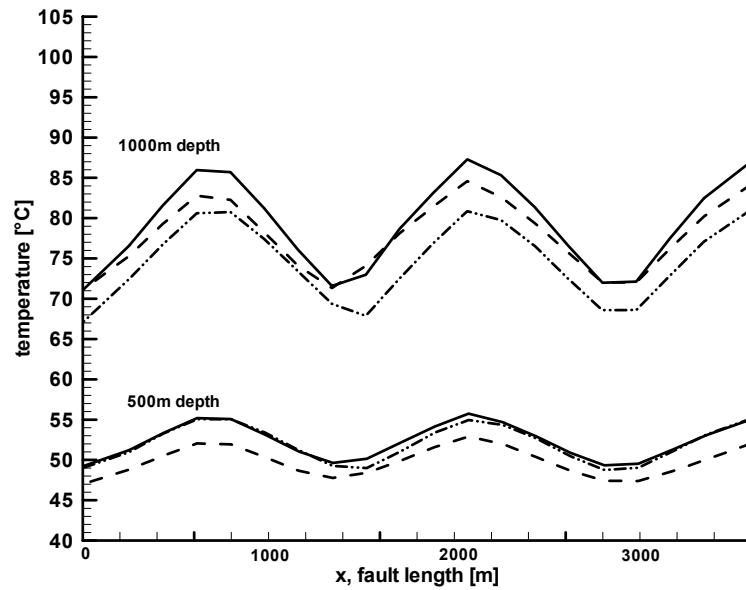


Figure 3-8: Comparison of calculated temperatures at steady-state in the fault at 500 m and 1000 m depth, respectively, for models with different fault widths: 100 m= dashed lines, 200 m= solid lines, 400 m= dashed-dotted lines.

3.5 CONCLUSIONS AND OUTLOOK

The study highlights a direction dependent large-scale permeability distribution in the Rhine Graben. This anisotropy results from the typical stress regime of graben systems with minimum horizontal stress perpendicular to the strike of the Graben. Therefore, fracturing encourages flow in graben-parallel structures. Previous hydrothermal models ignored this important permeability structure. The observed small-scale temperature pattern can be explained only by convection systems within north-south striking fault zones. On the regional scale, major temperature anomalies such as Landau, Speyer and Soultz may be considered as the result of superposition and interaction of several graben-parallel convection systems. The importance of the north-south convection system is also confirmed by comparing graben-parallel with graben-perpendicular fluid flux. The latter can be estimated using calculated velocities from numerical simulations for a vertical cross-section perpendicular to the graben strike (Clauser, 1988). Averaging these velocities and multiplying them with a representative area (the length of a single convection cell multiplied by the height of the sedimentary cover) results in a graben-perpendicular flux of $\sim 10^{-6} \text{ m}^3/\text{s}$. The graben-parallel fluid flux is calculated from the velocity distribution above the centre of a convection cell multiplied by the fault width and half the height of the cell and

results in $\sim 3 \cdot 10^{-4} \text{ m}^3/\text{s}$. Thus, the graben-perpendicular fluid flux is negligible compared to the graben-parallel flux. Future investigations of temperature anomalies in the Rhine Graben must account for the graben-parallel component.

The presented results correlate with findings from other geothermal anomalies in the Rhine Graben such as Soultz. Temperature profiles of the 5000 m deep borehole GPK2 (Figure 2-6) at Soultz indicate convective impacts between 800 m to 4000 m depth (Figure 2-6). Kohl et al. (2000) showed that the local temperature field can be explained by a convective flow pattern which develops between 1000 m and 3700 m with similar fluid velocities like those used in this study. Since the thermal regime at Soultz also seems diffusive below 5000 m depth, it can be speculated that these faults have vertical extensions like those at Landau too. Future geothermal exploration in the Rhine Graben will yield more temperature data and potentially more information on fault geometries there. Clarifying graben-wide thermal features helps to delineate the general framework for HDR geothermal energy use at Soultz.

Generally, structures like the North Sea Central Graben, Vallès-Penedès (E) or the Basin and Range province (USA) are common locations for geothermal anomalies. In most cases such thermal anomalies are associated with the graben master faults. The presented study may provide common clues for investigating other graben-parallel temperature anomalies.

4 CHEMICAL MODELLING

To understand the later description of the coupled code *FRACHEM*, some chemical background is needed. Therefore, an introduction into chemical thermodynamics and kinetics is given. Since there is plenty of literature, only the most important insights are outlined. For further reading please refer to the cited literature.

4.1 CHEMICAL THERMODYNAMICS

Every chemical reaction such as, for example, the dissolution/precipitation equation for calcite



Equation 4-1

can be written in the general form

$$0 \leftrightarrow \sum_{i=1}^N \nu_i A_i .$$

Equation 4-2

The quantities ν_i define the stoichiometric coefficients of the reaction, A_i the species and N the number of species. Note that all parameters and their units are summarized in Table A.

The driving force for chemical reactions is the Gibbs free energy of reaction G (Anderson and Crerar, 1993). The free energy change ΔG comprises an enthalpy and an entropy contribution

$$\Delta G = \Delta H - T * \Delta S_r .$$

Equation 4-3

For standard state conditions

$$\Delta G^{\circ} = \Delta H^{\circ} - T^* \Delta S_r^{\circ} .$$

Equation 4-4

H is the enthalpy of the reaction, T the temperature at which the reaction takes place, S_r the entropy of the reaction, G° the standard Gibbs free energy, H° the standard enthalpy and S_r° the standard entropy. The driving force for a reaction can be the result of a negative H, a positive S_r , or both.

4.1.1 The equilibrium constant K

To describe equilibrium compositions of aqueous systems and to predict the direction of possible changes, the relationship between chemical potentials μ and composition has to be known. μ of any species i is

$$\mu_i = \mu_i^{\circ} + RT^* \ln a_i .$$

Equation 4-5

μ_i° is the standard chemical potential of species i, a_i the activity and R the gas constant (8.134 J/molK).

The relationship between G and the composition of the system is obtained by substituting the expression for μ (Equation 4-5) into the expression for ΔG (Equation 4-3). The result is

$$\Delta G = \Delta G^{\circ} + RT \ln Q$$

Equation 4-6

where Q is the reaction quotient

$$Q = \prod_i a_i^{v_i} .$$

Equation 4-7

At equilibrium, $\Delta G = 0$ and the numerical value of Q becomes K, the equilibrium constant

$$K \equiv Q_{eq} = \prod_i a_i^{v_i}$$

Equation 4-8

and Equation 4-6 is reduced to

$$\Delta G^\circ = -RT \ln K .$$

Equation 4-9

4.1.2 The saturation index SI

The logarithm of the ratio between the reaction quotient Q and the equilibrium constant K is called the saturation index SI

$$SI = \log \frac{Q}{K} .$$

Equation 4-10

The saturation index indicates the saturation state of a mineral in a solution. If $SI > 0$ the solution is oversaturated with respect to a specific mineral, whereas if the $SI < 0$ the solution is undersaturated with respect to a specific mineral and the solution is in equilibrium if $SI = 0$.

4.1.3 pH and alkalinity

The pH value simply is the negative logarithm of the H^+ activity

$$pH = -\log a_{H^+} .$$

Equation 4-11

The alkalinity of a solution corresponds to the quantity of added H^+ ions needed, from which each new acid addition will cause an equivalent diminution of the pH. For example, 1 mole of CO_3^{2-} can absorb 2 moles of H^+ with the reactions $CO_3^{2-} + 2H^+ \leftrightarrow HCO_3^- + H^+ \leftrightarrow H_2CO_3$. In usual aqueous solutions, the alkalinity is close to $Alk(\text{m\acute{e}q/l}) = 2 * CO_3^{2-} (\text{mmol/l}) + HCO_3^-(\text{mmol/l})$. m\acute{e}q stands for 'miliequivalent'.

4.1.4 Activity coefficient

Mostly, non-standard state reactions are considered. The products and reactants are then not in their standard state. Therefore, the difference between ΔG° and ΔG has to be defined as a function of the activity a_i

$$\Delta G - \Delta G^\circ = RT \ln a_i .$$

Equation 4-12

Standard states are chosen such that if the system behaves ideally, the activity takes on very simple forms. If the system is not ideal, an adjustment factor called the

activity coefficient γ has to be introduced to convert the simple activity into the true activity. For aqueous solutions the activity is

$$a_i = m_i * \gamma_i$$

Equation 4-13

where γ_i is the activity coefficient of a species i and m_i is the mole fraction. The activity of aqueous species in solution depends on its molality (mol/kg fluid) and on the interaction forces between ions. There are different methods to quantify these forces: the Debye-Huckel equation, extensions of the Debye-Huckel equation and the Pitzer equations.

Debye-Huckel equation

Activity coefficients for ions can be calculated for relatively low concentrations by the Debye-Huckel equation

$$-\log \gamma_i = A * z_i^2 * I^{0.5}.$$

Equation 4-14

A is a constant depending on the temperature and dielectric constant of the solvent and z_i is the charge of the ionic species i . The interaction forces between ions are described by the ionic strength I

$$I = \frac{1}{2} \sum_i m_i z_i^2.$$

Equation 4-15

In the Debye-Huckel equations, ions are regarded as point centres of charge in a medium with a dielectric constant equal to that of the pure solvent. This idealization results in reasonable agreement with experiments for solutions with ionic strengths up to 0.1. For ionic strengths up to 0.8 an extended version of the Debye-Huckel equation, also called the Davies equations, is more accurate (Davies, 1962; Helgeson, 1969 and Helgeson, 1981).

Pitzer equations

In mixed salt solutions and brines - such as the Soultz fluid - special attention has to be paid to interactions between specific pairs of ions. This is accounted for in the Pitzer equations (Pitzer, 1973 and Pitzer, 1975) to calculate activity coefficients. The Pitzer approach is a semi-empirical model. It combines the Debye-Huckel equation with additional terms describing the concentration dependence of the Gibbs energy

for non-ideal conditions (Kühn, 2003). The difference between the ideal and the real Gibbs energy (G° and G , respectively) is written in the form of a virial equation (a power series expansion):

$$\frac{G - G^\circ}{w_w * R * T} = f(I) + \sum_i m_i \sum_j m_j * B(I) + \sum_i m_i \sum_j m_j \sum_k m_k * \Psi_{ijk} + \dots$$

Equation 4-16

w_w is the water mass and m the molality of species i , j and k . $f(I)$ is the Debye-Huckel equation, the second virial coefficient B represents the interactions between pairs of components i and j in the solution and the third virial coefficient Ψ represents ternary interactions between components i , j and k . The second and higher terms, vanish for dilute solutions and the Debye-Huckel equation results. The series of virial coefficients can be extended to higher orders but the first three virial coefficients are sufficient to describe solutions of high salinity (Pitzer, 1991).

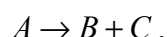
The virial methods differ from other techniques in that they take no explicit account of the distribution of species in solution (Bethke, 1996). In their simplest form, the equations recognize only free ions, as if each salt has fully dissociated in solution. In many chemical systems, however, it is desirable to include some complex species in the virial formulation. Species that protonate and deprotonate with pH, such as those in the series CO_3^{2-} , HCO_3^- and $\text{CO}_{2(\text{aq})}$, typically need to be included. In the virial methods, therefore, the activity coefficients account implicitly for the reduction of the free ion's activity due to the formation of ion pairs, and complex species are not included in the formulation. As such, the Pitzer equations describe not only the factors traditionally accounted for by activity models, such as the effect of electrostatic interaction (Debye-Huckel equations), but also the distribution of species in solution.

4.2 CHEMICAL KINETICS

In geochemical systems chemical components, such as ions, are redistributed among fluid and solid phases. The velocity of this process depends on the rates of chemical reactions. In the preceding section, equilibrium has been considered. A reversible process reaches equilibrium when its forward and reverse reactions proceed at equal rates. By calculating equilibrium concentrations, we determine the state of a system when its free energy has been expended, when nothing more can happen unless a change in composition or of conditions is introduced. Such calculations can predict

possible results of mixing any combination of materials at a given temperature and pressure. Unfortunately, the calculations often do not tell us if these predictions actually take place. This is because long time constants may be needed to attain equilibrium. Equilibrium reasoning is useful in setting limits on possible processes in nature, but reaction rates are often more important in determining what actually happens in a reasonable time (Krauskopf, 1995).

The rate of a reaction depends on the concentrations of the reacting substances. The simplest process to illustrate this is a reaction in which a single substance A breaks into two others, B and C



Equation 4-17

This is a so-called first-order reaction. Its reaction rate is

$$rate = -\frac{d[A]}{dt} = r[A] .$$

Equation 4-18

r is the rate constant and the brackets indicate concentrations. Equation 4-19 is the result after integration. c is the integration constant. If we set $\ln[A^\circ] = c$ at $t = 0$ Equation 4-20 results.

$$\ln[A] = -r * t + c$$

Equation 4-19

$$[A] = [A^\circ] * e^{-rt}$$

Equation 4-20

Reactions of this simple form are not common in nature. Unfortunately, there is no rule for the determination of reaction equations for a specific reaction. The reaction laws have to be identified experimentally. Equation 4-21 illustrates the most general form of a kinetic reaction. s is the mineral surface and m, n are empirical constants.

$$\frac{d[A]}{dt} = r(T) * s * (SI^{m-1})^n$$

Equation 4-21

4.2.1 Effect of temperature on rates

Reaction rates depend in many variables, among which temperature is particularly important. Most reactions go faster at higher temperatures. A brief look at reaction

mechanisms gives a basis for a quantitative treatment. Any reaction can take place only when particles of A and B collide and when the particles are supplied with the necessary energy, which is called the activation energy E_a . At higher temperatures more particles are activated and since particles move faster at higher temperatures, the reaction goes faster.

The activation energy can be related to temperature by an equation suggested by Arrhenius (Krauskopf, 1995):

$$r = A * e^{-\frac{E_a}{RT}}.$$

Equation 4-22

Here A is a constant specific for each equation. In order to receive a relation between the reaction constants r_1 and r_2 at two different temperatures T_1 and T_2 , the above reaction is rewritten:

$$\ln r_1 = \ln A - \frac{E_a}{RT_1} \text{ respectively}$$

Equation 4-23

$$\ln r_2 = \ln A - \frac{E_a}{RT_2}.$$

Equation 4-24

By subtracting equation Equation 4-24 from equation Equation 4-23, equation Equation 4-25 results. If the temperature T_1 and k_1 is known, r_2 at another temperature T_2 can be calculated.

$$\ln \frac{r_1}{r_2} = -\frac{E_a}{R} \left(\frac{1}{T_2} - \frac{1}{T_1} \right).$$

Equation 4-25

4.3 THERMODYNAMIC MODEL OF THE SOULTZ SYSTEM

A detailed description of the thermodynamic modelling of the Soultz HDR reservoir is given in Durst (2002). In the following, the main findings are resumed.

4.3.1 Calculation of the activity coefficients

Pitzer equations were used to determine the activity coefficients, since Soultz fluid has an ionic strength of around 1.6. Unfortunately, the use of these equations is has some inconvenient consequences. The increased complexity of the model decreases the performance. In addition, no reliable theoretical models exist at present to

calculate the aluminium activity in hot brines. For some species, like Mg^{2+} and Fe^{2+} , parameters are not available for higher temperatures (165°C and above). Thus, to simplify the model, special assumptions were made. For the Soultz system it can be assumed:

- modelled fluid is formation fluid
- no boiling or degassing
- no mixing with a different type of fluid
- fluid-rock interactions do not modify the concentration of major species (chlorine and sodium)

With those simplifications, only the temperature significantly influences the Pitzer equations. The activity coefficients could be calculated for H, O, Na, K, Ca, Si, C, Cl, SO_4 , Mg, HS and Fe. Detailed information on the determination of the activity coefficients is given in Durst (2002).

Comparative modelling of the speciation in solution for the Soultz type brine was carried out at different temperatures by comparing results from two different thermodynamic codes (Durst 2001). One code uses the Debye-Huckel approach to calculate the activity coefficients and the other the Pitzer formalism. The results show significant differences between the two model approaches and underline the necessity of using the Pitzer formalism when modelling brines.

4.3.2 Modelling of the Soultz formation fluid

The sample KP3-97-600 collected at the wellhead of GPK2 was the basis for the modelling of the formation fluid (Table 2-2, chapter 2.4.2). The fluid sample withdrawal and analysis were connected with several problems. 1) Sampling of deep fluid is technically difficult. Wellhead sampling results in fluids that underwent transformations such as degassing during upflow, whereas downhole sampling at high pressure and temperature is often unsuccessful. 2) Most of the analyses were performed on cold samples, when some minerals had already precipitated. 3) The high salinity of the fluids ($\text{TDS} > 100 \text{ g/l}$) requires dilution for some analytical methods, which increases the error percentage of the result for minor elements. Thus, to obtain reasonable values, assumptions such as thermodynamic equilibrium of the fluid with the mineral assemblage of the fracture fillings were made (Durst and Vuataz, 2000). Table 4-1 lists the fluid parameters with respect to the reservoir depth and in

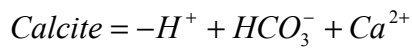
equilibrium with the mineral assemblage. There is no gas content in the Soultz reservoir.

Table 4-1: The fluid parameters with respect to the reservoir depth and in equilibrium with the mineral assemblage (after Durst and Vuataz, 2000). The electric charge of the species is left out.

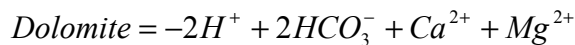
species	concentration [mol/kg]	species	concentration [mol/kg]
Na	$9.89 \cdot 10^{-1}$	Cl	1.71
K	$7.16 \cdot 10^{-2}$	SO ₄	$2.05 \cdot 10^{-3}$
Ca	$1.81 \cdot 10^{-1}$	HCO ₃	$1.40 \cdot 10^{-2}$
Mg	$4.59 \cdot 10^{-3}$	F	$2.09 \cdot 10^{-4}$
Al	$5.54 \cdot 10^{-6}$	SiO ₂	$3.44 \cdot 10^{-3}$
Fe	$4.64 \cdot 10^{-4}$		
temperature	165°C	pH	4.8

4.3.3 Mineral formation equations

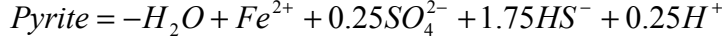
The basis for the composition of the rock matrix in the following models was the altered granite (Table 2-1, chapter 2.4.1). Since no parameters are known to calculate the aluminium activity coefficients, K-feldspar and clays could not be modelled. However, Jacquot (2000) showed that these minerals do not play a significant role. Thus, the Soultz system modelling accounts for the interaction of the formation fluid with calcite, dolomite, quartz and pyrite. Equation 4-26 to Equation 4-29 are the equations for the formation of these minerals. The calcite, dolomite and pyrite behaviour depend on the pH, since H^+ is involved in the formation equations: low pH values cause carbonates to dissolve, which consumes H^+ leading to increased pH values. Pyrite behaves in the opposite way.



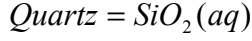
Equation 4-26



Equation 4-27



Equation 4-28



Equation 4-29

4.4 KINETIC MODEL OF THE SOULTZ SYSTEM

As previously discussed, for the Soultz system calcite, dolomite, pyrite and quartz are integrated in the geochemical model. To model the reaction rates a large number of parameters (m, n, s in Equation 4-21) are needed. These do not always exist. Especially for hot brines known parameters are limited. Thus, Durst (2002) built one kinetic law for each mineral dissolution and precipitation reaction. The laws derived from published experiments conducted in NaCl brines are briefly outlined below. Detailed information on the derivation of the reaction rate laws can be found in Durst (2002).

4.4.1 Calcite dissolution and precipitation

Far from the equilibrium the calcite dissolution rate is controlled by two processes the surface reaction and the diffusion of H^+ to the mineral surface (Sjöberg & Rickard, 1984). In the Soultz system both of the processes co-exist with a predominance of surface reaction. Equation 4-30 defines the calcite dissolution law accounting for the temperature, pH, surface reaction and dependency of the H^+ activity a_{H^+} . s is the reaction surface area.

$$r_d = \left[\left(1.643 * 10^{-1} * a_{H^+} + 1.11 * 10^{-5} \right) * s * \frac{T}{321.15} \right] * \left(1 - \frac{Q}{K} \right) * \exp \left(\frac{(T - 321.15) * (-65.98 * \ln a_{H^+} + 237.1)}{321.15 * T} \right)$$

Equation 4-30

Durst (2002) calculated the calcite dissolution rate for Soultz conditions based on Equation 4-30. The dissolution rate ranges between $5 * 10^{-5} \text{ mol/m}^3\text{s}$ to $5 * 10^{-4} \text{ mol/m}^3\text{s}$ and indicates that calcite dissolution occurs near the injection point due to the injection of fluid at 65°C.

The calcite precipitation law is based on the study from Shiraki & Brantley (1995) on near equilibrium kinetics at 100°C. The precipitation is dominated by spiral growth for $Q/K < 1.72$ and by nucleation at higher oversaturation. The inhibitor effect of magnesium (Zhang & Dawe, 2000) on calcite precipitation is not significant for the $\text{Ca}^{2+}/\text{Mg}^{2+}$ ratio of the Soultz fluid. Equation 4-31 defines the calcite precipitation rate.

$$r_p = 1.93 * 10^{-2} * T * \exp\left(\frac{-41840}{R * T}\right) * s * \left(\frac{Q}{K} - 1\right)^{1.93} \quad \text{for } \frac{Q}{K} < 1.72$$

$$r_p = 1.011 * T * \exp\left(\frac{-41840}{R * T}\right) * s * \exp\left(\frac{2.36}{\ln \frac{Q}{K}}\right) \quad \text{for } \frac{Q}{K} > 1.72$$

Equation 4-31

According to Durst (2002), in the Soultz system, the precipitation is around $10^{-5} \text{ mol/m}^3\text{s}$, which is one or two orders of magnitude smaller than the dissolution rate. Whereas dissolution is likely to occur near injection point, precipitation might take place in a wider zone. However, the competition between transport, reactions and temperature change does not allow any extrapolations without numerical simulations.

4.4.2 Dolomite dissolution and precipitation

The dissolution law is based on the work of Gauteliet et al. (1999). The temperature and pH dependent dolomite dissolution rate is

$$r_d = \left[10^{(-0.0436 * pH^2 - 0.5948 * pH - 2.0509) * s} * 2.104 * 10^7 * \exp(-2.754 * pH) * \exp\left(\frac{972 * pH - 5951}{T}\right) \right] * \left(1 - \frac{Q}{K}\right).$$

Equation 4-32

The rates for the Soultz system are two orders of magnitude lower than the calcite dissolution rate. However, dolomite is expected to dissolve near the injection point and probably also in a wider zone.

The dolomite precipitation law is derived from Arvidson & Mackenzie (1999):

$$r_p = 1.122 * 10^5 * s * \exp\left(\frac{-16060}{T}\right) * \left(\frac{Q}{K} - 1\right)^{2.26}.$$

Equation 4-33

The rates obtained for the Soultz system are several orders of magnitude lower than those of calcite. Thus, the calcite precipitation consumes all the Ca^{2+} and the CO_2 before dolomite is precipitated. Therefore, dolomite is not likely to precipitate in the Soultz system except if a significant increase of Mg^{2+} in the fluid occurs.

4.4.3 Quartz dissolution and precipitation

Dove (1994) derived a quartz dissolution equation depending on temperature and the pH.

$$r_d = \left[\exp^{-10.7 * T} * \exp\left(\frac{-66}{10^{-3} * R * T}\right) * \theta_{>\text{SiOH}} + \exp^{4.7} \right] * s * \left(1 - \frac{Q}{K}\right) * T * \exp\left(\frac{-82.7}{10^{-3} * R * T}\right) * (\theta_{>\text{SiO}_{\text{tot}}})^{1.1}$$

Equation 4-34

The quartz precipitation equation comes from Rimstidt & Barnes (1980).

$$r_p = \left[a_{\text{H}_2\text{O}}^2 * \exp\left(\left(1.174 - 2.028 * 10^{-3} * T - \frac{4158}{T}\right) \ln 10\right) \right] * s * \left(\frac{Q}{K} - 1\right)$$

Equation 4-35

$\theta_{>\text{SiOH}}$ is the fraction of the total surface sites occupied by hydrogen ions as $>\text{SiOH}$. And $\theta_{>\text{SiO}_{\text{tot}}^-}$ is the sum of the fraction of the total sites existing as deprotonated $>\text{SiO}^-$ site and as a complex with sodium ion as $>\text{SiO}^-\text{Na}^+$.

Given that the fluid in the Soultz reservoir is initially in equilibrium with regard to quartz at 165°C, injection of fluid at lower temperatures leads to oversaturation. Thus, quartz will only precipitate.

4.4.4 Pyrite dissolution and precipitation

The pyrite dissolution equation is derived from the studies by Williamson & Rimstidt (1994).

$$r_d = 250 * s * \exp\left(\frac{-6500}{R * T}\right) * \left(1 - \frac{Q}{K}\right)$$

Equation 4-36

Like quartz, pyrite will only precipitate due to oversaturation when injecting fluid at a temperature lower than 165°C.

The pyrite precipitation law is derived from studies by Rickard (1997) and Rickard & Luther (1997).

$$r_p = 0.125 * \frac{a_{HS^-} * a_{Fe^{2+}} * \sum S^{2-}}{K_{FeS} * (3 * K_{H_2S} + a_{H^+})} * V * \exp\left(\frac{-3500}{R * T}\right)$$

Equation 4-37

In Equation 4-37 V is the volume. The precipitation rate was calculated for the initial Soultz fluid as a function of temperature. Maximum precipitation around 135°C resulted. Yet, regarding the low rate values, this process is not likely to cause any significant change in the reservoir.

The behaviour of the components in the Soultz system described above, are based on theoretical kinetic estimations. However, such forecasts are assumptions, since neither the interaction of the different minerals nor the temperature, pressure and overall chemical processes were taken into account. To obtain more thorough results all relevant processes have to be considered. Only numerical modelling can do this. The next chapter describes the development of a coupled code that is created for numerical modelling.

5 THE COUPLED CODE FRACHEM

5.1 AIM OF COUPLING

The overall aim of this study is the simulation of the long-term HDR reservoir behaviour at the Soultz site. As previously pointed out, important consequences of storing and transporting heat and fluids in rocks give rise to significant coupling between thermal, hydraulic and chemical (THC) processes. To be able to predict reservoir performance these coupled processes have to be investigated simultaneously.

5.1.1 Governing processes and equations

Figure 5-1 schematically illustrates the coupling of the different processes and their interactions: temperature and pressure changes lead to chemical disequilibria in the reservoir, which may result in the precipitation or dissolution of several minerals. These chemical reactions alter the permeability of the fractured host rock and cause changes in fluid properties. The alteration of the permeability and the fluid properties have an impact on thermal transport, pressure field and fluid velocity. Herein, every process is coupled to the other processes and their interactions determine the long-term behaviour of the HDR reservoir.

The following conservation equations illustrate the coupling mathematically. The transient heat transport equation (Sauty, 1981) is

$$\frac{\partial}{\partial t}((\rho * c) * T) = -\nabla(\Phi * \rho_f * c_{pf} * v_f * T - \bar{\lambda} * \nabla T) + q_H.$$

Equation 5-1

T is the temperature, Φ the porosity, ρ_f the fluid density, c_{pf} the fluid heat capacity, v_f the fluid particle velocity and q_H a heat source. The crossed parameters are the

arithmetic means and contain values from the fluid and the solid phase. They are calculated depending on the phase fraction. $\overline{\rho^*c}$ is the arithmetic mean of the medium density and heat capacity

$$\overline{\rho^*c} = (1 - \Phi) * \rho_m * c_m + \Phi * \rho_f * c_f .$$

Equation 5-2

ρ_m is the density and c_m the heat capacity of the matrix (Pribnow, 1994). Accordingly, the arithmetic mean of the thermal conductivity $\bar{\lambda}$ is calculated

$$\bar{\lambda} = (1 - \Phi) * \lambda_m + \Phi * \lambda_f .$$

Equation 5-3

λ_m and λ_f are the thermal conductivities of the matrix and the fluid, respectively.

Following Clauser (1988), the thermal dispersion terms can be neglected in the above equations for two reasons: 1) it is difficult to obtain reliable diffusivity parameters and 2) in most of the cases diffusivity effects are negligible in comparison to other processes.

The transient hydraulic equation (Bear, 1979) is

$$\frac{\partial}{\partial t}(S_c * P) = -\nabla[K * (\nabla P + \rho_0 * g * \nabla z - \rho_0 * g * \nabla z * \beta_f * \Delta T)] .$$

Equation 5-4

S_c is the storativity, P pressure, K hydraulic conductivity, ρ_0 initial fluid density, g gravity, z depth, β_f thermal expansion coefficient. The first expression on the right represents diffusion and the second and third term buoyancy effects.

The transient chemical equation (Steefel & MacQuarrie, 1996) is

$$\frac{\partial}{\partial t}(\Phi * C_i) = -\nabla(v * C_i - \Phi * \tau * D_i * \nabla C_i) + q_i .$$

Equation 5-5

C_i is the concentration of a species i , v particle velocity, τ tortuosity of the medium, D_i diffusion coefficient and q_i a chemical source. The first term describes advective transport of chemical species and the second diffusive transport of chemical species. Sources represent newly composed species and sinks are the decay of chemical

species. It is assumed that mechanical dispersion can be neglected because a simple fracture system is treated.

The interaction of temperature, pressure and chemistry can be seen with the help of the mathematical expression in a more qualitative way. The influence of the hydraulic processes in the temperature equation is governed by heat advection. The temperature influences viscosity and density of the fluids, which has an effect on the pressure. Chemical reactions such as precipitation and dissolution have an impact on fluid temperature, permeability and thereby also on fluid velocity. Finally, pressure and temperature conditions determine the chemical behaviour of the system.

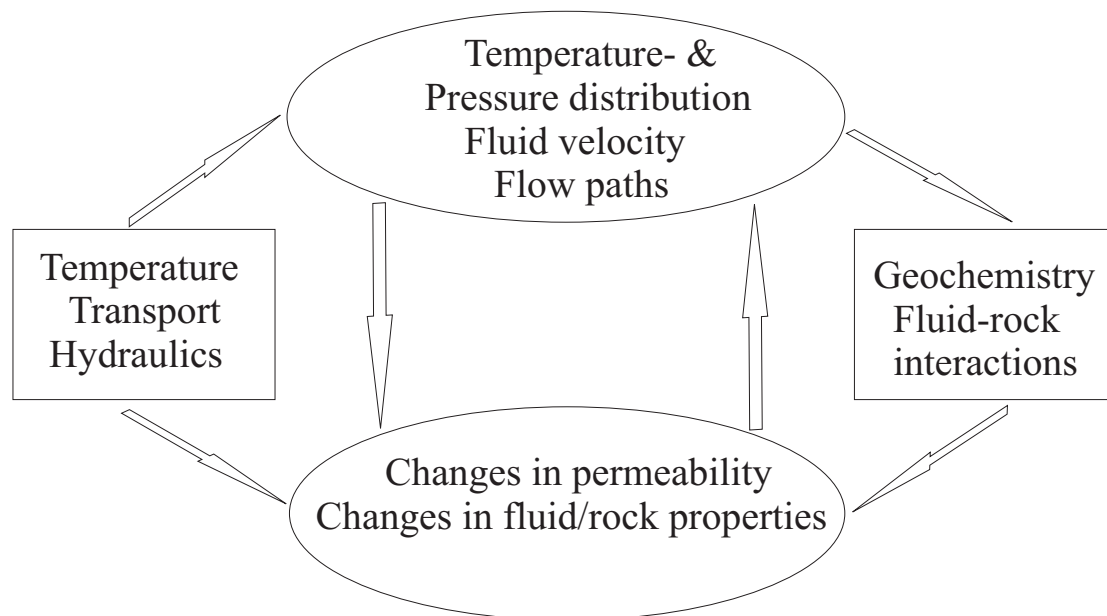


Figure 5-1: Schematic illustration of thermal, hydraulic and chemically coupled processes.

5.1.2 Coupling method

The numerical modelling of transient problems requires discretisation not only in space but also in time. A distinction is made between explicit and implicit methods for the discretisation in time. This difference applies for both the calculation of the single processes themselves and the coupling of the processes. Explicit approaches calculate the actual value of a parameter based only on the result from the preceding time step. The implicit approach also takes the actual value into account. This allows the calculation with larger time steps compared to explicit methods (Hughes, 1987). The processes are calculated with an implicit method. To couple thermal, hydraulic and chemical processes, different varieties of these methods come into consideration:

one-step (global implicit), sequential non-iterative (explicit) and sequential iterative (explicit) approach (Steeffel & MacQuarry, 1996).

In the one-step method the transport and the reaction equations are simultaneously solved. This yields the most exact results from a mathematical point of view. However, the size of the equation system to be solved restricts the system to only few aqueous species. The sequential non-iterative approach (SNIA) is simpler to implement. In this method, first the reaction equations are solved, then the fluid flow between the elements is calculated and finally the chemical species are transported from element to element. This method can lead to numerical instabilities, since the reaction rates calculated at time t are supposed to stay constant until $t+\Delta t$ without considering further chemical reactions due to changes in fluid composition and temperature during the interval Δt . To reduce such instabilities, time steps have to be small. A fully coupled solution is the sequential iterative approach (SIA) that iterates between reaction and transport. The reaction and the transport are considered as constant source terms. The iteration is done until the concentrations converge. This method is more elegant than the sequential non-iterative approach and can be used for systems containing multiple aqueous species. However, it is more complex and may fail to converge (Steeffel & MacQuarry, 1996).

5.1.3 Previous fluid-rock interaction studies at Soultz

Fluid-rock interactions at the Soultz reservoir were already subject of previous studies. Genter (1990) performed simulations based on thermodynamic equilibrium using the Debye-Huckel formalism. The results show that the interaction of the formation fluid with altered granite leads to granite dissolution and porosity increase. As stated above (chapter 4.2), thermodynamic equilibrium calculations set limits in possible processes and therefore, kinetics is needed to determine if reactions actually happen in a reasonable time. In addition, the Debye-Huckel approach is not very adequate to model the Soultz reservoir regarding the high salinity of the formation fluid (Durst, 2001).

The application of the Pitzer specific interaction for the Soultz system was first studied by Azaroual (1992). He highlighted the need of this approach but also stressed its difficulties. Yet in his studies, he simulated interaction of unaltered granite with distilled water and compared these results to experimental findings. Consequently, the

model is not representative for the Soultz reservoir, which consists of altered granite and highly saline fluids.

Jacquot (2000) carried out kinetic simulations of the interaction between altered granite and the formation fluid. The models contained the main minerals of the altered Soultz granite except sulphides and sulphates but including clay minerals. In his results he shows that the carbonates are the most reactive minerals in the Soultz HDR system. However, these models are still based on the Debye-Huckel formalism.

In short, the previous works were helpful in understanding the system but were not directly applicable for the intended coupled modelling. None of these models was able to simulate the thermal, hydraulic and chemical (THC) coupled processes for the conditions at the Soultz HDR system.

5.1.4 Existing THC coupled codes

To perform such representative simulations, an adequate computer program that allows the simultaneous modelling of THC coupled processes for temperatures up to 200°C and high saline fluids has to be used.

Geochemical kinetic modelling of hot brines is rarely done, especially when coupled with thermal and hydraulic processes. THC coupled codes exist only for either hot diluted fluids or cold brines: on the basis of *TOUGH2* (Pruess, 1991), *CHEMTOUGH* (White, 1995) and *TOUGHREACT* (Xu & Pruess, 1998) were developed. Both apply the Debye-Huckel approach to calculate the activity coefficients. *SHEMAT* (Clauser, 2003) in contrast uses the Pitzer equations, but is generally valid for temperatures up to 90°C. Other codes such as *CSP* (Matthai et al., 2001) integrate the Pitzer equations and are valid up to high temperatures but do not account for chemical kinetics.

Unfortunately, none of them entirely fulfils the claims for Soultz conditions. Consequently, a new THC coupled code has to be created. Instead of creating an entirely new one, two existing codes, *FRACture* (Kohl and Hopkirk, 1995) and *CHEMTOUGH*, were coupled. *FRACture* was chosen because it was developed especially to model the long-term behaviour of HDR reservoirs. The fact that the source code was available, was helpful. In 1999, when this work started, *SHEMAT* was only at the beginning of its development and therefore, *CHEMTOUGH* was chosen as basis for the coupling with *FRACture*. Both are briefly outlined in the

following. *SHEMAT* was used for comparative calculations and is discussed in a separate chapter (chapter 7).

5.2 FRACTURE

5.2.1 General

The finite element code *FRACTure* (Kohl and Hopkirk, 1995) is suited to simulate 3D models of coupled hydraulic, thermal and elastic processes and their interactions. Its name is an acronym for its functionalities: Flow, Rock And Coupled Temperature effects. The code was developed to model the long-term behaviour of HDR reservoirs (Kohl, 1992). It has also been successfully applied to a variety of applications such as the analysis of geoelectric measurements, radon transport (Kohl et al., 1994), solute tracer tests, simulations of borehole heat exchanger operations (Kohl et al., 2002), Alpine tectonics (Kohl et al., 2001) and hydrogeological system modelling (Kohl et al., 2000).

Figure 5-2 illustrates the physical coupling of the different processes. Hydraulic processes are treated as laminar Darcy flow including the Boussinesq assumption on density driven flow or as turbulent flow. Several thermal processes can be modelled: diffusion, fluid flow or mass advection, heat generation, dispersion and absorption for solute transport. The elastic processes account for stress perturbations arising from linear poro- or thermo-elastic effects in the rock matrix and from a non-linear stress dependent on the joint closure law. *FRACTure* allows thermal, hydraulic or rock mechanical processes to be turned off at any time. In all of the following simulations the elastic processes are turned off, since the focus of this study is the thermal, hydraulic and chemical (THC) coupling.

5.2.2 Numerical implementation

The basic mass- and energy-balance equations are discretized in time using the finite difference type Newmark method (Hughes, 1987). In Figure 5-3 a coupled time step is shown: all thermal and hydraulic data are known at the beginning of a time step. First the pressure field and velocities are calculated: the buoyancy velocity v_a and the dynamic viscosity μ are updated from the temperature. Non-linear fracture elements as well as linear matrix elements are included in the iteration. The calculation yields the hydraulic fracture aperture a_k , the conductivity of the fracture hydraulic K_k and the

pressure field P in fracture and matrix. Then, the temperature distribution in fracture and matrix is calculated based on the fluid velocity v_f resulting from the pressure field.

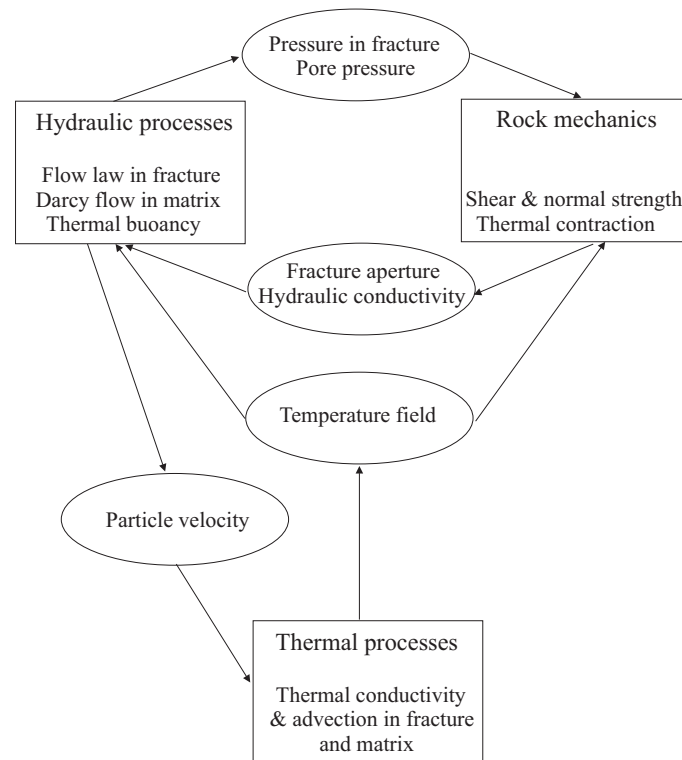


Figure 5-2: The physical coupling of thermal, hydraulic and elastic processes in FRACTure (Kohl, 1992).

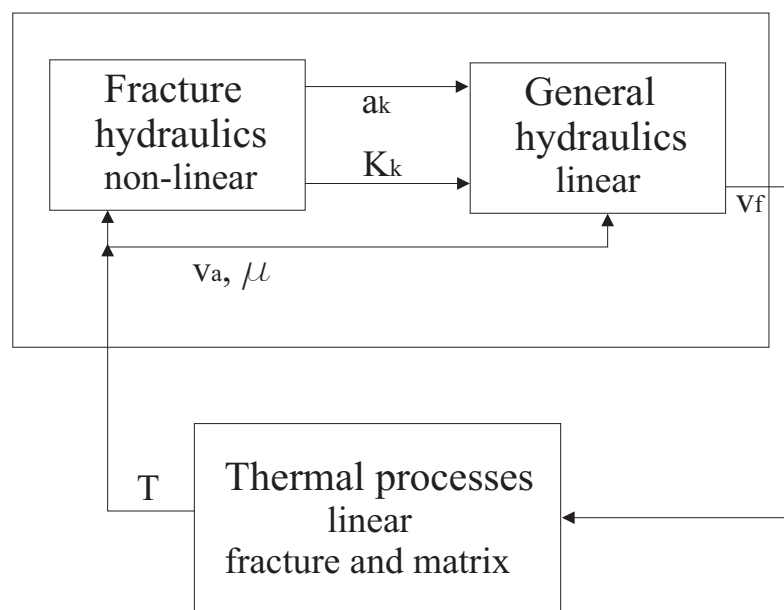


Figure 5-3: Coupling mechanism of a coupled time step in FRACTure (Kohl, 1992).

The Galerkin discretization of the advection term raises difficulties for numerical codes. These problems can be sized by two different dimensionless constants. The temporal constant called Courant number Cr indicates the number of element lengths ΔL that are passed within one time step Δt

$$Cr = \frac{v * \Delta t}{\Delta L}.$$

Equation 5-6

The spatial constant is called Peclet number Pe and indicates the ratio between the effect of advection and diffusion

$$Pe = \frac{(\rho c_p)_f * v * \Delta L}{\lambda}.$$

Equation 5-7

The accuracy of a numerical model depends on the size of these constants. Fluid velocity, spatial discretization and time step sizes very much affect the size of the constants: higher velocity increases both Cr and Pe . Larger time steps increase Cr . Smaller elements increase Cr and decrease Pe . Only in explicit methods the seize of Cr is critical. Empirical formules indicate that for 1D models inaccuracies are in an acceptable range when $Cr < 1$ and $Pe < 10$ for finite element solutions.

FRACture comes along with the graphical mesh generator program *WinFra* that creates complex 2D or 3D finite element meshes. Special emphasis is on the discretization of irregular finite element networks. Several interfaces have also been developed to import external DXF files or digital terrain models.

5.3 CHEMTOUGH

5.3.1 Original CHEMTOUGH

CHEMTOUGH (White, 1995) is a geochemical code based on the finite volume code *TOUGH2*, which is a further developed version of the geothermal reservoir simulator *TOUGH* (Pruess, 1991). *TOUGH* is the abbreviation of ‘Transport Of Unsaturated Groundwater and Heat’. It is a 3D numerical code to simulate the coupled transport of water, vapour, non-condensable gas and heat in porous and fractured media. The basic mass- and energy-balance equations for an arbitrary flow domain are discretized in space using the integral finite difference method (Edwards, 1972; Narashiman &

Witherspoon, 1976) and in time fully implicitly as a first order finite difference. The resulting equations are strongly coupled because of the interdependence of mass. *TOUGH2* performs a simultaneous solution of the discretized equations, taking all coupling terms into account. A choice of sparse direct solver or various preconditioned conjugate gradient algorithms are available for solving linear equations. Thermophysical properties of water, steam and CO₂ are represented. Injection or withdrawal of heat and fluids can be modelled. Double-porosity, dual-permeability and multiple interacting continua methods are available to model flow in fractured porous media. The basic equations are conservation laws in the form of

$$\frac{\partial Q_{t_{in}}}{\partial t} = -\nabla F_{in} + qr_{in}.$$

Equation 5-8

$Q_{t_{in}}$ is the quantity of component i (water, steam, gas or heat) in the volume element. ∇F_{in} is the variation of $Q_{t_{in}}$ due to transport and qr_{in} is the variation of $Q_{t_{in}}$ due to reactions in the volume element such as heat exchange, condensation or injection.

In *CHEMTOUGH*, the possibilities to transport chemical species and to model fluid-rock interactions driven by pressure and temperature changes are added. Transport and reaction are coupled using a one-step approach. For each chemical species one equation of the type of Equation 5-8 is inserted. The species can be transported via advection or diffusion (no dispersion). The geochemical part of the code calculates the qr_{in} terms for the chemical species. The model is appropriate to describe many reactions that take place in a geothermal reservoir. Four possible reaction types are implemented: 1) equilibrium reactions in aqueous phases using the Debye-Huckel concept to calculate the activity coefficients, 2) gas-liquid reactions and liquid-solid reactions with precipitation and dissolution, 3) simple formalisms are implemented to model kinetic reactions and 4) the effects of porosity changes on the permeability using a simple empirical equation for porous rocks. The chemical reactions are considered by adding a CHEM block to the *TOUGH2* input.

5.3.2 Modified CHEMTOUGH/geochemical FRACHEM module

The characteristics of the Soultz system, such as the high salinity of the fluids and the re-injection of the fluid after production, preclude the use of the original geochemical model implemented in *CHEMTOUGH*. Thus, Durst (2002) made several

modifications. These are described in detail in Durst (2002) and summarized hereafter.

To account for the high salinity of the fluids, the Debye-Huckel approach was replaced by the Pitzer formalism to calculate the activity coefficients. The polynomial coefficients for the activity coefficient calculation are given in one of the input files (chem.dat). Appendix A describes the various input files.

CHEMTOUGH contained simple kinetics for most mineral reactions. Some mineral reactions like carbonate minerals were not included. However, as discussed in chapter 4.3.1, the use of the Pitzer approach raises new problems such as the lack of parameters for aluminium and Mg^{2+} and Fe^{2+} at higher temperatures. Thus, only calcite, dolomite, pyrite and quartz could be integrated into the model (see chapter 4.3.3). The new kinetic laws for these minerals were implemented accordingly, which also required modifying the calculations of the reaction surface. Other minerals like feldspar, anhydrite and hematite are intended to be incorporated in the model at a later stage. The kinetic modelling of clays had also to be postponed due to the lack of available data and the complexity of the model including variable composition minerals.

The empirical equations to calculate the effect of porosity changes on permeability were replaced. Since the fluid circulation in the Soultz system occurs in clusters of fractures and highly altered granite, two types of porosity models were considered: the fracture- and the grain-type porosity model. In the fracture-type porosity model, circulation occurs in fractures filled with a constant thickness layer of reactive minerals. In the second model, the fluid circulates in the interstitial space between spherical grains of reactive minerals. The implemented porosity-permeability relation accounts for both models and was developed after the fracture type porosity model of Northon & Knapp (1977) and the grain model after Bolton et al. (1996). In addition, the conversion of the permeability k into the hydraulic conductivity K

$$K = \frac{k}{\mu}$$

Equation 5-9

and vice versa is implemented to interact with FRACTure that calculates hydraulic processes based on hydraulic conductivity rather than on permeability. Note that in

groundwater hydraulics, the numerator is multiplied by the fluid density and the gravity constant.

To calculate the dynamic viscosity μ the relation of Smith & Chapman (1983) is used

$$\mu = 2.4 * 10^{-5} * 10^{\left(\frac{248.37}{T+133.15}\right)}.$$

Equation 5-10

Produced fluids in HDR systems are re-injected after being cooled in the surface heat exchanger. *CHEMTOUGH* did not allow the concentration of the species in the injected fluid to be continuously altered unless it was manually changed after each time step, which was a time consuming procedure. Some modifications were made so that re-injection of produced fluids is now possible with *CHEMTOUGH*.

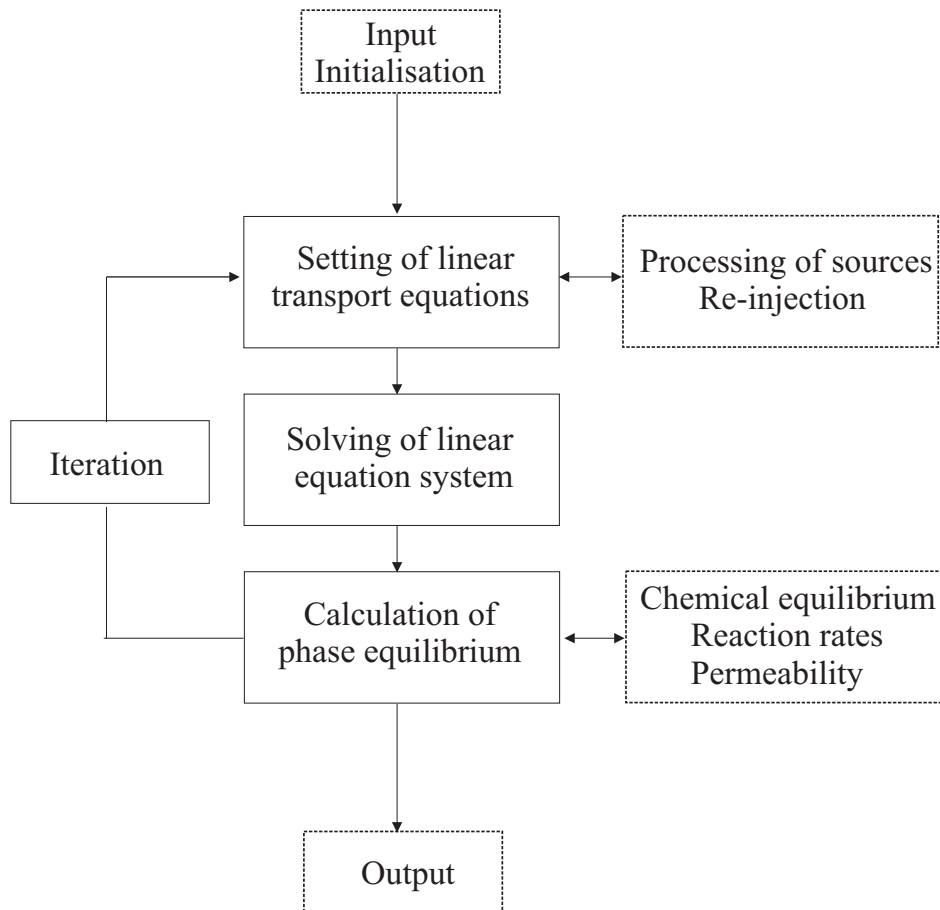


Figure 5-4: Flow chart of the modified *CHEMTOUGH* (=geochemical module of *FRACHEM*). The dashed boxes highlight the modified parts (Durst, 2002).

Finally, two types of new output files are generated. One output file (chem_output.dat) lists the temperature, pressure, porosity, permeability, pH,

concentrations of species and the reaction rates at distinct time steps. The second type of output file (mon_node_elX.dat) prints, for specified elements, a file in a format that is readable by *Tecplot*. These files monitor the temporal evolution of the above parameters. Examples of output files are given in Appendix A. Figure 5-4 illustrates the flow chart of the modified *CHEMTOUGH*. In the following the modified *CHEMTOUGH* is called geochemical module of *FRACHEM*.

5.4 COUPLING FRACTURE AND CHEMTOUGH TO FRACHEM

An explicit method (SNIA) (chapter 5.1.2) was chosen to couple *FRACtUre* and *CHEMTOUGH* to *FRACHEM*. Each hydraulic and thermal step is followed by a chemical step. Figure 5-5 illustrates the flow chart of *FRACHEM*: first *FRACtUre* reads the geometry and the model setting information from the input.dat file. Then the thermal and hydraulic processes are calculated as described in chapter 5.2.2 and illustrated in Figure 5-3. This yields the temperature T and pressure P distributions as well as the fluid velocities v_f . Since *FRACtUre* is a finite element code and *CHEMTOUGH* a finite volume code, an interface was written to unify the different geometrical information required by both codes. The interface also calculates the amount of fluid V transported from element to element based on the fluid velocities from *FRACtUre* and the geometry in the chem_input.dat file. Finally, *CHEMTOUGH* reads the chem.dat file and calculates the chemistry subject to temperature, pressure and transported fluid amount. The precise process was described in chapter 5.3.2 and illustrated in Figure 5-4. The resulting porosity Φ and hydraulic conductivity K are given back to *FRACtUre* and the cycle restarts. There is an option not to update Φ and K in *FRACtUre* (see Appendix A). This option was implemented to test the single modules (see chapter 5.4.3).

Below, the preparations for the coupling of *FRACtUre* with the geochemical module of *FRACHEM* (changes in WinFra and development of the interface) and the new code *FRACHEM* are illustrated.

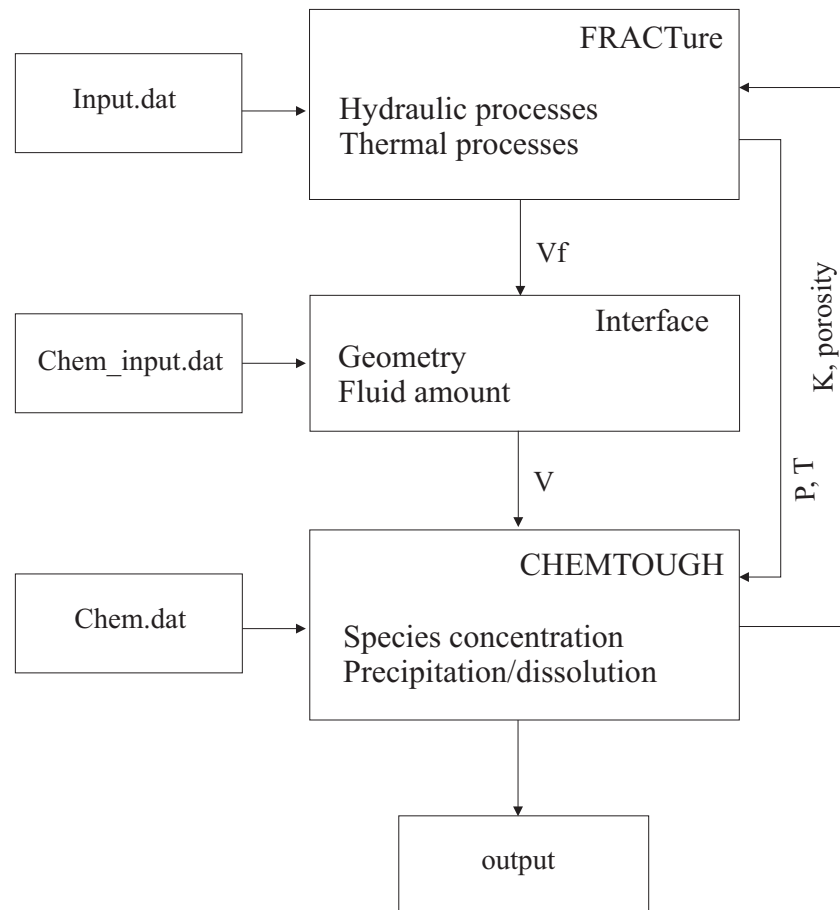


Figure 5-5: Simple schematic flow chart of FRACHEM.

5.4.1 Extension of WinFra

Two features were added to WinFra: 1) the option to save the model geometry as *TOUGH2* input (tough2_input.dat) and 2) the possibility to create a *FRACHEM* interface input file (chem_input.dat).

To simplify the setting of the *TOUGH2* geometry input for the Rhine Graben study an additional feature was added to *WinFra*. This feature allows to:

- generate 1D, 2D and 3D *TOUGH2* input meshes directly in *WinFra* or via imported external DXF files
- sources and boundary conditions are directly added to the input
- automatically refine the model
- generate an additional file to simplify visualising the results.

In the mean time an additional interactive pre- and postprocessor for *TOUGH2* (and other codes) called *PetraSim* was developed (Swenson et al., 2002).

Although *WinFra* is capable of creating *TOUGH2* input files for irregular mesh geometries, it is not recommended to do so. This is because the finite volume method implemented in *TOUGH2* is not very accurate with irregular meshes (Bächler et al., 2001).

The second feature that was added to *WinFra* is the creation of the *chem_input.dat* file. The *FRACHEM* interface needs this file to provide *CHEMTOUGH* the required geometrical information for its finite volume calculations. Based on this information, the *FRACHEM* interface determines the amount of fluid that is transported from element to element. *Chem_input.dat* lists:

- element number
- co-ordinates of its mid points
- connection of the elements
- interface area between two neighbouring elements
- co-ordinates of three interface vertices.

WinFra is capable of creating regular and irregular mesh geometries containing 1D, 2D and 3D elements. Note that at this stage, models with 1D elements in combination with 2D or 3D elements cannot be calculated with *FRACHEM* since the code is only designed to treat one element type. In addition, it is not recommended to work with irregular models. The reason for this will be illustrated in the next section. The format of the *chem_input.dat* is described in Appendix A.

5.4.2 Interface

To couple *FRACtUre* and *CHEMTOUGH* an additional interface was created. It has two functions: 1) to convert the geometry information from finite elements into finite volume and 2) to calculate the amount of fluid that is transported from element to element. The interface consists of several subroutines that are called during the program sequence. The main subroutines are *INTERFACE_init*, *INTERFACE_Advection* and *CalculateAdvection*. Figure 5-7 illustrates their position in the program sequence.

INTERFACE_init reads the number of elements and the co-ordinates of the element midpoints (Mp 1, Mp 2) and counts the number of connections between the elements from the *chem_input.dat* file. In addition, it builds up the element neighbourhood information: for each element to element connection, three points of the interface area

are saved together with the element number of the connected elements. In addition, all element connections are identified. *INTERFACE_Advection* reads the x, y and z-component of the advection for each element from the advX.dat files.

CalculateAdvection determines the amount of fluid V that is transported from element to element depending on the inclination of the interface area. Figure 5-6 illustrates the geometrical situation. First, the norm \vec{n} of the interface area between two neighbouring elements (E 1 and E 2) is calculated. Then, the angle α between \vec{n} and the distance \vec{d} between the two element midpoints is computed. v_x and v_y are the x- and y-components of the fluid velocity in element E 1. The true fluid velocity v_x' from element E 1 to E 2 is the projection of v_x onto \vec{n} . The relation between v_x and v_x' is

$$|\vec{v}_x'| = |\vec{v}_x| * \cos \varphi .$$

Equation 5-11

$\cos \varphi$ can be calculated by

$$\cos \varphi = \frac{\vec{n} * \vec{v}_x}{|\vec{n}| * |\vec{v}_x|} .$$

Equation 5-12

Introducing $\cos \varphi$ into Equation 5-11 leads to

$$|\vec{v}_x'| = \frac{\vec{n} * \vec{v}_x}{|\vec{n}|} .$$

Equation 5-13

Finally, multiplying v_x' by the interface area yields the fluid amount V that is transported from E 1 to E 2.

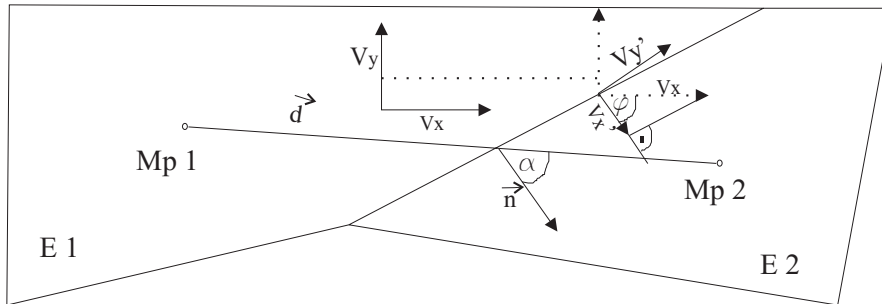


Figure 5-6: Scheme for calculation of fluid flow between two irregular elements.

5.4.3 FRACHEM

FRACture and the geochemical module of *FRACHEM* were now coupled to *FRACHEM*. Figure 5-7A to C illustrates the elements of *FRACHEM*. The file management of all input and output files during the simulation is done at the beginning (Figure 5-7A). Here, all input information is read such as the *Input.dat* for the *FRACture* part, the *chem_input.dat* for the interface and the *chem.dat* for the *CHEMTOUGH* part. Then, the main subroutine *FRACHEM_driver* is called. In the figure, all subroutines are underlined.

Figure 5-7B describes the *FRACHEM_driver*. A transient *FRACHEM* run consists of several time intervals. These consist of a certain number of time steps. The *FRACHEM_driver* loops over intervals and single time steps. First, the hydraulic and the thermal processes are calculated as illustrated in Figure 5-3. This yields the *disX.dat*, *advX.dat* and *hflX.dat* files. Then, the subroutines *Interface_Advection* and *CalculateAdvection* are called to compute the fluid amount that is transported from element to element. Finally, the *CHEMTOUGH* subroutines *main_chem* and *chem_output* are evoked.

main_chem is illustrated in Figure 5-7C. The reactive transport is calculated in three steps: the thermodynamic equilibrium and the reaction rates r_1 are evaluated by subroutine *Chemical_state*. *Steady_reaction* computes the concentration variation of the species and *Chemical_transport* fulfils the advective transport of the chemical species. To improve the stability of the SNIA method, *Chemical_state* is called twice to determine the thermodynamic equilibrium and the reaction rates r_2 after the transport. Then, the concentrations of the species are reset to the ones at the beginning of the chemical time step. *Steady_reaction* is called again to calculate the species concentration due to the averaged reaction rate $(r_1 + r_2)/2$ and *Chemical_transport* transports the chemical species. Additional controls were inserted in the code to prevent the species concentrations from becoming negative, which would cause the solver to fail. Finally, the effect of the fluid-rock interaction on porosity, permeability and reaction surface areas is computed by the subroutine *Permeability_change*. *chem_output* writes the *chem_output.dat* and *mon_node_elX.dat* files.

Note that to save simulation time *main_chem* is only executed for the so-called active elements. At the beginning of the simulation, all elements with porosities higher than a predefined boundary value (5%) are set to active elements, since reactive transport occurs mainly in fractures. All other elements ignore any reactive transport.

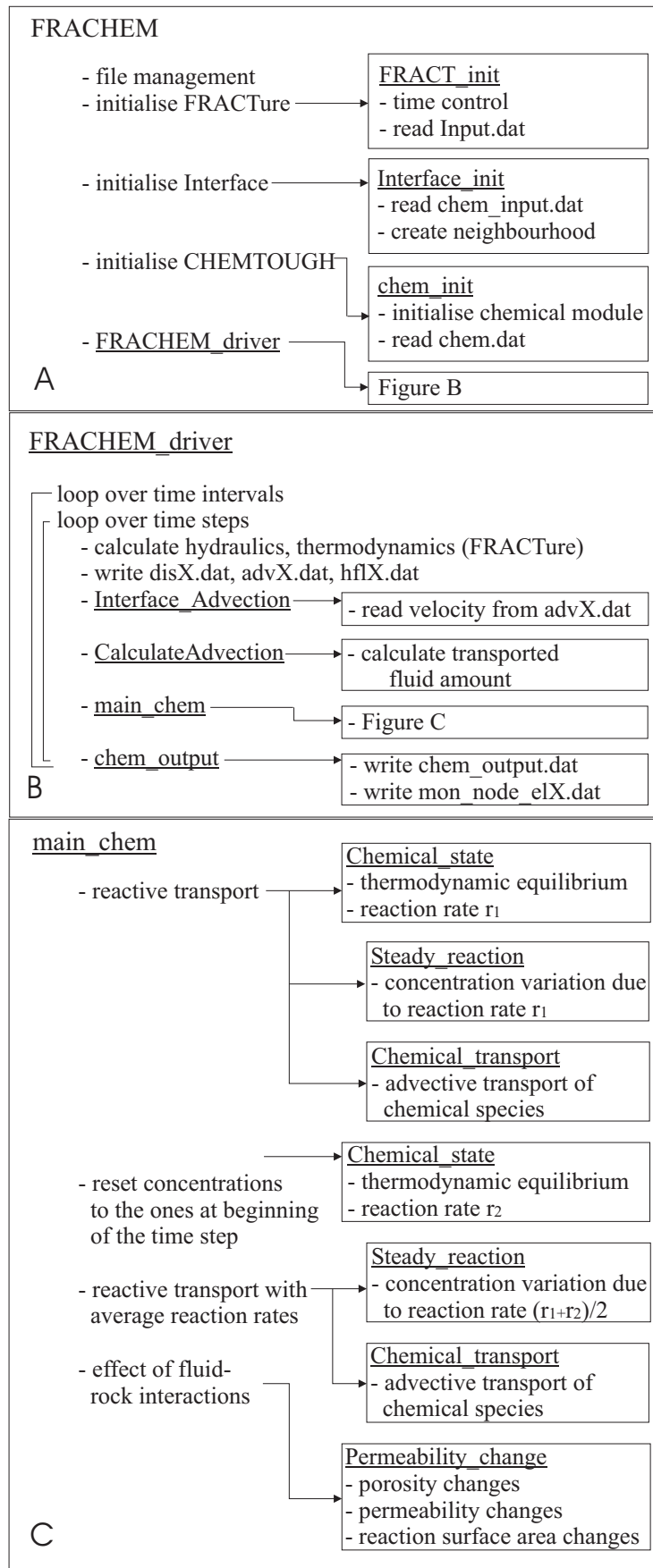


Figure 5-7: Elements of FRACHEM. Figure A shows the main program FRACHEM. Figure B illustrates the subroutine FRACHEM_driver and figure C main_chem.

5.5 FIRST FINDINGS USING FRACHEM

Durst (2002) performed several model runs with *FRACHEM*. Below, the main findings are summarized.

5.5.1 Thermodynamic calculation of reaction potential of the system

The geochemical module of *FRACHEM* was used to estimate the maximum potential amount of mineral precipitation and dissolution of calcite, dolomite, quartz and pyrite that might occur when cooling the Soultz fluid from a temperature of 165°C to 65°C. In each simulation only one mineral reaction was allowed.

Table 5-1 lists the amount of mineral precipitation or dissolution per kg of fluid. The amount was extrapolated for one year assuming an injection rate of 25 l/s corresponding to the 1997 circulation test (see chapter 2.1.1). These thermodynamic simulations show that the dissolution of the carbonates seems to be significantly more important than the precipitation of quartz and pyrite, and will lead to increased porosity and permeability.

Table 5-1: Maximum potential amount of mineral precipitation and dissolution out of a total fluid volume of $7884 \cdot 10^5$ l ($=25$ l/s $\cdot 3.15 \cdot 10^7$ s). (d) and (p) indicate dissolution and precipitation, respectively (Durst, 2002).

mineral	amount per kg fluid [mg]	amount per year [kg]	amount per year [m ³]
calcite (d)	590	460'000	170
dolomite (d)	535	420'000	155
quartz (p)	98	80'000	30
pyrite (p)	29	22'000	4

5.5.2 1D fracture model with the geochemical module of FRACHEM

To test the geochemical module of *FRACHEM*, chemical reactions along a 1D fracture of 1200 m length were modelled for a time period of ten years. At one end of the fracture, fluid was injected at a temperature of 65°C. On its way to the production well at the other end of the fracture, it was progressively heated to a temperature of 165°C. The rock matrix was assumed to consist of calcite, dolomite, quartz and pyrite (see chapter 4.3.3). For this pure geochemical test calculation, the fluid temperature and flow field remained unchanged despite the modelled permeability variation.

The injection of cold fluid creates a chemical non-equilibrium, which induces dissolution of calcite and dolomite as well as precipitation of quartz and pyrite (see

chapter 4.4). The results show that the main chemical process are the fluid-calcite reactions that lead to porosity and permeability increases near the injection point, due to calcite dissolution. Because of the progressive temperature increase along the fracture, precipitation of calcite occurs towards the production point.

The simulation results compare well with qualitative expectations from theoretical kinetic calculations (chapter 4.4). Under steady-state hydraulic and thermal conditions, the geochemical module of *FRACHEM* works properly. Still this does not represent real HDR conditions. Therefore, further coupled models need to be calculated with *FRACHEM* to test the transient temperature and pressure development.

5.5.3 2D fracture models with FRACHEM

The first complete application of *FRACHEM* was a 2D fracture model in which some aspects of the Soultz HDR reservoir are incorporated. The model consists of a single 50 m long, 1 m wide and 1 m deep fractured zone surrounded by rock matrix. The initial temperature in the model is 165°C, which corresponds to the temperature at 3500 m depth in the reservoir (see chapter 2.3.2). At one end of the fracture fluid at $q_{inj} = 4 \cdot 10^{-3}$ l/s at $T_{inj} = 65^\circ\text{C}$ is injected. The production well is placed at the other end. The pressure at the production point was held constant at 25 MPa (bottom well pressure at GPK2). Now the thermal and chemical processes were coupled; but still, the porosity and permeability changes did not affect the hydraulic field. The simulation time was 6.4 years.

With the assumed parameters ($K_k = 10^{-6}$ m²/Pas, $\lambda = 2.2$ W/mK) the entire fracture has nearly cooled down to the injection temperature after 6.4 years. As in the previous model, calcite dissolves near the injection point at a maximum rate of 10^{-4} mol/m³s and precipitates at maximum $2.5 \cdot 10^{-4}$ mol/m³s at the production well. With increasing simulation time, the dissolution zone moves towards the production point. Near the injection well all calcite has dissolved after one year with a reaction rate reducing correspondingly to zero. In contrast, dolomite never precipitates. At the beginning of the simulation, dissolution only takes place near the injection point at a maximum rate of $6.5 \cdot 10^{-5}$ mol/m³s. After one month, the dissolution zone spreads and moves towards the production point similar to the calcite behaviour and the reaction rate decreases to $0.8 \cdot 10^{-5}$ mol/m³s.

These results show the interdependence of the pH, temperature and carbonate behaviour (see chapter 4.4): the cold fluid at low pH dissolves calcite and dolomite near the injection well at a high rate. Reheating the fluid causes the calcite to precipitate and the pH to rise. Since the calcite precipitation rate is higher than that of dolomite, calcite precipitation prevents the precipitation of dolomite. According to the temperature evolution in the fracture, this process moves towards the production well and the reaction rates decrease. With increasing reaction time, the reaction rates reduce strongly due to the decrease of available carbonates. At the beginning, the dissolution of dolomite is controlled by temperature, whereas with time it depends more on calcite precipitation.

Quartz precipitates in the fracture at a maximum rate of $6 \cdot 10^{-7} \text{ mol/m}^3\text{s}$. At the beginning of the simulation the maximum reaction rate is near the injection well. Depending on the temperature evolution, with time it moves towards the production point and decreases to $10^{-7} \text{ mol/m}^3\text{s}$. Pyrite has similar behaviour and precipitates at maximum $4 \cdot 10^{-12} \text{ mol/m}^3\text{s}$. Unlike quartz, some punctual dissolution events occur. These differences are due to the fact that even if the pyrite reaction depends on the temperature evolution, there is still an influence from the pH. Like in the previous model, porosity and permeability increase near the injection point due to dissolution of carbonates and decrease near the production point due to calcite precipitation. After 6.4 years the maximum porosity is 16% and the minimum is 7%, down from initially 10%.

A more complex model consisted of two fracture zones of different widths. The model results are similar to those from the single fracture model with both fractures showing the same behaviour.

Both models are very simple and clearly do not represent the situation at Soultz. No model sensitivity analyses were conducted and the models were not yet fully coupled. In the following chapters fully coupled models of the Soultz HDR reservoir were developed and the model sensitivity was tested.

6 SENSITIVITY ANALYSES

The new code *FRACHEM* was tested to investigate its numerical behaviour. Different sensitivity analyses were performed. They are described in this chapter. The primary focus is to evaluate the capacity of the code and the model sensitivity. The details of the simulation results are of secondary importance. Detailed discussion of the results can be found in chapter 8 where the same model is used for a long-term simulation.

Below, the numerical model, its geometry, model parameter and initial- and boundary conditions are introduced. Then, this model was used to investigate the model sensitivity and the capacity of the code. Therefore, thermal-, hydraulic- and chemical processes were coupled step by step. Four different model simulations were done: in model 1 temperature and hydraulic processes were coupled. In model 2 chemical processes were also taken into account to calculate equilibrium concentrations at 165°C. The coupling between chemistry and hydraulic processes was deactivated. Model 3 simulated temperature, hydraulic and chemical kinetic processes still without coupling chemistry and hydraulic processes. Finally, in model 4 all processes are coupled.

6.1 NUMERICAL MODEL

6.1.1 Model geometry, initial- and boundary conditions

Figure 6-1 sketches a simplified physical model of the Soultz reservoir: the injection and the production well are connected through fractured zones surrounded by a granitic matrix. The zones are 0.1 m wide, 10 m deep and have a porosity Φ of 10 %. Each zone consists of several fractures. One of these fractured zones is modelled. For simplicity, below the term ‘fracture’ is used rather than ‘fractured zone’ throughout

the work. All of the following sensitivity analyses were performed with the same model geometry.

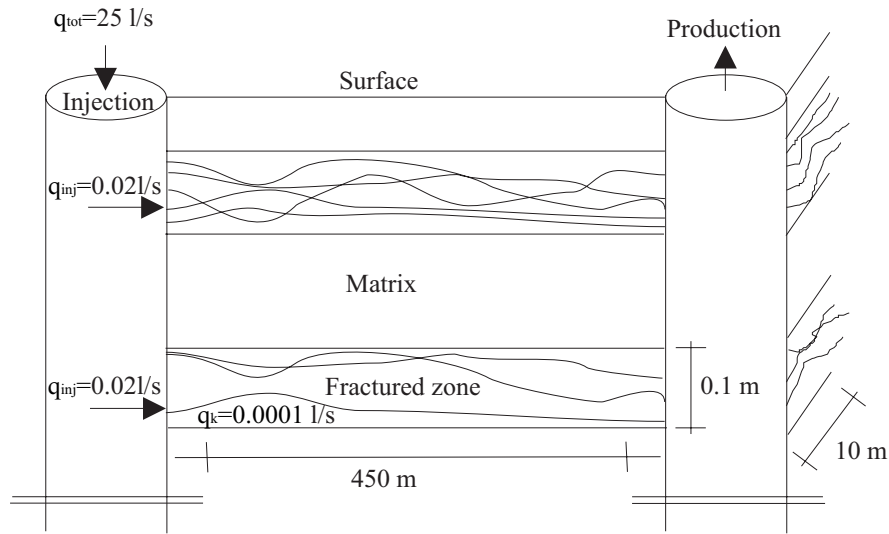


Figure 6-1: Simplified physical model of the Soultz reservoir.

Figure 6-2 shows the geometry of the numerical model. Near the injection (at $x = 50$ m) and the production point (at $x = 500$ m) the discretization of the mesh is finer than elsewhere. The upper model illustrates the area around the injection point and the fracture (black). The area around the production well has the same geometry. The lower model represents the entire model. The roughest mesh has 198 rectangular quadrilateral elements consisting of 238 nodes. Finer models were also calculated to test the influence of the discretization (see chapter 6.2.2 and 6.4.3). Since the model is symmetric to the x -axis, only the upper part of the model was simulated to save calculation time.

The initial temperature was set to 165°C (reservoir temperature at 3500 m depth) and Dirichet boundary conditions were applied to the upper, left and right boundary. A constant over-pressure of 2 MPa was assumed at the injection well and hydrostatic conditions at the production. In each of the fractured zones fluid was injected at $q_{inj} = 2 \cdot 10^{-2} \text{ l/s} = 2 \cdot 10^{-5} \text{ m}^3/\text{s}$ and a temperature of 65°C . The injection rate for each fracture was $q_k = 10^{-4} \text{ l/s} = 10^{-7} \text{ m}^3/\text{s}$. This is based on the fluid production rate $q_{tot} = 25 \text{ l/s}$ (1997 circulation test) and assuming 1250 fractured zones ($q_{tot}/q_{inj} = 1250$ fractured zones) consisting of 200 fractures.

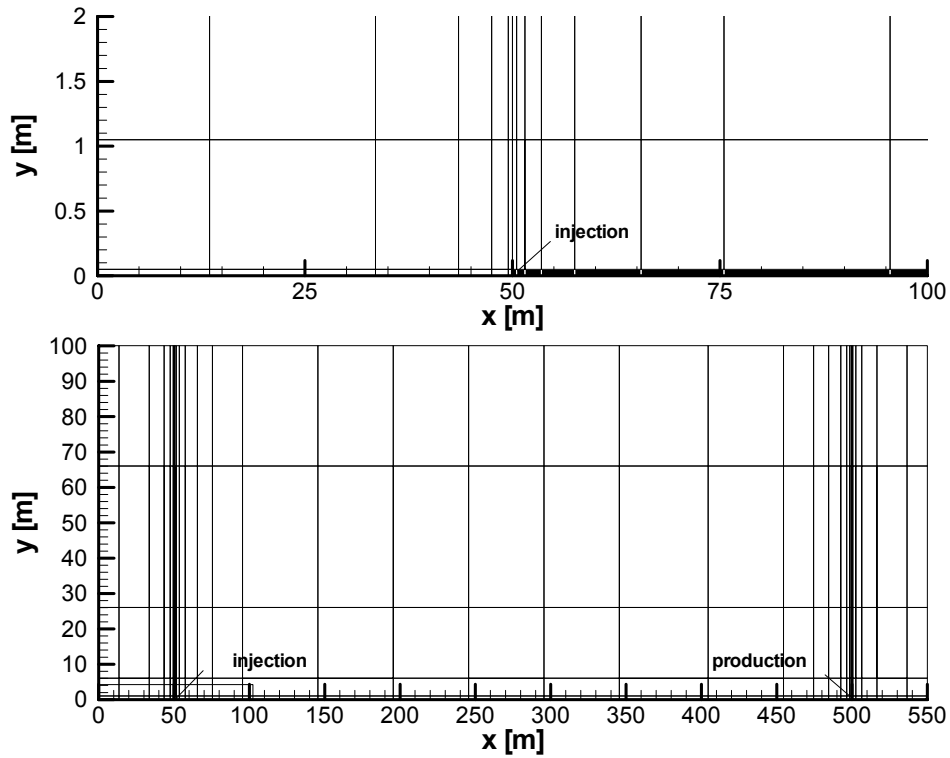


Figure 6-2: Model geometry of the Soultz reservoir at 3500 m depth. The upper model shows the finer mesh discretization around the injection well. The black bar represents the fracture. The lower model illustrates the entire model.

6.1.2 Hydraulic and thermal model parameters

The hydraulic model parameters are calculated following empirical laws from laboratory experiments that measured flow rates through fractures as function of the pressure gradient (Bear, 1979). For 1D parallel flow through fractures, the relation between the injection rate q_{inj} , pressure gradient ∇P , transmissivity Tr_{tot} and the fracture depth L is the following:

$$Tr_{tot} = \frac{q_{inj}}{L * \nabla P}$$

Equation 6-1

Thus, the total transmissivity of the fractured zone is $Tr_{tot} = 2.25 \cdot 10^{-10} \text{ m}^3/\text{Pas}$. This is the sum of the fractures' transmissivities Tr_k within the zone. The fracture aperture a_k can be calculated with the cubic law for laminar fracture flow between parallel, flat planes:

$$a_k = \sqrt[3]{12 \cdot \mu \cdot Tr_k}$$

Equation 6-2

Note that in reality, near the well the flow is turbulent. This is neglected in the following. μ is calculated by Equation 5-10. At 165°C $\mu = 1.63 \cdot 10^{-4} \text{ Pas}$ and the resulting $a_k = 1.3 \cdot 10^{-5} \text{ m}$. Equation 6-3 leads to the hydraulic conductivity of the fracture K_k .

$$K_k = \frac{Tr_k}{a_k}$$

Equation 6-3

The fluid flow in the matrix is negligible due to low hydraulic conductivity and zero matrix porosity. Thus, all chemical reactions happen in the fracture, whereas in the matrix no reactions take place.

The thermal model parameters are calculated by Equation 5-2 and Equation 5-3. No radiogenic heat production was integrated in the model. Table 6-1 lists the resulting parameter values for the matrix, fracture and fluid.

Table 6-1: Physical model parameters for matrix, fracture and fluid.

parameter		fracture_k	matrix_m	fluid_f
hydraulic conductivity K	[m ² /Pas]	$8.5 \cdot 10^{-8}$	10^{-15}	-
porosity Φ	[%]	10	0	-
thermal conductivity λ	[W/mK]	2.9	3	0.6
density ρ	[kg/m ³]	-	2650	995
heat capacity c_p	[J/kgK]	-	1000	4200
ρc_p	[J/Km ³]	$2.73 \cdot 10^6$	$2.65 \cdot 10^6$	$4.2 \cdot 10^6$
storativity S_c	[1/Pa]	10^{-10}	10^{-10}	-
transmissivity Tr	[m ³ /Pas]	$1.12 \cdot 10^{-12}$	10^{-15}	-

6.1.3 Simulation mode

A model simulation run consists of several time sequences with different numbers of time steps. All models have two preceding time sequences. During the first, only the steady-state temperature field is calculated to set the initial temperature in each element to 165°C. In the second time sequence, only steady-state pressure and velocities are calculated to evaluate the initial pressure distribution. After the first two time sequences, fluid at a temperature of 65°C at 0.02 l/s is injected during all following time sequences. The produced fluid flows through a buffer, which represents the mixing of the fluid volume contained in wells and surface installations, before being re-injected.

Steady-state pressure is assumed for all simulations, since it is reached after few seconds. This can be calculated through Equation 6-4 (modified after Carslaw & Jaeger, 1959), which is the analytical solution of the 1D transient hydraulic equation for infinite half space (Equation 5-4).

$$P = P_0 + \operatorname{erfc} \left(\frac{x}{2 * \sqrt{\frac{K}{S_c}} * t} \right) * (P_{inj} - P_0)$$

Equation 6-4

Figure 6-3 shows the temporal pressure evolution in the fracture for $P_0 = 0$ MPa at the production point ($x = 450$ m), $P_{inj} = 2$ MPa at the injection point ($x = 0$ m), $K = 8.5 * 10^{-8}$ m²/Pas and specific storage coefficient $S_c = 10^{-10}$ Pa⁻¹. The fixed pressure distribution that is prescribed by the boundary conditions is reached already after 600 seconds. At the production well the analytically calculated pressure is higher than the pressure calculated with *FRACHEM*. This is because the analytical equation is valid for infinite half space models, whereas the numerical model is not infinite.

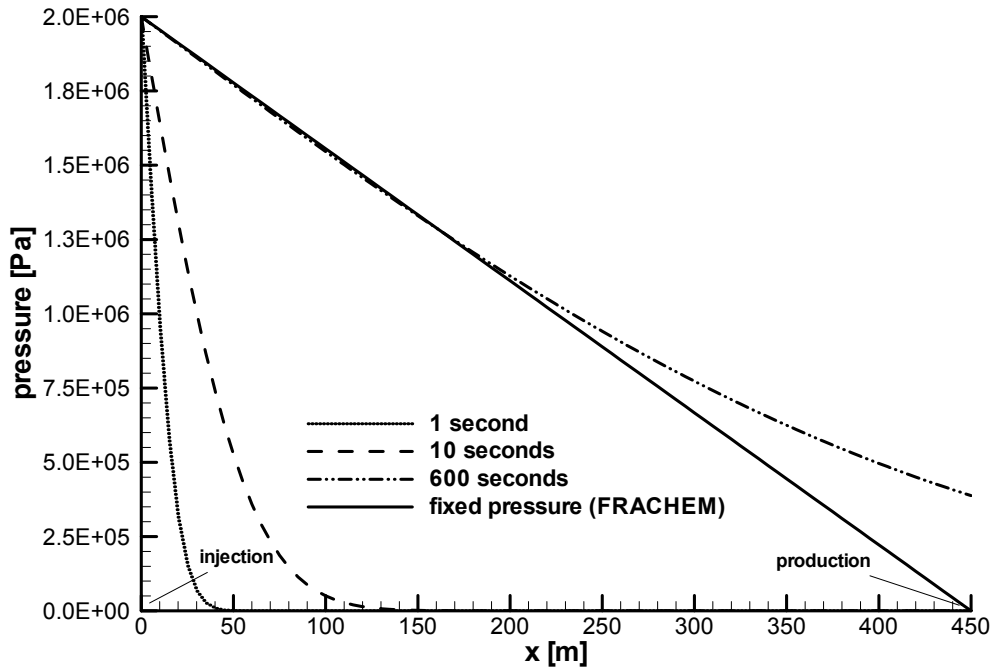


Figure 6-3: Pressure evolution in the fracture calculated after Equation 6-4.

6.2 MODEL 1: TH COUPLING

As mentioned before, the different processes were coupled step by step. In this section only thermal and hydraulic processes were coupled to investigate the model sensitivity in terms of hydraulic and thermal processes. First, the results of a basic model are presented and then those after changing the mesh discretization and time steps.

6.2.1 Basic model results

The basic model consists of a time sequences indicated in Table 6-2. The temperature and pressure distribution in the fracture and the matrix after 10 years, the end of the simulation, is shown in Figure 6-4 and Figure 6-5. The temperature was decreased from 165°C to 65°C near the injection well. Along the fracture it increases to 85°C towards the production point. Due to thermal diffusion, the temperature of the matrix is decreased around the fracture. The flow velocity develops perpendicular to the isobars and reflects the Neumann boundaries: it decreases from 2 MPa at the injection point towards the production well where it reduces to 0 MPa. The resulting fluid velocity of $3.77 \cdot 10^{-4}$ m/s compares well with the theoretically calculated velocity

resulting from multiplying the hydraulic conductivity K_k with the pressure gradient ∇P .

$$v = K_k * \nabla P$$

Equation 6-5

Using Equation 6-5 yields $v = 3.84 \cdot 10^{-4}$ m/s. The numerical calculated velocity is lower because of fluid diffusion into the matrix, which is not taken into account in the equation. Since steady-state hydraulic process was calculated, the pressure and velocity do not change during the simulation.

Table 6-2: Time sequences and time step sizes of the basic model. n is the number of the time sequence, $nstep$ the number of time steps per sequence, dt the time step size and sum of dt the total simulation time.

n	nstep	dt [sec]	sum of dt
1	1	1	-
2	1	1	-
3	1	100	100 sec
4	10	10^4	27 hours
5	10	10^5	11 days
6	10	10^6	0.3 years
7	100	10^6	3.5 years
8	100	10^6	6.7 years
9	11	10^7	10 years

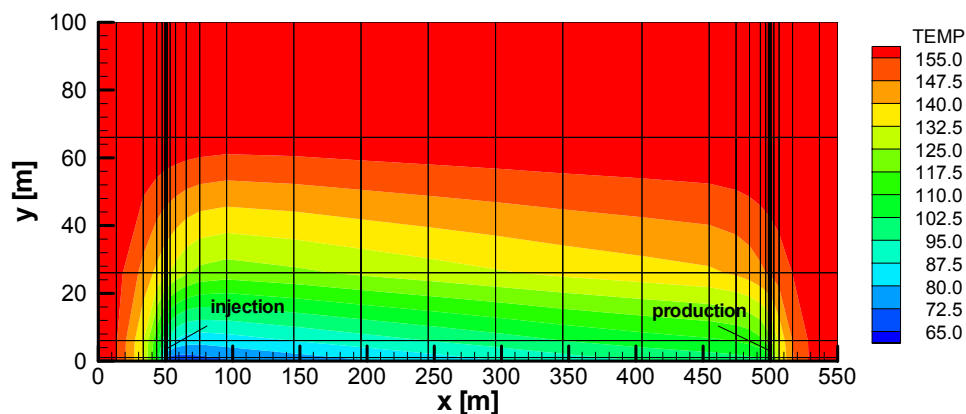


Figure 6-4: Temperature distribution in the model after 10 years. The temperature is given in $[^{\circ}\text{C}]$.

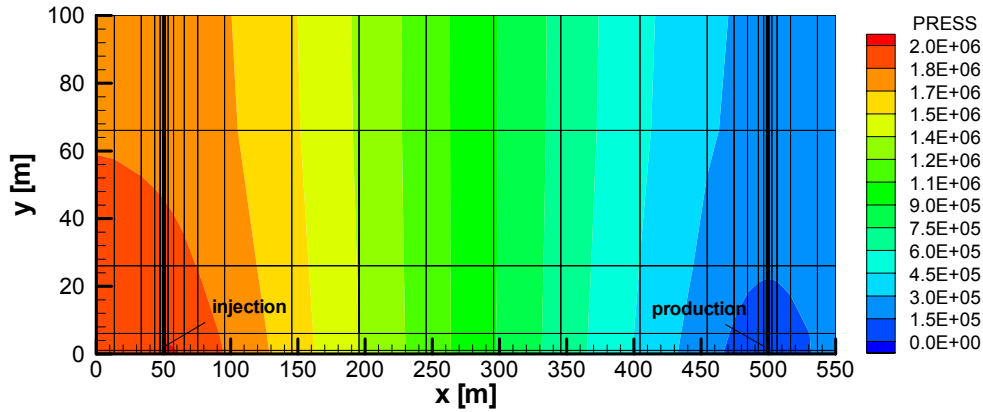


Figure 6-5: Pressure distribution in the model after 10 years. The pressure is given in [Pa].

Figure 6-6 shows the temperature development along the fracture axis ($y=2.5 \cdot 10^{-3}$ m) after different times. The temperature steadily decreases in the fracture. The diffusive temperature front has not yet reached the model boundary.

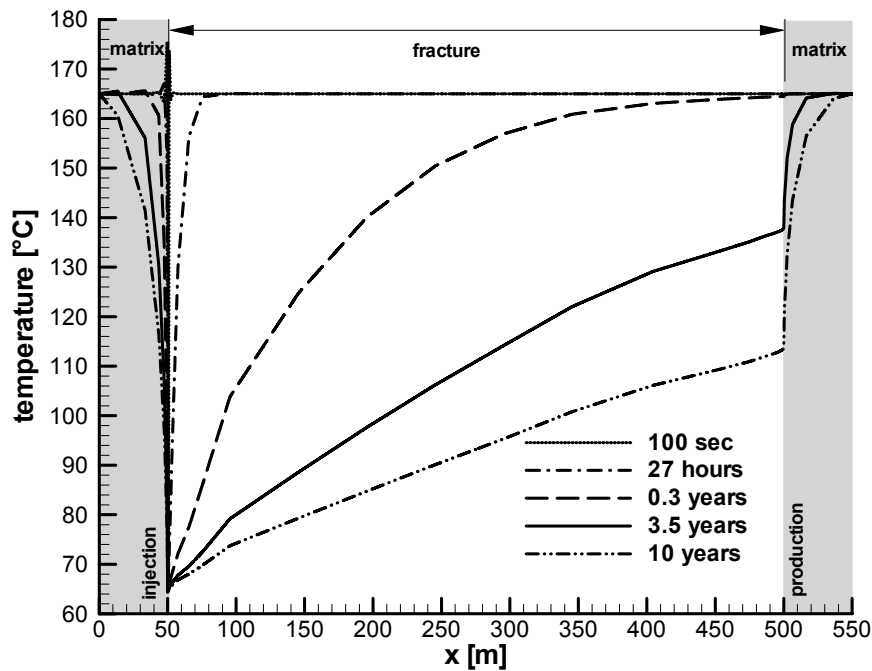


Figure 6-6: Temperature development along the fracture axis ($y=2.5 \cdot 10^{-3}$ m) after different times.

The figure shows the restrictions of the numerical model: the Galerkin discretization of the advection term raises difficulties for numerical codes (chapter 5.2.2). Calculating with small time steps at the beginning of the simulation leads to

numerical oscillations near the injection well. This can be seen at 100 seconds. In the following time steps there are no oscillations any more.

For the present model $Cr = 0.075$ ($v = 3.77 \cdot 10^{-4}$ m/s, $\Delta t = 10^2$ sec and $\Delta L = 0.5$ m) and $Pe = 264$ (Equation 5-6 and Equation 5-7). With the given model parameters, Pe is about one order of magnitude too high whereas Cr is acceptable. By reducing the discretization size ΔL , Pe can be decreased. Below, an attempt was made to reduce the oscillations by refining the mesh.

6.2.2 Geometrical- and time step sensitivity

The basic mesh was refined twice, not only to reduce the oscillations but also to investigate if the mesh discretization has an influence on the results. The refined mesh elements are one fourth of the original element length and height.

The results show that even with the refined mesh, oscillations occur near the injection well at the beginning of the simulation. With logarithmic refining of the mesh, these oscillations would certainly vanish. However, since a time scale of 100 seconds is of no importance in the simulation, they were neglected in the following. For the rest of the simulation time, the results do not differ much from the basic model: at 27 hours the largest temperature difference in the fracture is 12°C . This is less than 1% of the total temperature. At 10 years both temperatures are nearly the same. The difference is no more than 2°C . Thus, both models result in comparable temperature distributions. To investigate the sensitivity and the power of the code the basic model can be used.

Further models with different time step length were calculated to test the sensitivity to time steps. The models result in nearly identical temperature distributions and it can be stated that changing the time step does not influence the model results. In an additional model simulation, with time steps of 10^4 seconds at the beginning of the simulation, no oscillations occurred any more while the temperature distribution for later time steps stayed the same. Thus, taking time steps of at least 10^4 seconds at the beginning of the simulation suppresses the oscillations.

6.3 MODEL 2: PARTIAL THC COUPLING AT EQUILIBRIUM

In a further step, chemistry was coupled with temperature and hydraulic processes. To investigate if the initial model parameters represent chemical equilibrium the temperature of the injected fluid was kept constant at 165°C during the simulation. Also the pressure and the velocities were held constant as in the previous models. In addition, porosity changes due to dissolution or precipitation processes were not updated in the FRACTure part. The time steps were 10^2 seconds and the simulation time was one year.

As discussed in chapter 2.2.2, the target heat exchanger at Soultz is granitic rock (mainly calcite, dolomite, quartz and pyrite) and the reservoir fluids are highly saline having an amount of total dissolved solids (TDS) of about 100 g/l. Table 6-3 lists the chemical composition of the matrix and the reservoir fluid at a temperature of 165°C (Durst, 2002).

Table 6-3: Chemical model components and initial concentrations.

component	concentration [mol/kg]	component	concentration [mol/kg]
H ₂ O	$5.55 \cdot 10^{+1}$	HS ⁻	$7.20 \cdot 10^{-4}$
Na ⁺	$9.93 \cdot 10^{-1}$	CO ₃ ²⁻	$2.41 \cdot 10^{-7}$
K ⁺	$8.08 \cdot 10^{-2}$	OH ⁻	$8.07 \cdot 10^{-7}$
Ca ²⁺	$1.60 \cdot 10^{-1}$	Ca(HCO ₃) ⁺	$2.65 \cdot 10^{-4}$
H ⁺	$2.08 \cdot 10^{-5}$	HCO ₃ ⁻	$1.96 \cdot 10^{-3}$
Cl ⁻	1.46	CaCO ₃ (aq)	$2.81 \cdot 10^{-6}$
CO ₂	$3.80 \cdot 10^{-2}$	CaSO ₄ (aq)	$3.12 \cdot 10^{-4}$
SO ₄ ²⁻	$1.16 \cdot 10^{-3}$	quartz	$1.67 \cdot 10^{+2}$
H ₄ SiO ₄	$2.17 \cdot 10^{-3}$	calcite	$1.21 \cdot 10^{+1}$
Fe ²⁺	$5.01 \cdot 10^{-4}$	dolomite	1.63
Mg ²⁺	$5.43 \cdot 10^{-3}$	pyrite	$8.30 \cdot 10^{-1}$

The simulation results confirm the chosen parameter values, since most of the variables stay constant or vary only slightly. Besides temperature and pressure that were explicitly fixed also pH, porosity and permeability stay constant during all the simulation time. Only the mineral reaction rates vary slightly. Theoretically, at equilibrium, zero reaction rates would be expected. But this is rarely obtained with numerical modelling. In the present model the calcite reaction rate starts at

$-3.5 \cdot 10^{-10}$ mol/m²s and gradually decreases to $-0.5 \cdot 10^{-10}$ mol/m²s. The dolomite reaction rate changes from $-4.1 \cdot 10^{-16}$ mol/m²s to $-3.4 \cdot 10^{-16}$ mol/m²s. The quartz reaction rate decreases from $-9.7 \cdot 10^{-12}$ mol/m²s to $-9.5 \cdot 10^{-12}$ mol/m²s and the pyrite reaction rate from $-1.72 \cdot 10^{-15}$ mol/m²s to $-1.7 \cdot 10^{-15}$ mol/m²s. Since all the reaction rates are very small (compared to chapter 4.4) and tend to become zero, the system is assumed to be at equilibrium.

6.4 MODEL 3: PARTIAL THC COUPLING

6.4.1 Basic model results

The model represents the continuation of model 2. In general, the model was the same as before: the hydraulic processes were held constant and porosity changes due to dissolution or precipitation processes were not updated in the FRACTure part. This time, the temperature of the injected fluid was 65°C. Thus, the temperature was not constant any more. Since the SNIA method is very sensitive to the time step size (chapter 5.1.2), constant time steps of 10^2 seconds were taken to simulate 1 year. Such small time steps prevent the Courant number Cr from becoming larger than 1 (compare chapter 5.2.2) so that no numerical oscillations occur.

The temperature evolution is exactly the same as the one in model 1 (Figure 6-6) because permeability changes were not coupled to hydraulic processes. The porosity evolution (Figure 6-7) is as expected and described in chapter 4.4. It increases at the injection point due to dissolution of calcite and decreases towards the production point because of calcite precipitation.

The mineral reaction rates confirm the above results. Figure 6-8 and Figure 6-9 show the quartz and the calcite reaction rate, respectively, along the fracture for different time steps. Note that in *FRACHEM* negative reaction rates indicate mineral precipitation and positive dissolution.

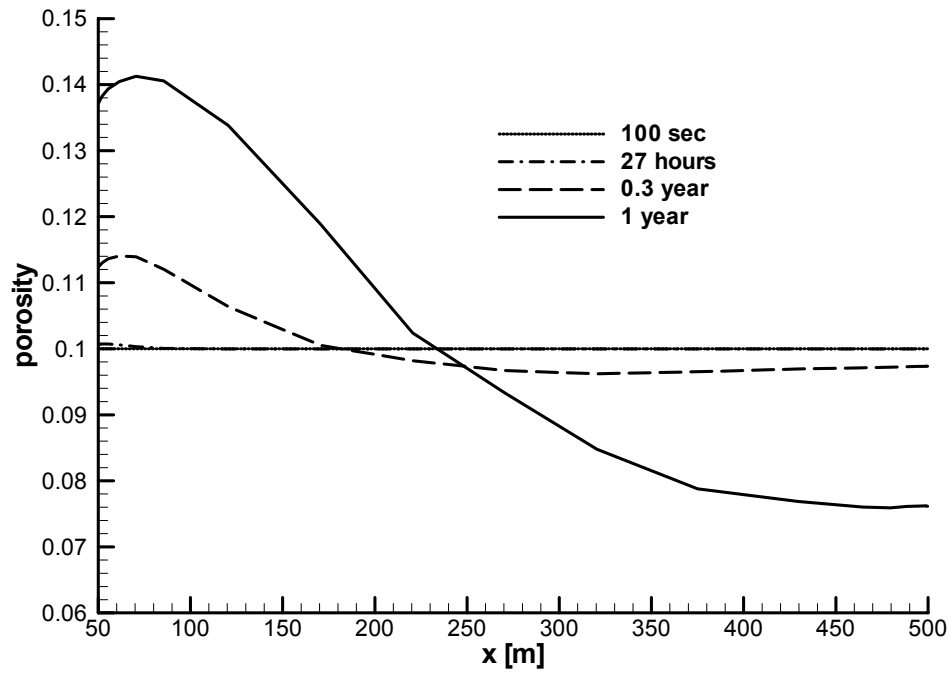


Figure 6-7: Porosity evolution within the fracture for different time steps.

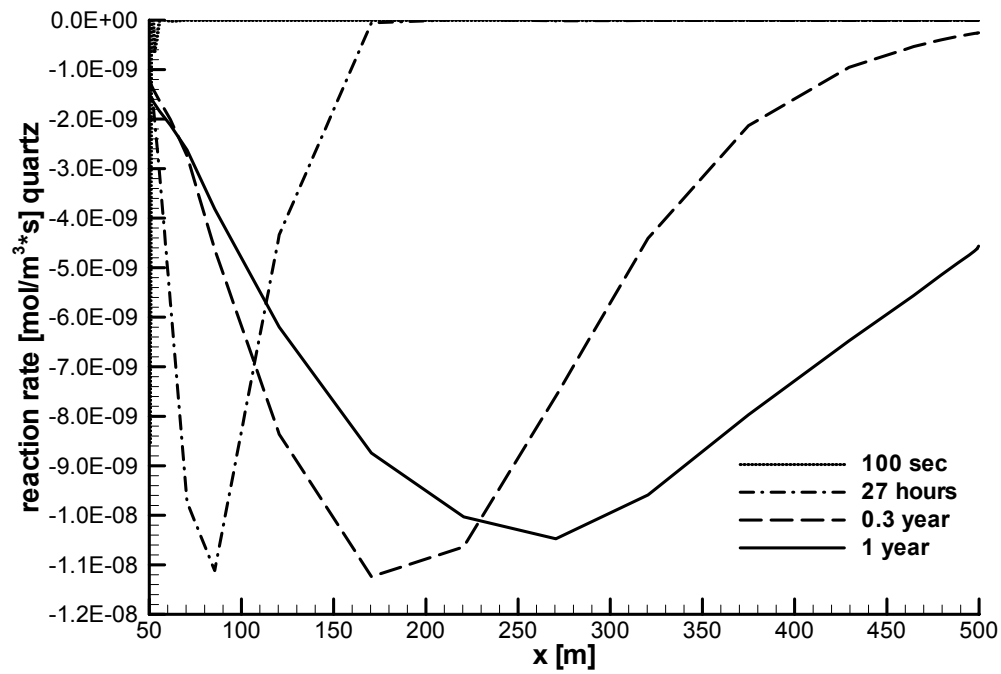


Figure 6-8: Quartz reaction rate within the fracture for different time steps.

In agreement to the predictions in chapter 4.4, quartz precipitates near the injection well due to the injection of fluid at a temperature of 65°C. With increasing simulation time the temperature (Figure 6-6) in the fracture decreases and therefore the range in the fracture where quartz is precipitated broadens and moves towards the production well. Also the calcite reaction rates evolve as predicted in chapter 4.4: near the injection point there is dissolution taking place and towards the production point calcite is precipitated. Note that the temperature oscillations that occur in the first 100 seconds of the simulation (Figure 6-6) do not affect the evolution of the reaction rates.

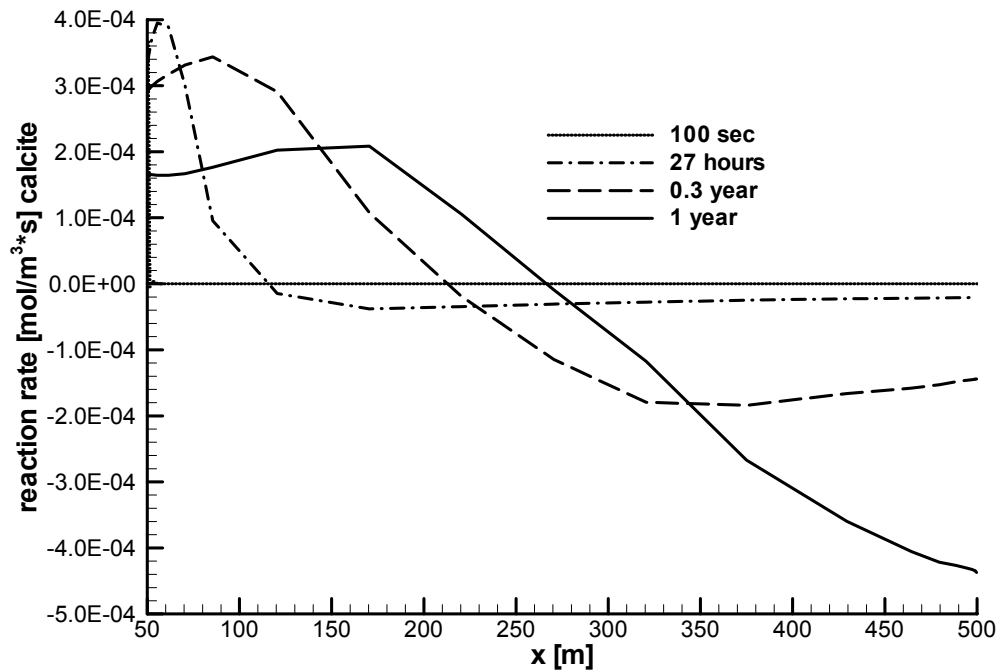


Figure 6-9: Calcite reaction rate within the fracture for different time steps.

6.4.2 Sensitivity to time steps

To highlight the importance of the time step lengths, five models are calculated for 200 days with constant time steps (10^1 , 10^2 , 10^3 , 10^4 , 10^5 seconds) during the simulation. The resulting time dependent evolution of the calcite reaction rate in the fracture at $x = 300$ m is shown in Figure 6-10: all models yield different reaction rates except the 10^1 and 10^2 seconds models. A comparison of the 10^3 , 10^4 and 10^5 seconds models highlights that the size of the reaction rate decreases about one order of magnitude when increasing the time step one order of magnitude. In addition,

the larger the time step, the earlier the reaction rate changes from negative to positive (from precipitation to dissolution, respectively).

Since the 10^1 - and the 10^2 seconds models yield the same results in contrast to all other models, it can be stated that at time steps larger than 10^2 seconds the SNIA method causes numerical oscillations (chapter 5.1.2). Oscillations may yield negative species concentrations causing the chemical solver to break down. The implemented duplicate reaction rate calculation and controls that prevent the concentrations from becoming negative (chapter 5.4.3), are not sufficient to overcome this problem. Such prevention, however, creates artificially altered reaction rates. Rates that result when calculating with time steps larger than 10^2 seconds are therefore imprecise. Model simulations without controls confirmed these findings: *FRACHEM* breaks down when calculating with time steps larger than 10^2 seconds. In addition, since the quartz reaction rate does not reveal such artificial rates, high reaction rates - such as that of calcite- are more likely to evoke oscillations.

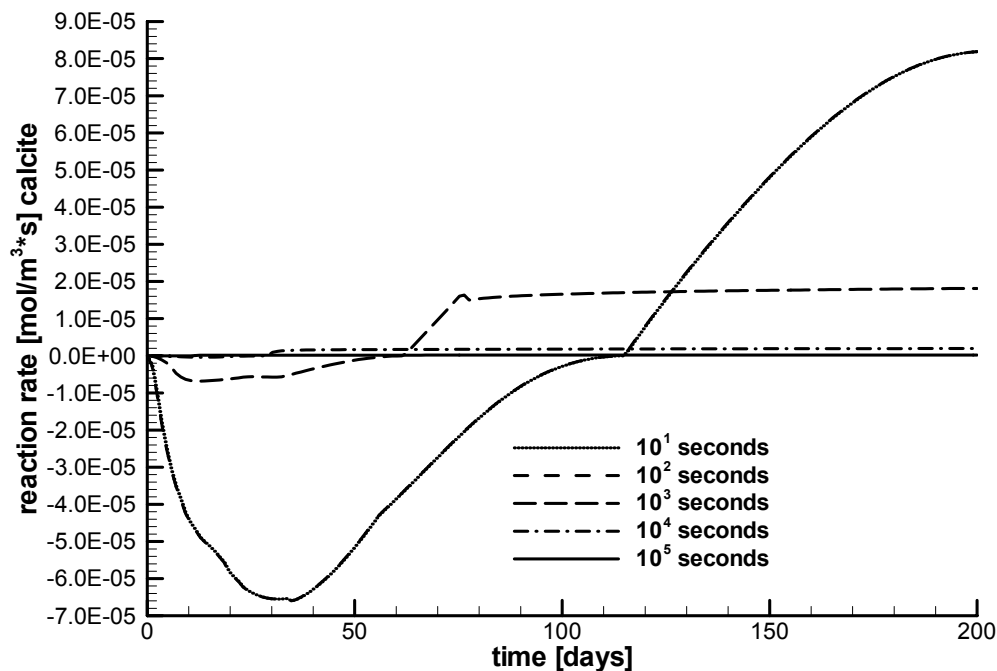


Figure 6-10: Comparison of time dependent calcite reaction rates in the fracture at $x = 300$ m for five models with different time steps.

The differences in the reaction rates result in varying porosities. Figure 6-11 shows the porosity evolution for the five models. The difference in porosity between the

10^3 - and the 10^4 seconds model is about 0.01 after one year of simulation, which is about 10% of 0.11 (the porosity after one year for the 10^4 seconds model). This difference is expected to increase further when calculating more than one year. Again, the 10^1 – and 10^2 seconds models result in identical porosities.

For the present model, 10^2 seconds is the largest time step that can be taken to obtain reasonable results. This time step size may vary with every new model set up depending on the chosen parameters and has to be found through sensitivity analyses.

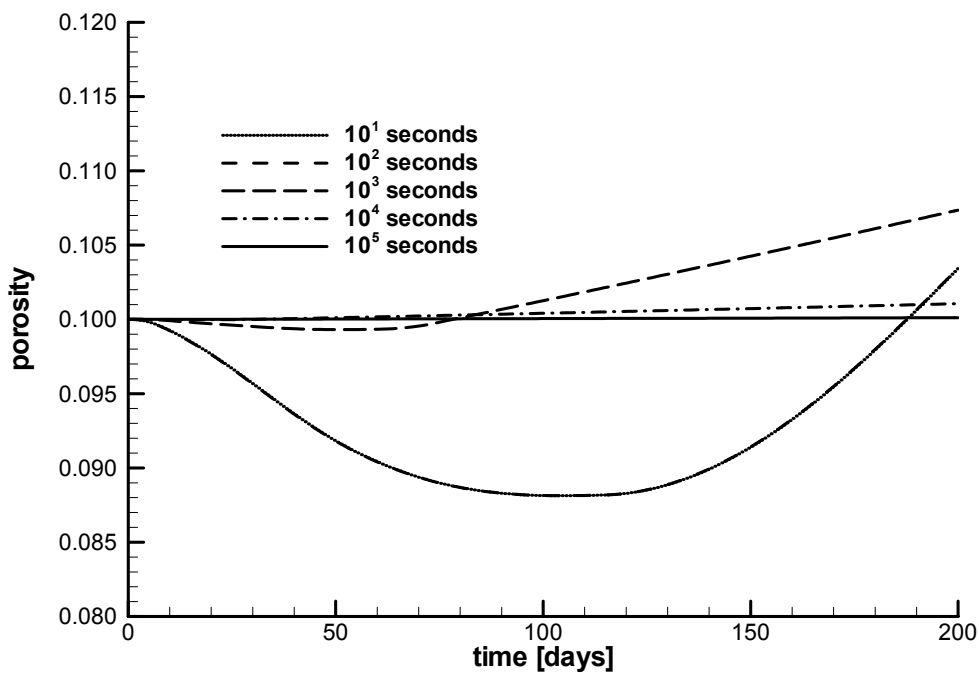


Figure 6-11: Comparison of time dependent porosities in the fracture at $x= 300$ m for five models with different time steps.

6.4.3 Refining the model

The basic model was refined to test if the mesh discretization has an impact on the chemical model results. The mesh elements are now half as long and high as before. Since refining the mesh results in only minor temperature changes (see chapter 6.2.2) and the pressure was still steady-state, possible changes in the results have to be traced back to the chemical module of *FRACHEM*.

The reaction rate curves evolve similar in both models and the difference is very small ($\Delta r_{\text{calcite}} = 1.0 \cdot 10^{-6} \text{ mol/m}^3\text{s}$ and $\Delta r_{\text{quartz}} = 4.0 \cdot 10^{-10} \text{ mol/m}^3\text{s}$). Also the porosity evolution differs only slightly (around 1%). Since all other parameter depend on the

reaction rates and the porosity, it can be assumed that all these parameters do not change much either. Thus, the mesh discretization does not influence the model results.

6.5 MODEL 4: FULL THC COUPLING

To conclude the sensitivity analyses, model 3 was simulated again but porosity changes due to dissolution or precipitation processes were now updated in the FRACTure part. Thermal, hydraulic and chemical processes were fully coupled. Note again, that here the focus is the model sensitivity and the capacity of the code. Detailed interpretations of the model results are given in chapter 8.

6.5.1 Basic model results

Figure 6-12 to Figure 6-14 show the temperature, calcite reaction rate and porosity evolution of model 4 compared to model 3. The general behaviour is the same. But changes in the porosity/permeability, and thus in the hydraulic conductivity, now impact the fluid velocity and the pressure distribution in the fracture: mineral precipitation causes the porosity and therefore also the permeability and the hydraulic conductivity to decrease. Lower hydraulic conductivity results in lower fluid velocities. Figure 6-12 shows the resulting effect on the temperature. The calcite precipitation near the production well causes the fluid velocity to decrease. Since the fluid velocities are smaller, the rate of temperature decrease in the fractured zone is lower than in model 3. After 1 year, the maximum temperature difference between the two models is 10°C (in the middle of the fracture). Figure 6-13 highlights the difference in the calcite reaction rate between model 3 and model 4. The slower temperature decrease in the fracture results in lower mineral reaction rates up to 400 m and in higher rates near the production point. After 1 year, the maximum difference in the reaction rates is $1.4 \cdot 10^{-4} \text{ mol/m}^3\text{s}$ (in the middle of the fracture). Due to the lower reaction rates up to 400 m, the porosity does not increase as fast as in model 3 (Figure 6-14), whereas near the production well the porosity decreases more slowly. The maximum porosity difference occurs in the middle of the fracture and is about 0.005.

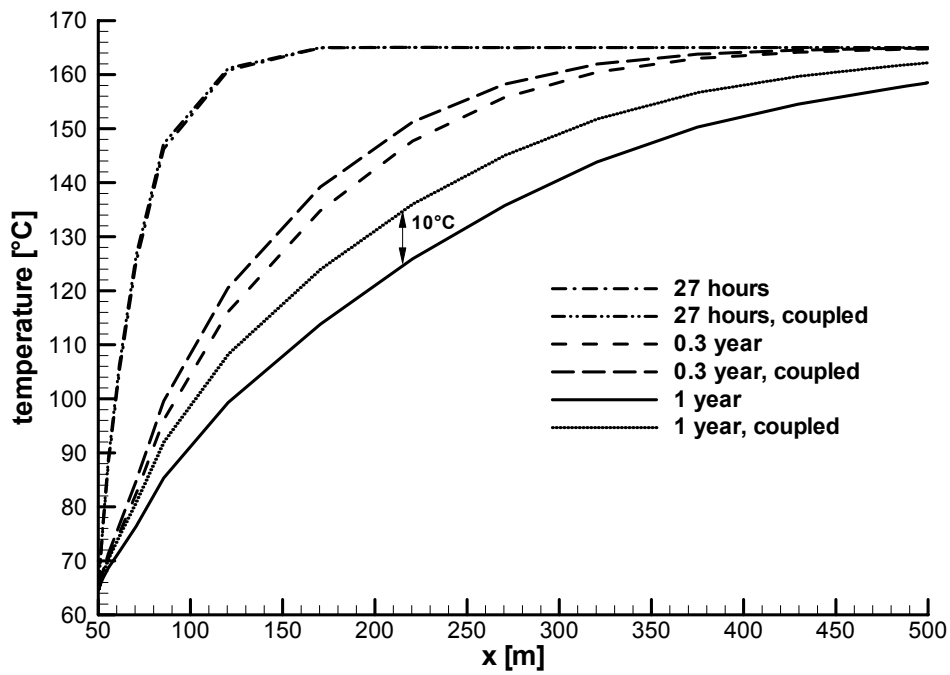


Figure 6-12: Comparison of temperature evolution along the fracture between the partially coupled model (model 3) and the fully coupled model (model 4).

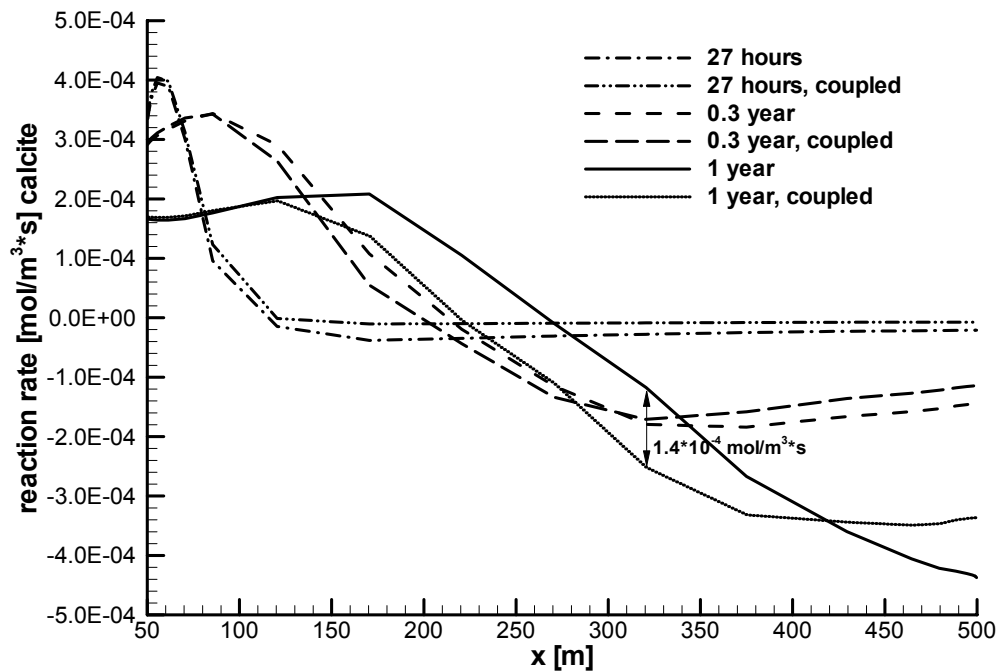


Figure 6-13: Comparison of calcite reaction rate evolution along the fracture between the partially coupled model (model 3) and the fully coupled model (model 4).

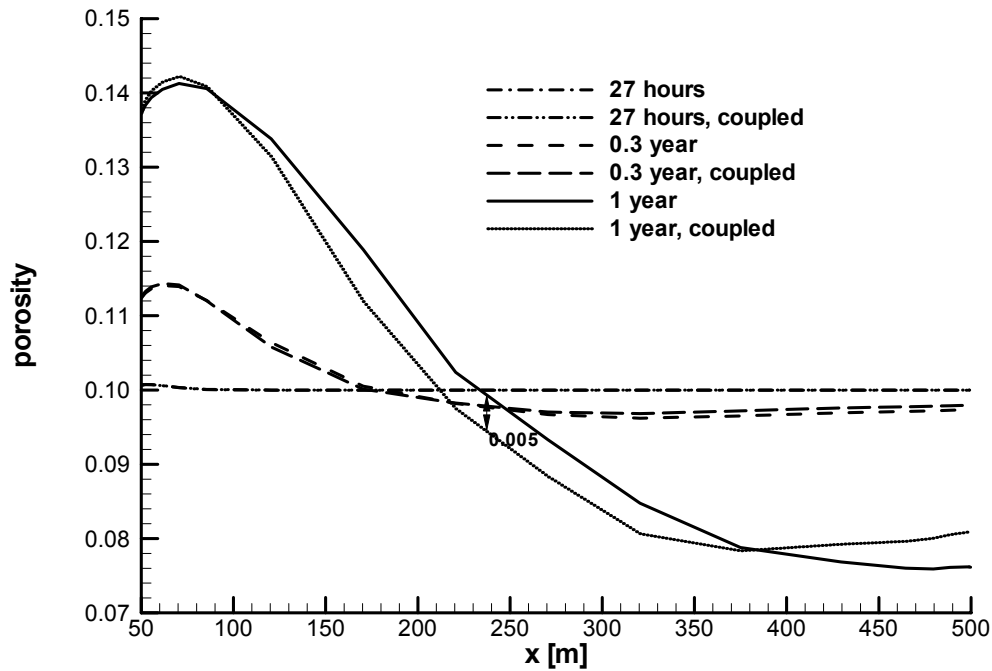


Figure 6-14: Comparison of porosity evolution along the fracture between the partially coupled model (model 3) and the fully coupled model (model 4).

The simulation results of model 4 are in agreement with the expected results when the thermal, hydraulic and chemical processes are coupled. Thus, *FRACHEM* also yields reasonable results for fully coupled models. Moreover, the comparison of the two models shows the interdependence of the different parameters and thus reveals the effect of the coupling.

6.5.2 Sensitivity to the amount of fluid flow through the fracture

When coupling the chemical module to *FRACtUre* the stability of the code was especially investigated: allowing too much fluid to be transported from one element into the neighbouring element could lead to high Courant and Péclet numbers, which would cause the code to break down due to numerical instabilities (see chapter 5.2.2). Therefore, in a first attempt, only 10% of the fluid amount in the actual element was transported from the actual element into the neighbouring element within one time step. A single transportation time step was ten times smaller but repeated ten times to transport the total fluid amount.

However, sensitivity analyses showed that *FRACHEM* is stable when calculating with time steps of 10^2 seconds, no matter what percentage of element fluid amount is

transported in one time step. Moreover, exactly the same results are produced when allowing 10%, 50% or even 100% of the element fluid amount being transported within the same time step. This shows that if the time step is chosen so that $Cr < 1$ and $Pe < 10$, there is no need to limit the amount of fluid flow. Thus, future *FRACHEM* models will allow 100% of the element fluid amount to be transported in a single time step.

6.6 CONCLUSIONS

The sensitivity analyses give detailed information on the capacity of *FRACHEM*. First of all, only thermal and hydraulic processes were coupled (model 1). This allowed verification of the model set up and the analytically calculated model parameters. In addition, the model sensitivity in terms of hydraulics and thermal processes could be investigated. The simulation results show that the temperature and the pressure field evolve as expected. The numerically calculated velocity compares well with the analytical calculations.

In model 2 thermal, hydraulic and chemical processes were partially coupled by not updating porosity changes due to dissolution or precipitation processes in the FRACTure part. The simulation at equilibrium (165°C) showed that the initial chemical parameters are well equilibrated and represent equilibrium.

In model 3 the temperature was no longer constant. These simulations revealed that the selected time step strongly influences the simulation results. Due to the time step sensitivity of the SNIA method, at time steps larger than 10^2 seconds, numerical oscillations occur. The duplicate calculation of the reaction rates and controls, which were implemented in *FRACHEM* to prevent this, turned out to be insufficient. Moreover, the controls yielded artificial reaction rates. Thus, for this model set up, the largest time step that still results in correct reaction rates is 10^2 seconds. Further mesh refinement did not change the results.

Finally, in model 4 the porosity changes were updated in the FRACTure part. Comparing with model 3 highlighted the importance of coupling thermal, hydraulic and chemical processes. Although the overall trend of the model results is the same, detailed investigations prove that the update of the porosity in the FRACTure part changes the model behaviour. Furthermore, it was shown that limiting the amount of fluid flow from element to element was not needed to prevent oscillations as long as the maximum time step size was 10^2 seconds.

The sensitivity analyses show that the *FRACHEM* model yields reliable results provided that the maximum size of the selected time steps are 10^2 seconds. However, the fact that there is an upper practical limit to the time step sizes is inconvenient. With a maximum time step size of 10^2 seconds long-term simulations take very long calculation times.

7 BENCHMARK WITH SHEMAT

This chapter summarizes the results from a comparative simulation between *FRACHEM* and *SHEMAT*. The benchmark was used to quantify the *FRACHEM* results, since no reliable measured data were available. *SHEMAT* was chosen because it is similar to *FRACHEM*, intensively tested and a laboratory experiment was successfully simulated.

7.1 GENERAL

The development of *SHEMAT* started in 1982 as a tool to simulate advective heat transport in porous media based on the USGS 3D groundwater code by Trescott & Larson (1977). *SHEMAT* was continuously developed and is today -similar to *FRACHEM*- a tool for simulating coupled flow, heat transfer, multi-component transport and chemical reactions in porous media (Clauser, 2003). It can be used for a wide variety of thermal and hydrogeological problems. *SHEMAT* is particularly well suited to quantify the effect on flow and transport of chemically induced changes in the pore space of deep sandstone aquifers. It was also successfully employed for the prediction of the long-term behaviour of hydro-geothermal hot water production systems where operation times of at least 30 years are required.

SHEMAT includes the graphical user interface *Processing SHEMAT*, which is based on *Processing MODFLOW* (Chiang & Kinzelbach, 2001). *Processing SHEMAT* includes a professional graphical pre- and postprocessor, the 3D finite difference fluid flow, the heat and species transport code *SHEMAT* and the chemical reaction module.

7.2 CHEMICAL MODULE OF SHEMAT

As in *FRACHEM*, where the chemical module is based on *CHEMTOUGH*, the chemical reaction model in *SHEMAT* is a modification of the geochemical code *PHRQPITZ* (Plummer et al., 1988). It calculates the precipitated or dissolved amount of mineral species for high temperature and salinity, using the Pitzer approach to calculate the activity coefficients. A data base of Pitzer interaction parameters, valid for temperatures from 0 to 150°C, is provided for the system Na-K-Mg-Ca-H-Cl-SO₄-OH-(HCO₃-CO₃-CO₂)-H₂O. The Pitzer treatment of the aqueous model is based on the equations presented by Harvie et al. (1984) and data of Greenberg & Möller (1989). The data for the incorporated carbonic acid system (set in parentheses in the above list) are valid for temperatures from 0 to 90°C according to He & Morse (1993). *PHRQPITZ* was extended (Kühn, 2003) to include the calculation of temperature dependent Pitzer coefficients.

To calculate the kinetic reaction laws, a general law is implemented in *SHEMAT* for all minerals.

$$\Delta C_i = \Delta t * s * r * \exp\left\{-\frac{E_{act}}{k_B * T}\right\} * \left\{\frac{C_{ion}(t) - C_{eq}(t)}{C_{eq}(t)}\right\}$$

Equation 7-1

ΔC_i is the concentration change of mineral i, s the reaction surface of a mineral, r the reaction rate, E_{act} the activation energy, k_B the Boltzmann's constant, C_{ion} the concentration of a species and C_{eq} the equilibrium concentration of a species. Variable initial reaction rates, activation energies and initial surface reaction areas are used to differentiate between the minerals.

7.3 NUMERICAL IMPLEMENTATION

The partial differential equations for flow, heat transfer and multi-component transport are solved numerically by a finite difference approach. A pure upwind scheme, the II'in-flux-blending scheme (Clauser and Kiesner, 1987) and the Smolarkiewicz method (Smolarkiewicz, 1983) are implemented for solving the advective transport equations.

The SNIA approach was used to couple flow, heat transfer, multi-component transport and geochemical reactions as in *FRACHEM* (chapter 5.4.3). The relationship between the permeability and porosity is based on the assumption that the shape of the

internal surface of rock pores follows a rule of self-similarity. The theory of fractals is applied using the formulations from Pape et al. (1999) based on the Kozeny-Carman equation. Permeability is expressed as a power series of porosity calculated from the fractal dimension of the fluid-matrix interface. The expression is very complex and numerous petrophysical data are needed to calibrate it.

The single modules of the numerical model were tested against different standard benchmarks and literature data to verify that the implemented modules work correctly and that the code yields results of sufficient quality. The coupling aspects were successfully modelled by simulating the permeability evolution observed during a core flooding laboratory experiment with an anhydrite probe (Bartels et al., 2002).

7.4 COMPARISON BETWEEN *FRACHEM* AND *SHEMAT*

The most appropriate model to compare would be the core flooding laboratory experiment with anhydrite (Bartels et al., 2002), since this model reproduces measured data. Unfortunately, *FRACHEM* does not contain anhydrite. To our knowledge, there is no other laboratory experiment with brines at high temperatures and therefore, the model of the sensitivity analyses (chapter 6) was used again.

It was intended to use identical parameters (chapter 6). Only two modifications had to be made, to run the same model with *FRACHEM* and *SHEMAT*: 1) The initial temperature in the model was changed from 165°C to 90°C, since the data for the carbonic acid system in *SHEMAT* are only valid up to a temperature of 90°C. 2) Only calcite and quartz was integrated in the model; pyrite cannot be simulated with *SHEMAT* because Fe^{2+} is not integrated in the database. Dolomite was left out, to avoid interactions between calcite and dolomite and to keep the model simple.

For an ideal comparison both, the *FRACHEM* and the *SHEMAT* model runs were gradually developed. In a first step, the temperature and the pressure field were modelled. Then, the thermodynamic equilibrium at temperatures of 65°C and 90°C was calculated. And finally, fully coupled models including kinetics were calculated.

7.4.1 Temperature and pressure field

The aim of the first model run was to receive the same temperature and pressure field in the *FRACHEM* and the *SHEMAT* model in order to have the same basis for the chemical model. *SHEMAT* calculates in groundwater hydraulic units (meters) and absolute pressure, whereas *FRACHEM* calculates the hydraulics in Pa and relative

pressure distributions (over-pressure) can be calculated. Therefore, different boundary conditions have to be set: the initial pressure in *FRACHEM* was 0 MPa and in *SHEMAT* 3500 m, representing zero over-pressure and hydrostatic pressure at 3500 m. In *FRACHEM*, Dirichlet boundary conditions are set to fix the pressure to 2 MPa and 0 MPa and in *SHEMAT* to 3700 m and 3500 m at the injection and the production well, respectively. The pressure P at the production well is calculated according to Equation 7-2 based on the absolute pressure at 3500 m depth and 2 MPa over-pressure. In the equation, ρ_f is the fluid density (1000 kg/m^3) and g (9.81 m/s^2) the gravitational constant.

$$P[m] = \frac{2 \text{ MPa}}{\rho_f * g} + 3500 \text{ m}$$

Equation 7-2

As in the previous model, 0.02 l/s fluid at $T = 65^\circ\text{C}$ is injected at the injection well and extracted at the production point. The model parameters for the matrix and the fracture are calculated according **Equation 6-1** to Equation 6-3, Equation 5-2 and Equation 5-3. The resulting values are listed in Table 7-1.

Table 7-1: Model parameter for the *FRACHEM* and the *SHEMAT* model.

parameter		fracture _k	matrix _m	fluid _f
hydraulic conductivity K	$[\text{m}^2/\text{Pas}]$	$7 \cdot 10^{-8}$	10^{-15}	-
permeability k	$[\text{m}^2]$	$2.2 \cdot 10^{-11}$	10^{-18}	-
porosity Φ	$[\%]$	10	0	-
thermal conductivity λ	$[\text{W/mK}]$	2.8	3	0.6
density ρ	$[\text{kg/m}^3]$	-	2650	1000
heat capacity c_p	$[\text{J/kgK}]$	-	1000	4200
ρc_p	$[\text{J/Km}^3]$	$2.8 \cdot 10^6$	$2.65 \cdot 10^6$	$4.2 \cdot 10^6$
transmissivity Tr	$[\text{m}^3/\text{Pas}]$	$1.12 \cdot 10^{-12}$	-	-

Both models were run over a simulation period of six months. Figure 7-1 illustrates the temperature development at three different points in the fracture. The first point is at $x = 60 \text{ m}$, near the injection well, the second point is at $x = 320 \text{ m}$ in the middle of the fracture halfway towards the production point and the third point is at $x = 480 \text{ m}$, near the production well. In the following, the points are referred to as ‘near injection’, ‘middle’ and ‘near production’. Both models result in about the same

temperatures. The maximum temperature difference of $\sim 2^{\circ}\text{C}$ is near the injection at the beginning of the simulation. A good fit is obtained at the other two points. At the end of the simulation, the maximum temperature difference is 0.5°C . Such small temperature differences do not have a significant effect on the chemical behaviour of the system.

The pressure distribution cannot directly be compared, since the units are different. Chemical reactions are pressure independent in both *FRACHEM* and *SHEMAT*. Therefore, only the fluid velocities in the fracture subject to the pressure field have to be in the same range. In *FRACHEM* the fluid velocities are $3.1 \cdot 10^{-4} \text{ m/s}$ and in *SHEMAT* $3.4 \cdot 10^{-4} \text{ m/s}$. Thus, it can be stated that both models result in concordant temperature and velocities.

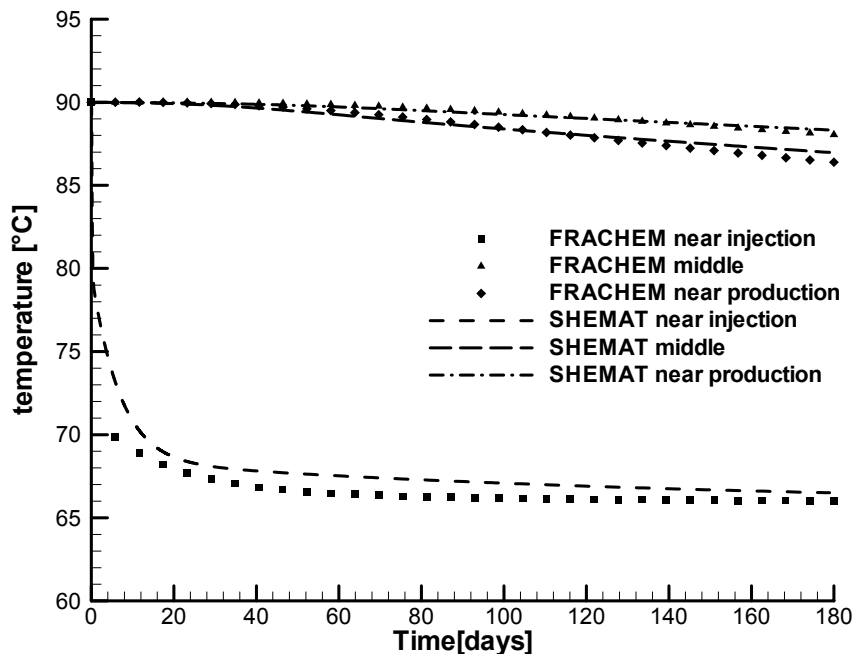


Figure 7-1: Temperature development near the injection well, in the middle of the fracture and near the production well in the *FRACHEM* and the *SHEMAT* model.

7.4.2 Equilibrium calculations

The initial model temperature of 90°C required re-equilibration of species and mineral concentrations, since the input concentrations for the previous model (Table 6-3) was equilibrated for a temperature of 165°C . This was achieved using the thermodynamic equilibrium module of *FRACHEM* (see Appendix A: chem.dat). To save computational time, the model consisted of only one element. The temperature was 90°C and no

fluid flow took place. The initial concentrations were taken from Table 6-3. Dolomite and pyrite were not included in the model.

To compare the thermodynamic modules of *FRACHEM* and *SHEMAT* and to check if the integrated Pitzer approach yields the same results, equilibrium concentrations were calculated for a temperature of 90°C with *SHEMAT*. Table 7-2 lists all concentrations. In contrast to *FRACHEM*, *SHEMAT* calculates the species concentrations by neutralizing the charge balance of the fluid, leading to slightly higher Na^+ concentrations. Since Na^+ is not a component of calcite or quartz and does not actively take part in the reactions, this difference has no impact. All other concentrations are in good agreement. Additional comparative equilibrium simulations prove that also at $T = 65^\circ\text{C}$ the results for *FRACHEM* and *SHEMAT* are similar (Table 7-2).

A comparison of the equilibrium concentrations at $T = 90^\circ\text{C}$ and at $T = 65^\circ\text{C}$ shows that calcite dissolves and quartz precipitates with decreasing temperature. Therefore, the Ca^{2+} and the C concentrations rise and the Si decrease. However, as stated in chapter 4.2, the true amount of dissolution and precipitation can only be determined when taking chemical kinetics into account.

Table 7-2: Equilibrium concentrations for *FRACHEM* and *SHEMAT* at $T = 90^\circ\text{C}$ and $T = 65^\circ\text{C}$.

	90°C	90°C	65°C	65°C
	FRACHEM	SHEMAT	FRACHEM	SHEMAT
species	[mol/kg]	[mol/kg]	[mol/kg]	[mol/kg]
Ca	$1.6361 \cdot 10^{-1}$	$1.6283 \cdot 10^{-1}$	$1.6547 \cdot 10^{-1}$	$1.6350 \cdot 10^{-1}$
Mg	$5.4274 \cdot 10^{-3}$	$5.4206 \cdot 10^{-3}$	$5.4274 \cdot 10^{-3}$	$5.4205 \cdot 10^{-3}$
Na	$9.9300 \cdot 10^{-1}$	1.0534	$9.9300 \cdot 10^{-1}$	1.0536
K	$8.0800 \cdot 10^{-2}$	$8.0746 \cdot 10^{-2}$	$8.0800 \cdot 10^{-2}$	$8.0757 \cdot 10^{-2}$
Si	$5.5910 \cdot 10^{-4}$	$3.6654 \cdot 10^{-4}$	$3.0643 \cdot 10^{-4}$	$1.9813 \cdot 10^{-4}$
Cl	1.4600	1.4590	1.4600	1.4592
C	$4.3740 \cdot 10^{-2}$	$4.3039 \cdot 10^{-2}$	$4.5602 \cdot 10^{-2}$	$4.3680 \cdot 10^{-2}$
S	$2.1904 \cdot 10^{-3}$	$2.1853 \cdot 10^{-3}$	$2.1904 \cdot 10^{-3}$	$2.1857 \cdot 10^{-3}$
calcite	12.0964	12.0729	12.0946	12.0673
quartz	167.0016	167.0467	167.0018	167.0561
pH	5.0	5.2	5.13	5.28

7.4.3 Kinetics

With the calculated equilibrium concentrations at $T=90^{\circ}\text{C}$ as initial parameters, chemical kinetic models were calculated for six months simulation time. According to chapter 7.2, additional parameters had to be set in *SHEMAT*: based on the resulting reaction rates from the *FRACHEM* simulation, the initial reaction rates were set for calcite ($10^{-4} \text{ mol/m}^3\text{s}$) and quartz ($10^{-11} \text{ mol/m}^3\text{s}$). The activation energy for calcite was assumed to be $4 \cdot 10^{-21} \text{ J}$ (Sjoeberg & Rickard, 1984) and for quartz $2.5 \cdot 10^{-18} \text{ J}$ (Rimstidt & Barnes, 1980). The initial reactive surface of minerals was set to 1 m^2 per total mineral volume present in each element. Like this, the reaction rate is internally updated due to changes of the reactive surface. The Kozeny-Carman porosity-permeability model was used with the fractal coefficients 1, 2 and 10 for the porosity ranges 0-1%, 1-10% and 10-100%, respectively. To calculate the calcite reaction kinetics, the charge balance has to be equalized via pH based on Na^+ and Cl^- . Sensitivity analyses with *SHEMAT* showed that refining the mesh does not influence the results. Other analyses highlighted that in *SHEMAT* the time step is also of great importance. As in the *FRACHEM* model, the time step had to be set to 10^2 seconds to prevent the Courant number from becoming larger than 1 (chapter 6.4.1) so that no instabilities occur.

The resulting temperatures and velocities are not much different from the thermo-hydraulic model results. The maximum temperature decrease in both models is 1°C and the velocity decrease is $3 \cdot 10^{-5} \text{ m/s}$. This already indicates that little calcite and quartz is dissolved or precipitated, respectively, causing minor changes in the porosity and permeability. Indeed, Figure 7-2 shows only small changes in the calcite- and no change in the quartz concentration. The figure compares *FRACHEM* with *SHEMAT* results. There is no difference in the quartz behaviour. It neither dissolves nor precipitates in both models. Calcite is more reactive in the *FRACHEM* model than in *SHEMAT*. The maximum difference occurs near the injection well with 8 % more dissolved calcite after six months. In the middle of the fracture and near the production well, the calcite difference is smaller. The trend is the same in both models: at the injection point calcite is dissolved and towards the production well calcite is precipitated.

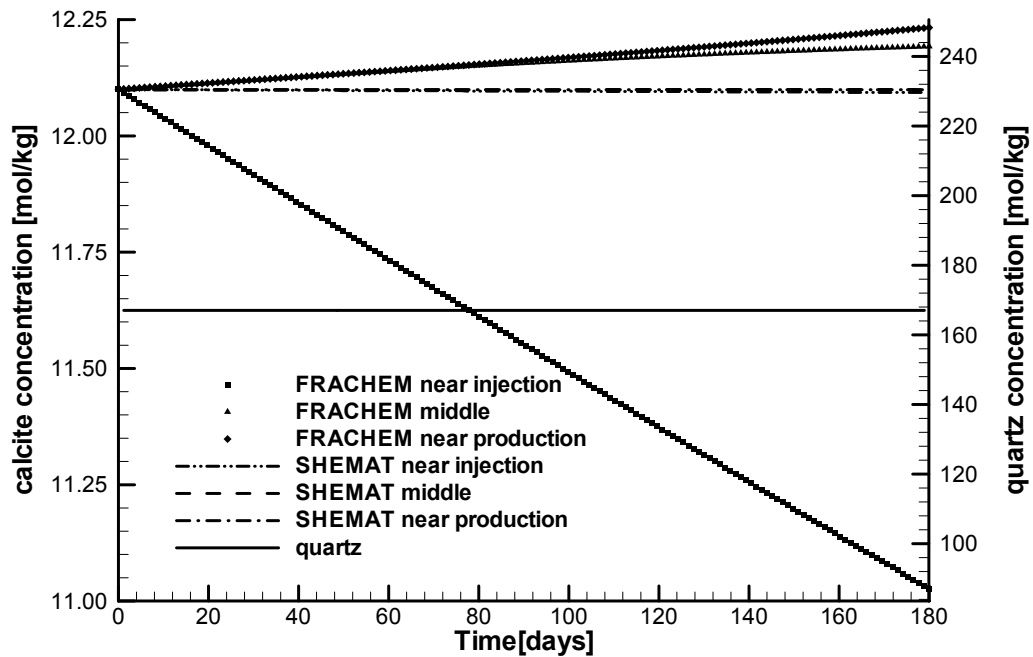


Figure 7-2: Calcite- and quartz concentration development near the injection well, in the middle of the fracture and near the production well in the *FRACHEM* and the *SHEMAT* model (with a calcite reaction rate of 10^{-4} mol/m³s).

Since both models yield similar equilibrium concentrations at $T = 90$ and $T = 65^\circ\text{C}$, the diverging amount of dissolved and precipitated calcite has to be traced back to different chemical kinetic calculations in *FRACHEM* and *SHEMAT*. Several factors can be thought of: 1) the kinetic laws for the mineral reactions, 2) the size of the assumed activation energy, 3) the reaction surface area and 4) the size of the initial reaction rate.

The kinetic reaction laws implemented in *FRACHEM* were specifically developed for each mineral (chapter 4.4). In *SHEMAT* a general law was taken for all minerals using varying initial reaction rates, activation energies and initial surface reaction areas to differentiate between the minerals (chapter 7.2). Sensitivity analyses with *SHEMAT* showed that varying the activity energy and the initial surface reaction area did not influence the results much.

However, varying the initial calcite reaction rate does change the results. Increasing the initial reaction rate two orders of magnitude to 10^{-2} mol/m³s results in the best fit; the concentrations are in the same range as the concentrations in the *FRACHEM* model. Figure 7-3 illustrates the results. The maximum concentration differences are

again near the injection well. There, the differences are about 0.15 mol/kg ($\sim 1\%$ of the initial concentration). The differences in the middle of the fracture and near the production well are much smaller and are about 0.05 mol/kg ($\sim 0.5\%$ of the initial concentration).

Unfortunately, *SHEMAT* does not allow controlling the actual reaction rates but calculates directly the resulting amount of mineral dissolution or precipitation. No comparison between the calculated reaction rates of *FRACHEM* and *SHEMAT* is possible. But, since all other parameters are the same and the resulting concentrations compare well with the *FRACHEM* model, it can be assumed that using an initial calcite reaction rate of 10^{-2} mol/m³s results in actual reaction rates of 10^{-4} mol/m³s, similar to *FRACHEM*. Future *SHEMAT* versions should print out the actual reaction rates, in order to be able to compare with the reaction rates of *FRACHEM*.

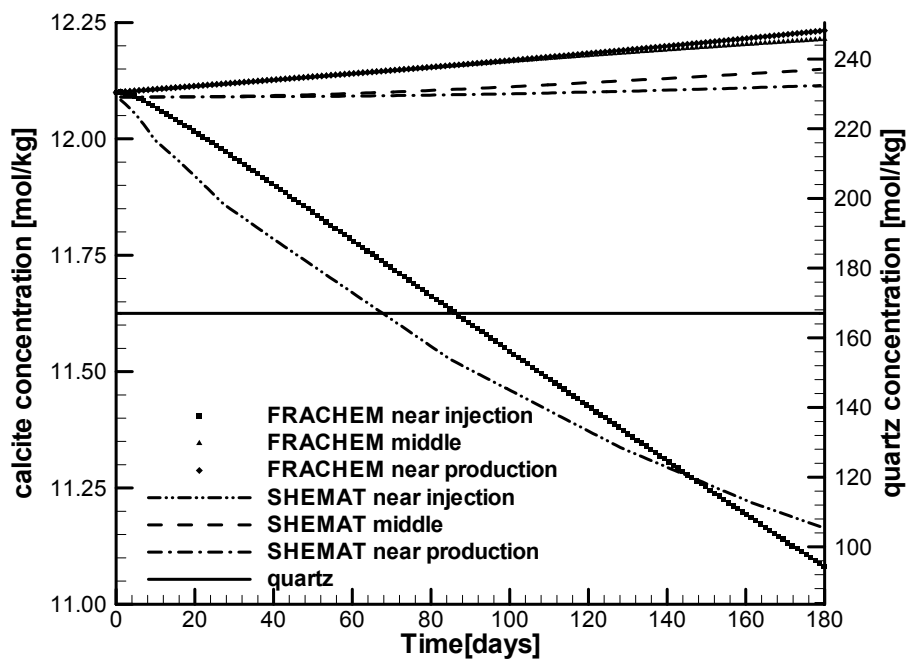


Figure 7-3: Calcite- and quartz concentration development near the injection well, in the middle of the fracture and near the production well in the *FRACHEM* and the *SHEMAT* model (with a calcite reaction rate of 10^{-2} mol/m³s).

The porosity-permeability models implemented in *FRACHEM* (model for fractured rocks, chapter 5.3.2) and *SHEMAT* (Kozeny-Carman model, chapter 7.3) result different porosities. Figure 7-4 illustrates the porosity development for the two

models. Due to the dissolution of calcite, the porosity is increased near the injection well, whereas in the middle of the fracture and near the production well they are decreased, since calcite is precipitated. The 1 % excess of calcite that is dissolved in *FRACHEM* near the injection results in 3.5 % (compared to the initial porosity) increased porosity compared to *SHEMAT* results. The 0.5 % of calcite that is precipitated more in the *FRACHEM* model leads to 0.5 % decreased porosity. Different models with varying fractal exponents were tested without achieving major changes in the results.

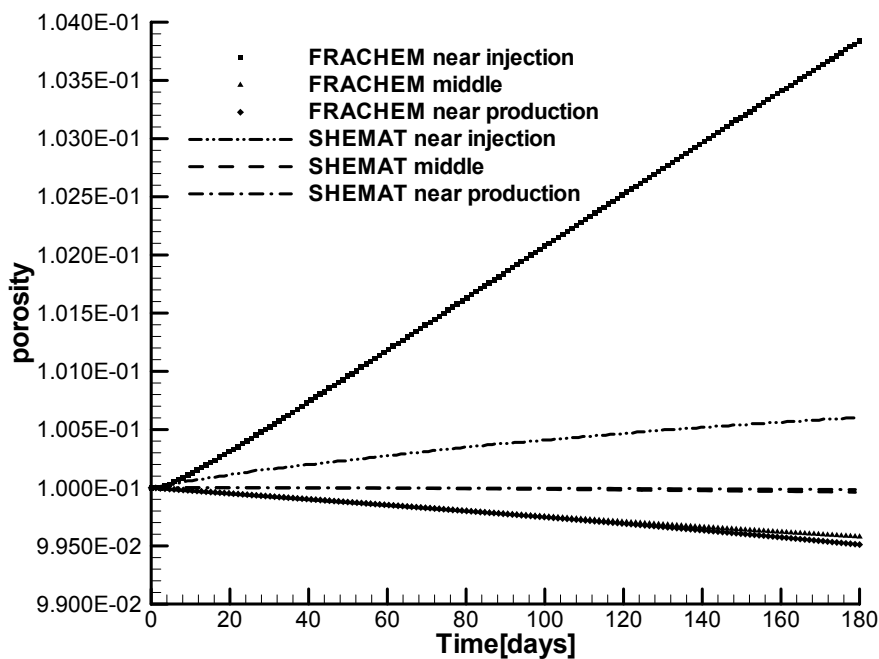


Figure 7-4: Porosity development near the injection well, in the middle of the fracture and near the production well in the *FRACHEM* and the *SHEMAT* model (with a calcite reaction rate of $10^{-2} \text{ mol/m}^3 \text{ s}$).

7.5 CONCLUSIONS

The comparative modelling validated *FRACHEM*. The fact that both models yield sensible results is of great importance, since no reliable measured data nor adequate laboratory experiments are available for comparison.

FRACHEM and *SHEMAT* calculate the same temperature development and fluid velocities. Thermodynamic equilibrium modelling at $T = 65^\circ\text{C}$ and $T = 90^\circ\text{C}$ resulted in comparable species and mineral concentrations for both models. Thus, the Pitzer approach is well implemented. Assuming an adequate initial calcite reaction rate in

the *SHEMAT* model results in a good fit of calcite concentrations. The only major difference between the two codes is the implemented porosity-permeability models resulting different porosity and permeability values.

Summarizing, it can be stated that *FRACHEM* is more suited to simulate the long term behaviour of the fractured HDR reservoir because of several factors:

- The chemical thermodynamics are limited to $T = 150^{\circ}\text{C}$ ($T = 90^{\circ}\text{C}$ for carbonate minerals) in *SHEMAT*. In *FRACHEM* these can be calculated at least to $T = 200^{\circ}\text{C}$, which is the reservoir temperature at 5000 m depth.
- The kinetic laws in *FRACHEM* are especially developed for the Soultz conditions, whereas in *SHEMAT* one general kinetic law for all minerals is implemented.
- The Kozeny-Carman porosity-permeability model that is implemented in *SHEMAT* is suited to model porous media. In Soultz however, the target host rock is highly fractured granite and therefore, the porosity-permeability model implemented in *FRACHEM* that was developed to simulate fractured media is more suited.
- *FRACHEM* is a finite element and *SHEMAT* is a finite difference code, which requires rectangular meshes. *FRACHEM* also allows irregular elements. This can be an advantage when calculating with models containing many elements. Irregular elements can then be used to reduce the number of elements and therefore, also the calculation time.

Thus, in the following chapter *FRACHEM* is used to simulate the long-term behaviour of the Soultz HDR reservoir.

8 LONG-TERM RESERVOIR MODEL

In the two previous chapters (chapter 6 and 7), the numerical behaviour of *FRACHEM* and the model sensitivity were investigated and a benchmark with *SHEMAT* was conducted. Up to this point, the model results were only qualitatively interpreted. This chapter focuses on the quantitative interpretation of the long-term HDR reservoir model results.

8.1 NUMERICAL MODEL

The geometry of the model in chapter 6 was used again (see Figure 6-2). All initial- and boundary conditions were the same as in chapter 6, except the pressure boundary conditions. For the sake of completeness, all initial- and boundary conditions are described again: the initial temperature was set to 165°C (reservoir temperature at 3500 m depth) and Dirichet boundary conditions were applied to the upper, left and right boundary. At the injection point, fluid was injected at $q_{inj} = 2 \cdot 10^{-2} \text{ l/s} = 2 \cdot 10^{-5} \text{ m}^3/\text{s}$ and a temperature of $T_{inj} = 65^\circ\text{C}$. The fluid that was produced at the production well was re-injected. This time, constant over-pressure of 6 MPa was assumed at the injection well according to the 1997 circulation test (chapter 2.1.1) and hydrostatic conditions at the production well.

The model parameters were the same as in chapter 6 (see Table 6-1). Only the hydraulic conductivity was changed, due to the modified pressure conditions. Using Equation 6-1 to Equation 6-3 leads to $K = 4.2 \cdot 10^{-8} \text{ m}^2/\text{Pas}$. Also, the initial chemical composition of the matrix and the fluid at $T_0 = 165^\circ\text{C}$ stayed the same as in chapter 6 (see Table 6-3). The injected fluid was of the same chemical composition as the produced fluid. Note that the injected fluid was not equilibrated with respect to $T_{inj} = 65^\circ\text{C}$. The simulation time was 2 years.

8.2 TEMPERATURE EVOLUTION

The fluid temperature evolution along the axis of the fractured zone is illustrated in Figure 8-1. The injection of fluid at $T_{inj} = 65^\circ\text{C}$ leads to a temperature decrease around the injection point. On its way through the fractured zone towards the production point the fluid is reheated by the surrounding granitic rock matrix up to a maximum of $T_0 = 165^\circ\text{C}$ at the production point. With increasing simulation time, the temperature in the fractured zone decreases. After 2 years, a temperature of 155°C is reached at the production well.

The temperature distribution in the matrix around the fractured zone is shown in Figure 8-2. Note that only a third of the model extension in the x-direction is illustrated. Although no fluid was assumed to circulate in the matrix, the temperature of the matrix around the fracture decreased, due to thermal diffusion. Around the injection point, the thermal diffusion front has travelled furthest into the matrix. The front has not yet reached the model boundary.

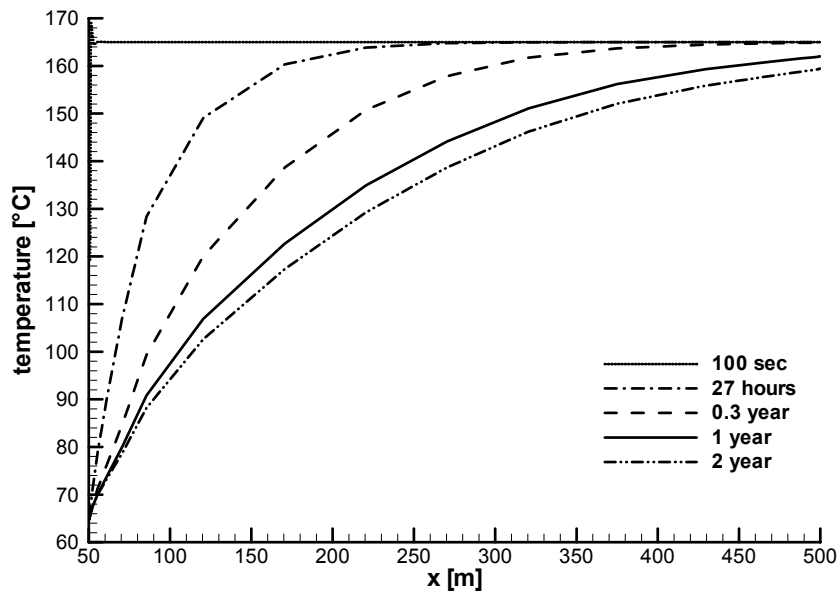


Figure 8-1: Temperature evolution in the fracture.

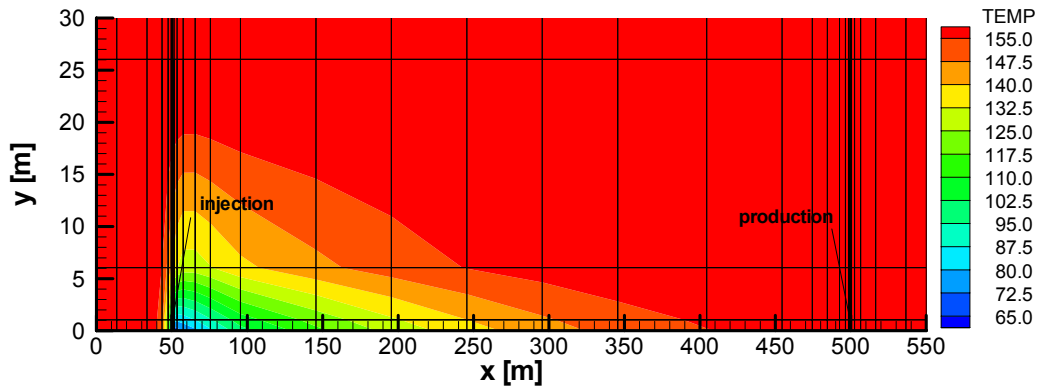


Figure 8-2: Temperature distribution in the model after 2 years. The temperature is given in $^{\circ}\text{C}$.

8.3 CHEMICAL PROCESSES

The reservoir fluid is assumed to be in equilibrium with the surrounding rock matrix at $T_0 = 165^{\circ}\text{C}$ (chapter 4.3.2). Injecting fluid at $T_{\text{inj}} = 65^{\circ}\text{C}$ causes the fluid to become disequilibrated leading to either the dissolution or precipitation of minerals. The mineral behaviour is best illustrated by the reaction rate. Therefore, the reaction rates of the different minerals are shown below instead of the concentrations. The resulting total amount of dissolved or precipitated minerals is discussed later in chapter 8.3.4. Note again that negative reaction rates represent mineral precipitation and positive rates dissolution.

8.3.1 Carbonate dissolution and precipitation

Figure 8-3 shows the calcite reaction rate. Injecting fluid at $T_{\text{inj}} = 65^{\circ}\text{C}$ causes the fluid in the fracture to be undersaturated in calcite and therefore, calcite dissolves. At the beginning of the simulation, calcite dissolution occurs at the injection point at a rate of $4 \cdot 10^{-4} \text{ mol/m}^3\text{s}$ (not shown in the figure). With increasing simulation time, the dissolution zone moves towards the production point. The maximum dissolution rate of $5.4 \cdot 10^{-4} \text{ mol/m}^3\text{s}$ is reached at 27 hours and decreases afterwards. Due to the dissolution of calcite near the injection well the fluid is enriched in Ca^{2+} . Thus, calcite starts to precipitate with increasing temperature towards the production point. The maximum precipitation rate is reached after 1 year ($6.8 \cdot 10^{-4} \text{ mol/m}^3\text{s}$). From this time onwards, the precipitation rate decreases towards zero, which is the rate at thermodynamic equilibrium.

Figure 8-4 illustrates the dolomite reaction rate. Its behaviour is similar to the calcite rate: at the beginning of the simulation dolomite dissolves at $r = 10^{-5} \text{ mol/m}^3\text{s}$ (not shown in figure) at the injection point due to the injection of fluid at $T_{\text{inj}} = 65^\circ\text{C}$. With increasing simulation time, the dissolution zone moves towards the production point. The maximum dissolution rate of $1.85 \cdot 10^{-5} \text{ mol/m}^3\text{s}$ is reached at 0.3 years and decreases afterwards. According to the predictions of the theoretical kinetic model (chapter 4.4) and the results of Durst (2002) described in chapter 5.5.2, dolomite never precipitates. This is because the calcite precipitation rate is higher than that of dolomite. Therefore, the calcite precipitation consumes all the Ca^{2+} and the CO_2 before dolomite is precipitated.

Figure 8-5 shows the evolution of the pH value that is influenced by the temperature and the carbonate reactions (chapter 4.4). The injection of fluid at $T_{\text{inj}} = 65^\circ\text{C}$ causes the pH value to decrease (Durst, 2002), whereas the carbonate dissolution consumes H^+ ions leading to an increased pH value (compare Equation 4-26 and Equation 4-27). Since the pH value is lower than the initial one (4.8), the effect of the temperature dominates. This also applies towards the production point: the release of H^+ due to calcite precipitation has a smaller effect on the pH value than the temperature and thus, the pH value (~ 4.9) is higher than the initial value.

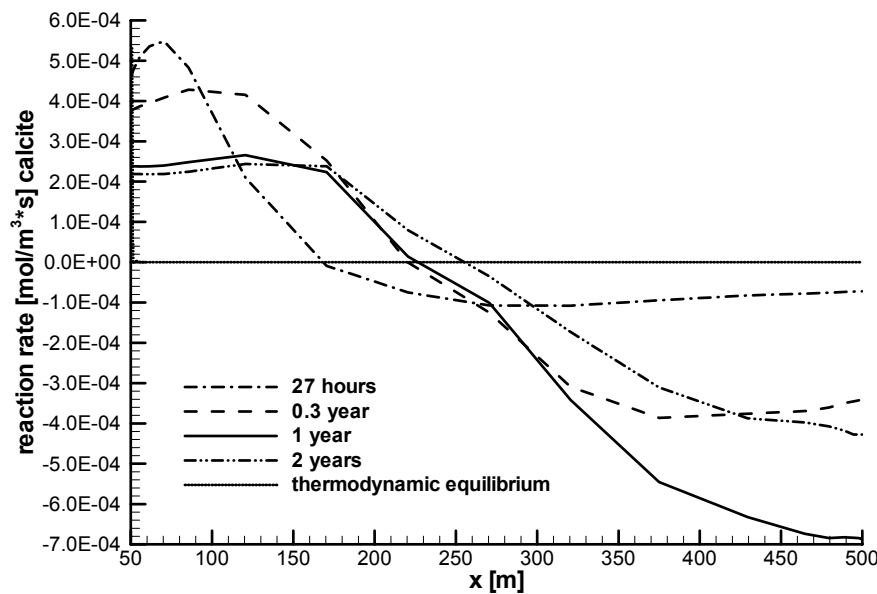


Figure 8-3: Temporal evolution of the calcite reaction rate in the fracture.

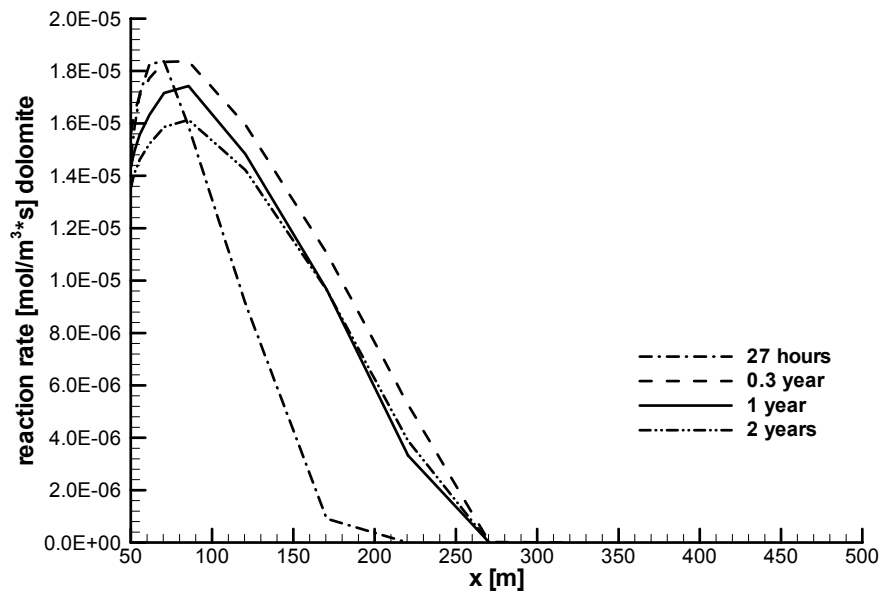


Figure 8-4: Temporal evolution of the dolomite reaction rate in the fracture.

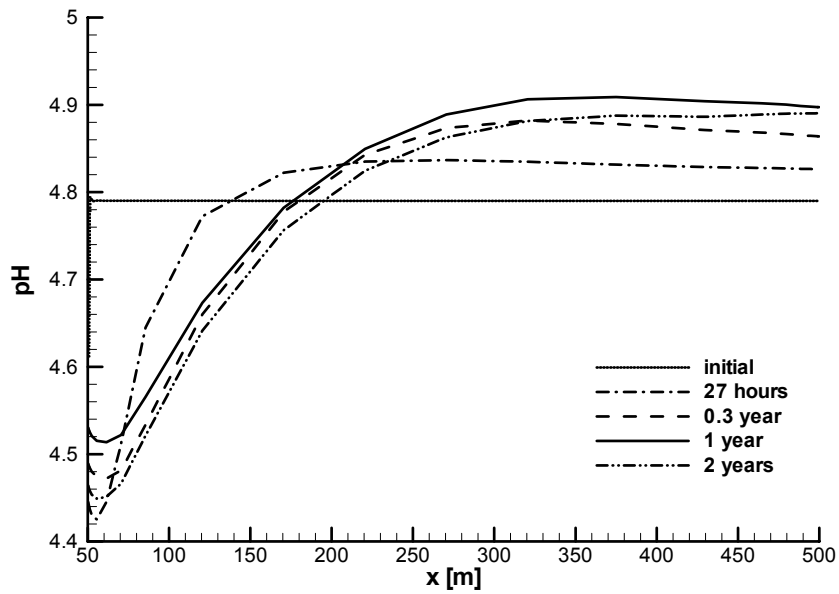


Figure 8-5: Temporal evolution of the pH value in the fracture.

The results are in good agreement with the estimated behaviour of the carbonates from the theoretical kinetic model of the Soultz system (chapter 4.4.1 and 4.4.2) and the results from Durst (2002) (chapter 5.5.3).

8.3.2 Quartz precipitation

Quartz precipitates near the injection well due to the injection of cold fluid. With increasing simulation time, the temperature in the fracture decreases (Figure 8-1) and therefore the range in the fracture where quartz is precipitated broadens and moves towards the production well. The maximum precipitation rate is $1.6 \cdot 10^{-8} \text{ mol/m}^3\text{s}$, which is one order of magnitude lower than the reaction rates found by Durst (2002). Since there are a lot of differences between the present numerical model and the model by Durst (2002) such as the model geometry, the hydraulic conductivity and pressure boundary conditions it is difficult to determine the exact reason.

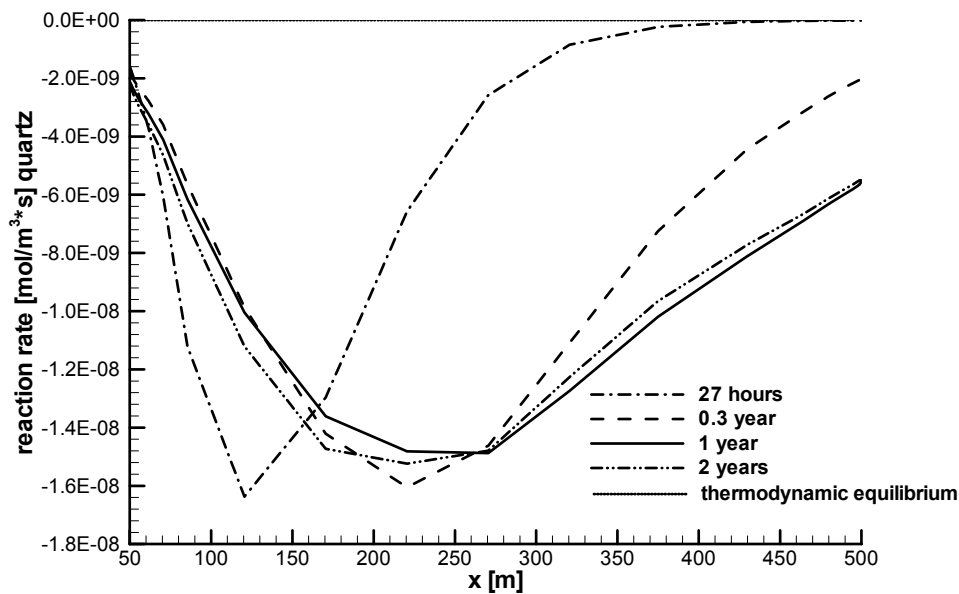


Figure 8-6: Temporal evolution of the quartz reaction rate in the fracture.

8.3.3 Pyrite precipitation

Finally, pyrite also behaves as predicted by the theoretical kinetic model of the Soultz system (chapter 4.4.4). Figure 8-7 proves this: pyrite precipitates due to the oversaturation resulting from the fluid injection at $T_{inj} = 65^\circ\text{C}$. Maximum precipitation occurs around 135°C (compare Figure 8-1). According to the temperature evolution, the area of maximum precipitation moves towards the production point. The maximum precipitation rate of $3.7 \cdot 10^{-12} \text{ mol/m}^3\text{s}$ is in good agreement with the rate of $4 \cdot 10^{-12} \text{ mol/m}^3\text{s}$ from Durst (2002) (chapter 5.5.3). However, no punctual dissolution events are found. Since pyrite reaction rates are much lower than the carbonate rates, the influence of the pyrite precipitation on the pH value is negligible.

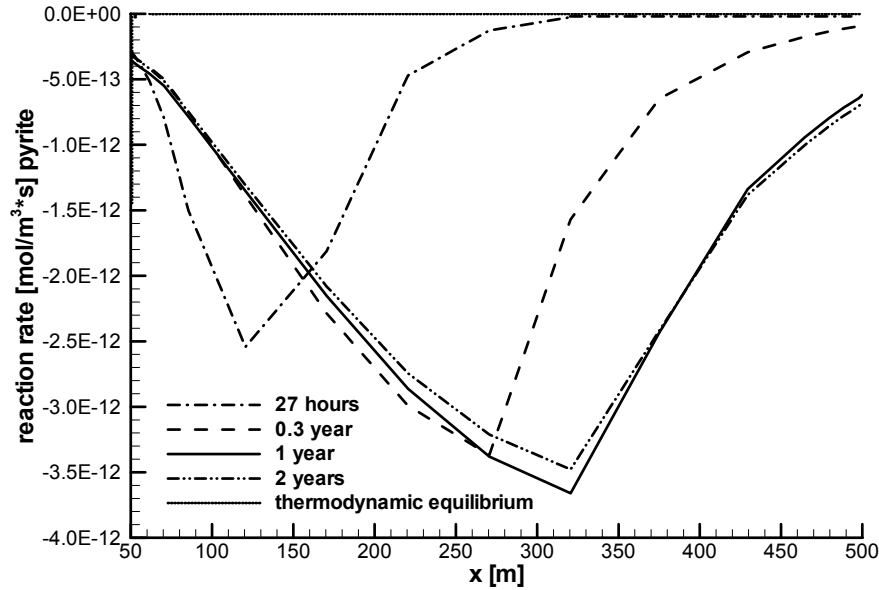


Figure 8-7: Temporal evolution of the pyrite reaction rate in the fracture.

8.3.4 Amount of dissolved and precipitated minerals

Based on the reaction rates, the amount of dissolved and precipitated minerals per element was calculated:

$$M_{i,E} = MW_i * V_E * \sum_{n=t_0}^{t_{tot}} (r_{i,n} * \Delta t)$$

Equation 8-1

$M_{i,E}$ is the amount of dissolved or precipitated mineral i in element E , MW is the molecular weight of mineral i , V_E the volume of element E , t_0 the initial time, t_{tot} the total simulation time, $r_{i,n}$ the reaction rate of mineral i at time n and Δt the time interval. Table 8-1 lists the initial amount for each mineral in the 21 fracture elements (see Figure 8-2), the amount of dissolved or precipitated minerals and the percentage of the initial mineral amount. Positive $M_{i,E}$ values indicate the dissolved and negative values the precipitated amount of minerals.

Table 8-1: Initial and dissolved or precipitated amount of minerals in each fracture element. Positive values represent dissolved and negative precipitated amount of minerals.

element number	element volume [m ³]	initial calcite [kg]	dissolved or precipitated calcite [kg]	initial dolomite [%]	initial dolomite [kg]	dissolved dolomite [kg]	initial quartz [%]	initial quartz [kg]	precipitated quartz [kg]	initial pyrite [%]	initial pyrite [kg]	precipitated pyrite [kg]	pyrite [%]
1	0.25	30.3	4.09	13.52	7.5	0.4	4.8	250.5	-1.7E-05	-6.8E-06	2.5	-5.5E-09	-2.2E-07
2	0.5	60.5	8.3	13.7	15.0	0.7	5.0	501.0	-3.6E-05	-7.2E-06	5.0	-9.6E-08	-1.9E-06
3	1	121.0	16.8	13.9	30.0	1.5	5.1	1002.0	-7.9E-05	-7.9E-06	10.0	-1.9E-10	-1.9E-09
4	2	242.0	34.3	14.2	60.0	3.2	5.4	2004.0	-1.8E-04	-9.2E-06	19.9	-1.5E-07	-7.5E-07
5	4	484.0	70.1	14.5	120.0	6.8	5.7	4008.0	-4.6E-04	-1.2E-05	39.8	-1.7E-07	-4.4E-07
6	5	605.0	89.4	14.8	150.0	8.8	5.9	5010.0	-7.8E-04	-1.6E-05	49.8	-3.9E-06	-7.7E-06
7	10	1210.0	177.8	14.7	299.9	17.3	5.8	10020.0	-2.4E-03	-2.4E-05	99.6	-8.6E-06	-8.6E-06
8	25	3025.0	382.4	12.6	749.8	33.8	4.5	25050.0	-9.2E-03	-3.7E-05	249.0	-8.9E-05	-3.6E-05
9	25	3025.0	203.4	6.7	749.8	17.5	2.3	25050.0	-1.0E-02	-4.1E-05	249.0	-6.6E-04	-2.6E-04
10	25	3025.0	-1.4	0.0	749.8	4.2	0.6	25050.0	-8.3E-03	-3.3E-05	249.0	-6.3E-04	-2.5E-04
11	25	3025.0	-113.1	-3.7	749.8	0.2	0.0	25050.0	-6.7E-03	-2.7E-05	249.0	-8.1E-04	-3.3E-04
12	25	3025.0	-214.6	-7.1	749.8	0.0	0.0	25050.0	-4.4E-03	-1.8E-05	249.0	-1.2E-03	-4.7E-04
13	29.5	3569.5	-303.8	-8.5	884.8	0.0	0.0	29559.0	-3.5E-03	-1.2E-05	293.8	-2.3E-03	-7.8E-04
14	25	3025.0	-266.5	-8.8	749.8	0.0	0.0	25050.0	-2.1E-03	-8.5E-06	249.0	-3.4E-03	-1.4E-03
15	10	1210.0	-111.4	-9.2	299.9	1.2	0.4	10020.0	-3.1E-04	-3.1E-06	99.6	-1.1E-03	-1.1E-03
16	5	605.0	-56.9	-9.4	150.0	1.1	0.7	5010.0	-1.6E-04	-3.2E-06	49.8	-6.9E-04	-1.4E-03
17	4	484.0	-47.0	-9.7	120.0	1.3	1.1	4008.0	-1.5E-04	-3.7E-06	39.8	-6.9E-04	-1.7E-03
18	2	242.0	-23.8	-9.8	60.0	0.8	1.3	2004.0	-7.7E-05	-3.8E-06	19.9	-3.9E-04	-1.9E-03
19	1	121.0	-12.0	-9.9	30.0	0.4	1.3	1002.0	-3.9E-05	-3.9E-06	10.0	-2.0E-04	-2.0E-03
20	0.5	60.5	-6.0	-9.9	15.0	0.2	1.4	501.0	-1.9E-05	-3.9E-06	5.0	-1.0E-04	-2.1E-03
21	0.25	30.3	-19.9	-9.9	7.5	0.1	1.0	250.5	-6.1E-06	-2.4E-06	2.5	-3.7E-05	-1.5E-03

The resulting amount of dissolved and precipitated minerals is given by the mineral reaction rates: calcite is the most reactive mineral in the system under consideration. The maximum dissolved percentage of the initial amount is 14.8 % and the precipitated amount is 9.9 %. 5.8 % is the maximum dissolved amount of dolomite as a percentage of the initial amount. The precipitated amount of quartz and pyrite is negligible compared to the carbonates because of their small reaction rates.

Table 8-2 lists the total amount of initial minerals, the total amount of dissolved and precipitated minerals as well as the percentage of the initial amount for one fractured zone. This table clearly shows that the biggest amount of dissolved and precipitated minerals is calcite. Thus, porosity and permeability changes are due to calcite reaction. The impact of the other minerals is negligible.

Table 8-2: Total initial and dissolved or precipitated amount of minerals in one fractured zone during 2 years.

mineral	total amount [kg]	dissolved amount [kg]	precipitated amount [kg]	dissolved percentage [%]	precipitated percentage [%]
calcite	27'225	990	1'180	3.6	4.3
dolomite	6'748	100	-	1.5	-
quartz	225'450	-	0.05	-	$2 \cdot 10^{-5}$
pyrite	2'241	-	0.01	-	$5 \cdot 10^{-4}$

To obtain the amount of dissolved and precipitated minerals in the whole reservoir (Table 8-3), the results from Table 8-2 were multiplied by the number of fractured zones (= 1250, see chapter 6.1.1). These results are compared to Table 5-1, which is the thermodynamic estimation of the maximum potential amount of mineral precipitation and dissolution that might occur when cooling the Soultz fluid from a temperature of 165°C to 65°C. Note that these results only account for 1 year, whereas Table 8-3 does for 2 years.

Table 8-3: Total dissolved or precipitated amount of minerals in the reservoir during 2 years.

mineral	dissolved amount [kg]	precipitated amount [kg]
calcite	1'237'500	1'475'000
dolomite	125'000	-
quartz	-	62.5
pyrite	-	12.5

Compared to Table 5-1, more than twice as much calcite is dissolved during two years. In contrast to the thermodynamic estimation, where no calcite precipitation was predicted, calcite is also dissolved in the present model. The amount of dissolved dolomite is about a third of the estimated amount, even for two years. Only a small amount of quartz and pyrite is precipitated compared to Table 5-1.

These differences arise from the diverse model assumptions used to calculate the amount of dissolved or precipitated minerals: the thermodynamic estimation did not take into account the interaction of the different minerals nor the kinetics, whereas these processes are all included in the present model. This comparison points out the importance of integrating the coupled interactions of minerals and kinetics when modelling the HDR reservoir

8.4 EVOLUTION OF POROSITY AND PERMEABILITY

The effect of the mineral reactions on the porosity is shown in Figure 8-8: the dissolution of calcite and dolomite near the injection well causes the porosity to increase. The calcite precipitation towards the production well leads to a porosity decrease. Since the precipitated amount of quartz and pyrite is orders of magnitudes smaller than the amount of precipitated calcite, the effect of quartz and pyrite is negligible. According to the evolution of the calcite reaction rate that decreases after 1 year, the increase of the porosity near the injection well (and the decrease towards the production well, respectively) from 1 to 2 years is smaller than up to 1 year. At the end of the simulation, the maximum porosity is 14.8 % and the minimum is 6.8 %, down from initially 10 %. These results are in good agreement with the data from Durst (2002) (chapter 5.5.3).

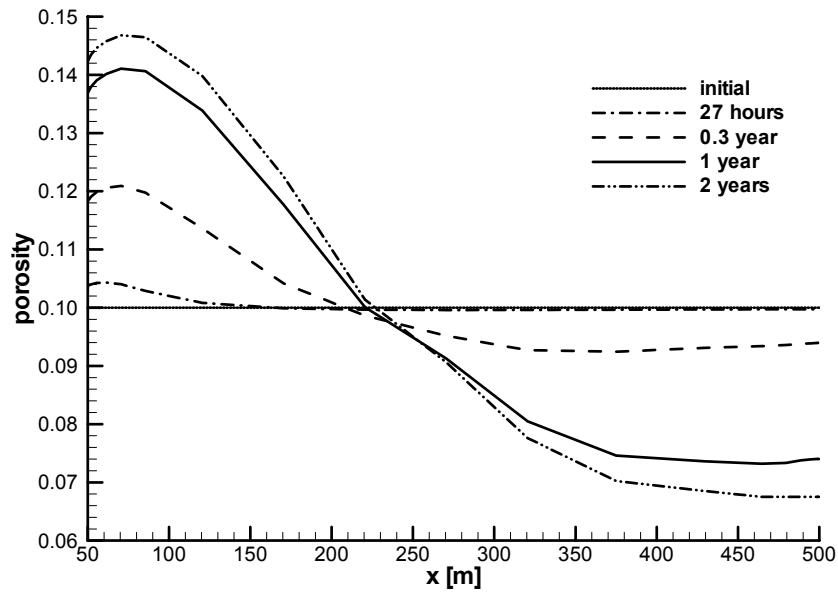


Figure 8-8: Temporal evolution of the porosity in the fracture.

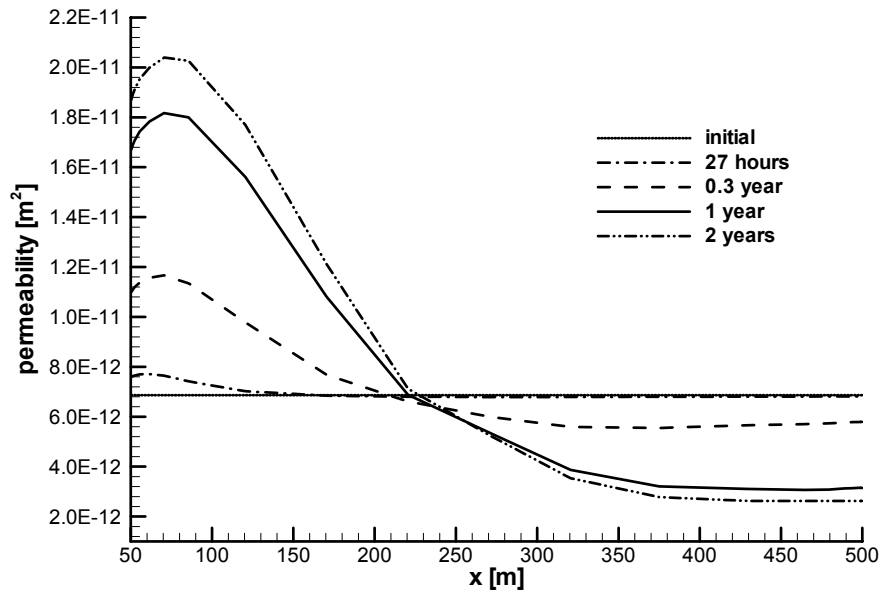


Figure 8-9: Temporal evolution of the permeability in the fracture.

The evolution of the permeability (Figure 8-9) is similar to the porosity: near the injection point, the permeability increases with simulation time due to calcite and dolomite dissolution. Towards the production point, the permeability is decreased because of calcite precipitation. Like the porosity evolution, the permeability increase near the injection well (and towards the production well) up to 1 year is four times as

large as between 1 and 2 years. The maximum permeability after 2 years is $2.1 \cdot 10^{-11} \text{ m}^2$ and the minimum is $3 \cdot 10^{-12} \text{ m}^2$, down from initially $6.8 \cdot 10^{-12} \text{ m}^2$.

Note that the evolution of the porosity and the permeability not only depends on the mineral reaction rates, but is also very much influenced by the porosity/permeability relation implemented in *FRACHEM*.

8.5 PRESSURE EVOLUTION AND FLUID VELOCITY

Figure 8-10 shows the pressure in the fractured zone at different time steps. The Neumann boundary conditions are reflected at the beginning of the simulation (100 seconds): at the injection point the pressure is 6 MPa and decreases towards the production well to 0 MPa. The further pressure development behaves according to the permeability evolution (Figure 8-9) that results from calcite dissolution and precipitation. The dissolution of calcite (see Figure 8-3) near the injection point causes the permeability (see Figure 8-9) to increase and therefore, the pressure in the fractured zone decreases at 27 hours. With increasing simulation time, the permeability near the production well decreases due to the precipitation of calcite, which leads to an increase in the pressure.

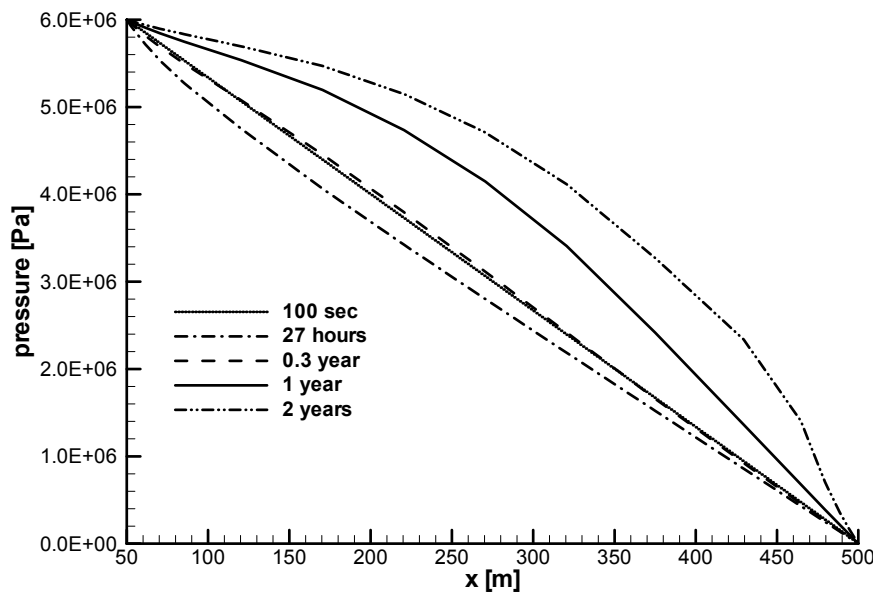


Figure 8-10: Pressure evolution in the fracture.

The initial fluid velocity of $3.8 \cdot 10^{-4} \text{ m/s}$ decreases with time, because of the permeability decrease near the production well. After 2 years, the fluid velocity is

decreased to $1.5 \cdot 10^{-4}$ m/s. Accordingly, the initial amount of injected fluid of 0.02 l/s decreases to 0.012 l/s after 2 years.

8.6 APPLICATION TO 1997 CIRCULATION TEST

To test the above findings, the numerical results were applied to hydraulic data measured during the 1997 circulation test. Since, in the numerical model, the pressure at the injection and the production point was fixed, pressure cannot be used for comparison. Instead, the transmissivity evolution was compared.

Figure 8-11 shows the pressure evolution at GPK1 (injection well) and GPK2 (production well) during the circulation test (from day 30 to 110) as well as the fluid injection and production rate. The pressure evolution at GPK1 is strongly influenced by the injection activities: sudden pressure drops are caused by shut-in stops during injection. This is clearly seen when comparing the injection rate with the pressure at GPK1. The pressure drop after 80 days is due to the injection stop of anti-scaling agent. The pressure decrease after each shut-in is assumed to be related to thermo-elastic processes such as tensile stresses due to the injection of cold fluid. The occurrence of thermo-elastic tensile stress at the injection well is a well-known effect (Kohl, 1992). Since, in the numerical model, no thermo-elastic processes are taken into account, effects from these processes have to be ignored in the measured data in order to compare with numerical data. Therefore, after 50 and 70 days, 10^5 Pa and $2 \cdot 10^5$ Pa (see fine arrows in Figure 8-11) were added on the measured pressure respectively, to compensate the thermo-elastic effects. The pressure after 85 days was set to the pressure value before the injection stop of anti-scaling agent (see fine arrow in Figure 8-11). Under these premises a pressure at GPK1 of 4 MPa resulted.

At GPK2 the pressure increases during the circulation test. Note that pressure evolution at production wells is usually plotted as drawdown pressure. In Figure 8-11 it is shown on the same axis like the pressure at GPK1 for better illustration. The production well is distant enough from GPK1, so that injection activities have no impact on the pressure evolution. Therefore, no sudden pressure drops occurred and the injection stop of anti-scaling agent has no impact on the pressure. In addition, since the temperature of the produced fluid is near the reservoir temperature (see Figure 8-1), no thermo-elastic effects are expected to occur.

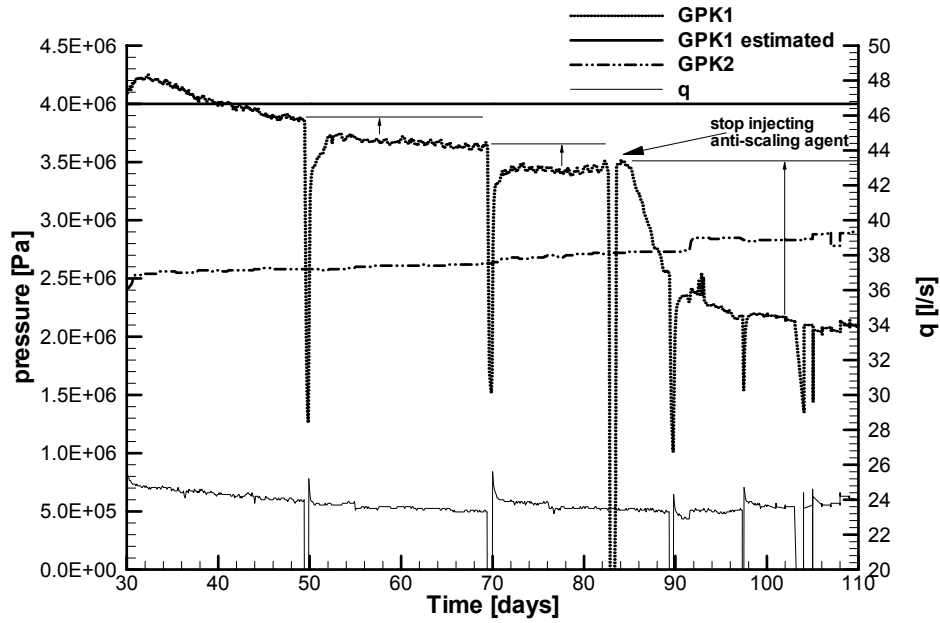


Figure 8-11: Fluid injection and production rate and pressure evolution during the 1997 circulation test. Time is days since 9th of July, when the test started. The fine arrows show the zones where the pressure at GPK1 was changed to neglect thermo-elastic effects.

The transmissivity Tr is calculated by (see also chapter 6.1.2, Equation 6-1):

$$Tr = \frac{q_{tot}}{L * \nabla P}$$

Equation 8-2

q_{tot} is the fluid production rate, L the depth of the fracture and ∇P the pressure gradient.

In the case of the numerical model, L is 10 m, ∇P is constant, since the pressure was fixed at the injection and the production point. q_{tot} is calculated by

$$q_{tot} = v_f * A_i * \Phi$$

Equation 8-3

v_f is the fluid velocity, A_i the area of the element interfaces and Φ the porosity.

To calculate the transmissivity evolution during the circulation test according to the numerical model, that is for a single fractured zone, the fluid injection rate is divided by the number of assumed fractured zones (chapter 6.1.1). ∇P is taken from the circulation data.

The resulting transmissivity evolution is illustrated in Figure 8-12. Due to different initial pressure conditions, the transmissivity in the numerical model is higher than that in the circulation test. However, the general trend is the same: the transmissivity decreases gradually with time. This is clearly seen when plotting the transmissivity evolution as a percentage of the initial value (Figure 8-13). The numerical results fit the circulation test very well. The outliers in Figure 8-12 and Figure 8-13 are due to the stop and shut-in activities.

The fact that the transmissivity in the circulation test decreases with time, when thermo-elastic effects are factored out, points to geochemical processes in the reservoir, such as the precipitation of calcite. The good fit between the transmissivity evolution of the numerical model and the 1997 circulation test confirms this assumption. The pressure evolution in the reservoir is therefore the result of interactions between thermo-elastic and geochemical processes.

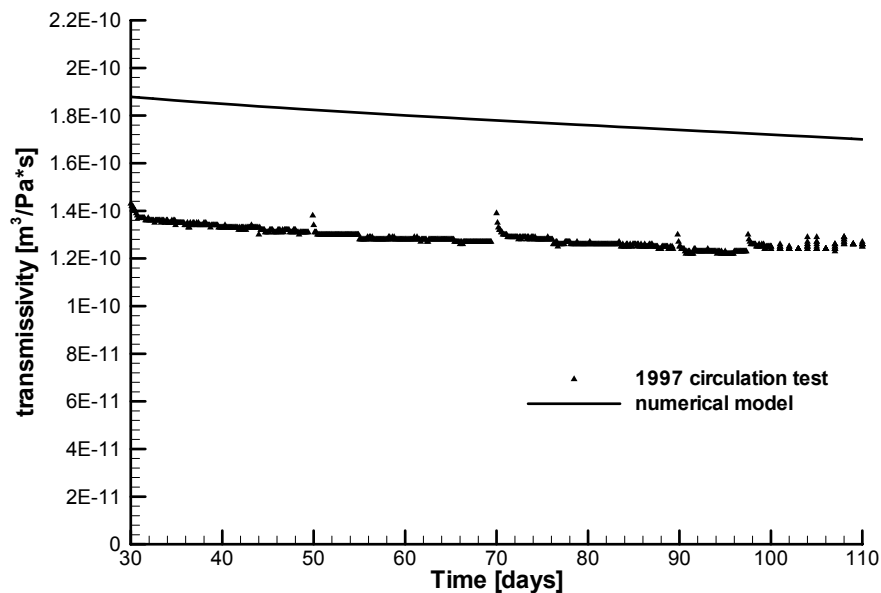


Figure 8-12: Comparison of the transmissivity evolution between the 1997 circulation test and the numerical results. Time is days since 9th of July, when the test started. The outliers in the circulation data are due to the stop and shut-in activities.

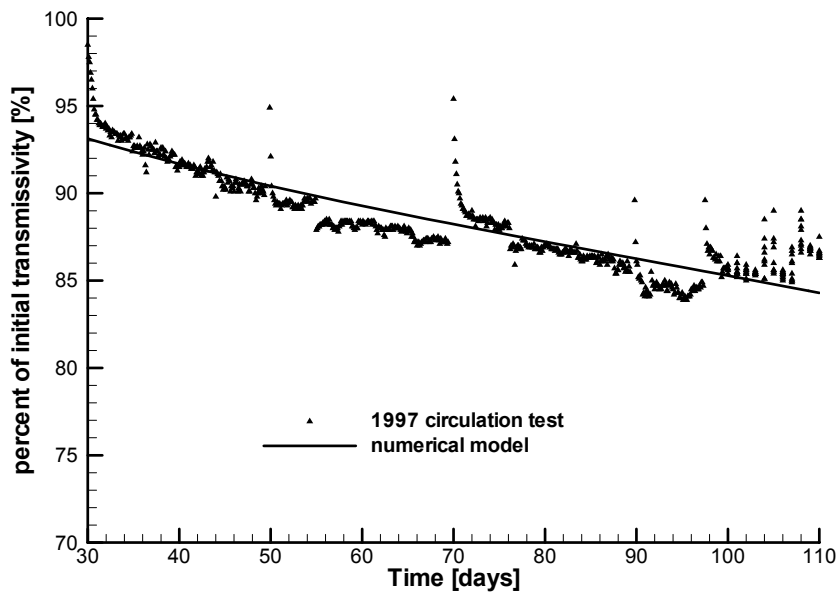


Figure 8-13: Comparison of the percentage of the initial transmissivity between the 1997 circulation test and the numerical results. Time is days since 9th of July, when the test started. The outliers in the circulation data are due to the stop and shut-in activities.

8.7 CONCLUSIONS

The long-term model of the HDR reservoir confirmed the theoretic kinetical modelling (chapter 4.4) that predicted the calcite to be the most reactive mineral. The changes in porosity and permeability are therefore due to the dissolution and precipitation of calcite. The impact of all other minerals can be neglected. After 1 year, the calcite reaction rate decreases, leading to a less distinct porosity and permeability change compared to the evolution before 1 year. The system seems to be very near to steady state. Thus, it is assumed that there will be no major changes in the porosity and the permeability, when calculating a time period of more than 2 years. The geochemical processes are not expected to be a limiting factor for the successful operation of the HDR concept at Soultz.

The results agree well with the results from Durst (2002) described in chapter 5.5.3, despite different model geometry and hydraulic parameters. Therefore, the chemical reactions seem not to be very sensitive to hydraulic processes and model geometry. As long as the temperature evolution is the same, similar reaction rates result. The presented model of the fractured zone leads to reasonable results, although it is only one of many possible reservoir models.

The comparison of the numerical results with the 1997 circulation test revealed that the geochemistry has an impact on the transmissivity. At the beginning of the circulation, the transmissivity decrease is faster (~5% in 20 days, see Figure 8-13) than with increasing simulation time (~10% in 100 days). It seems to asymptotically converge to a constant value. This agrees with the decrease of the calcite reaction rate with time (see Figure 8-3). Therefore, the transmissivity will probably not decrease much more during longer circulation periods.

The presented study covered a short period of time and focussed on the processes occurring at the production well. To be able to obtain more precise long-term predictions, longer time periods have to be modelled and the governing processes at the injection well have to be taken into account. This requires a more complex model, since it implies the integration of thermo-elastic effects.

The fact that geochemical impact is observed in the data of the 1997 circulation test highlights the importance of thermal, hydraulic and chemically coupled HDR reservoir models. The integration of geochemical considerations is therefore indispensable for integrated simulations of HDR systems and predictions of its performance.

9 CONCLUSION AND OUTLOOK

The presented work investigated the characteristics of the Soultz HDR reservoir and yielded important results towards understanding fluid-rock interactions as well as coupled thermal, hydraulic and chemical processes.

In the first part of the work, the regional and local temperature field in the Rhine Graben was investigated, to link the Soultz site to a greater context. For the first time, the temperature anomalies were studied by a 3D model focussing especially on the north-south trending faults in the Graben. It was found that the anomalies can be explained by large north-south trending convection systems within these faults. Not only the permeability of the fault and its width but also the fault's length and the model initial- /boundary conditions turned out to be crucial for the development and the size of convection cells. Careful treatment of model parameters as well as model geometry and initial-/boundary conditions is therefore of great importance when simulating convection systems. In addition, it was found that the graben-perpendicular fluid flux is negligible compared to the graben-parallel flux. This has to be taken into account when investigating temperature anomalies in the Rhine Graben. Moreover, such graben-wide features are important when delineating the general framework for HDR energy use at Soultz.

In the second part of the work, the coupled thermal, hydraulic and chemical processes in a fractured zone in the Soultz HDR reservoir were modelled for 2 years. Calcite turned out to be the most reactive mineral of the considered system consisting of calcite, dolomite, quartz and pyrite. During the 2 years, a total amount of 990 kg calcite (3.6% of the initial amount) are dissolved near the injection point leading to a

permeability increase from $6.8 \cdot 10^{-12} \text{ m}^2$ to $2.1 \cdot 10^{-11} \text{ m}^2$. Near the production well a total of 1'180 kg calcite (4.3% of the initial amount) are precipitated causing the permeability to decrease to $3 \cdot 10^{-12} \text{ m}^2$. After 2 years the systems seems to be very near to steady state. Therefore, it could be demonstrated, that mineral dissolution and precipitation during the circulation of the fluid in the reservoir does not represent a limiting factor on the HDR reservoir (at 3'500 m depth) performance at the Soultz site.

Comparing the coupled model results with the predictions from theoretical geochemical calculations, confirms that the complex interactions of the different processes can only be sized by numerical modelling. Moreover, the fact that geochemical impact is observed in the data of the 1997 circulation test, highlights the importance of thermal, hydraulic and chemically coupled HDR reservoir models. The integration of geochemical considerations is therefore indispensable for integrated simulations of HDR systems and for predictions of its performance.

The model simulated in this study represents simplified conditions of the Soultz HDR reservoir. To predict the long-term performance of the reservoir in greater detail, more complex models have to be set up. Several items should be improved:

- **Sensitivity to initial- and boundary conditions:** the initial- and boundary conditions were based on the 1997 circulation test and remained unchanged during the whole study. Since the conditions are estimations, several model runs should be done with slightly different conditions such as other injection rates or temperatures, to test the sensitivity. In addition, different model parameters should also be checked.
- **Simulation time:** since the reaction rates decrease with time, it was assumed that the system is near equilibrium after 2 years and that therefore, no major porosity change will occur any more. To confirm this assumption, the simulation time should be increased to the runtime of a HDR system (~30 years).
- **Deep reservoir:** the present study was based on the chemical composition of the 3'500 m deep reservoir, because only the geochemical monitoring data from the 1997 circulation test were available, when this study started. The target reservoir, however, is at 5'000 m depth. To take into account the actual chemistry of the Soultz HDR system, future models have to be based on the chemical composition of the 5'000 m deep reservoir.

- **Interaction of fractured zones:** in the present study, the coupled processes of a single fractured zone were investigated. In reality, the HDR reservoir consists of many such fractured zones. Depending on their distance and the relative exposure, these zones interact on each other. These interactions should be investigated to quantify the impact on the reservoir.
- **Complex model geometry:** the Soultz reservoir was assumed to consist of a regular sequence of fractured zones and intermediate matrix. All fractures in the zones were thought to be equally oriented. In reality, neither the sequences are regular nor are all fractures equally oriented. To represent a realistic reservoir model, a more complex geometry has to be shaped. Integrating additional data, such as seismic measurements, would help to delineate the fracture orientations and their occurrence.
- **3D model:** in the HDR system thermal, hydraulic and chemical processes take place not only horizontally but also in a vertical direction. Thus, future models have to be 3D.

The code *FRACHEM* was developed to simulate coupled thermal, hydraulic and chemical processes (including chemical kinetics) accounting for the specific Soultz conditions such as the high salinity of the reservoir fluid and the high temperatures. To our knowledge, there is at present only one other such code (*SHEMAT*; Clauser, 2003). Due to its special alignment to the Soultz conditions, which are mainly the implemented kinetic laws and the porosity-permeability relation for fractured rock, *FRACHEM* is more suitable to simulate the Soultz HDR reservoir. Sensitivity analyses and a benchmark with *SHEMAT* proved *FRACHEM* to be a reliable code. Unfortunately, the carbonate system implemented in *SHEMAT* cannot be used to model at temperatures higher than 90°C, whereas the temperatures in the Soultz HDR reservoir exceed 90°C. Therefore, a benchmark at a temperature of at least 165°C should be found. A percolation test with Soultz reservoir fluid circulating through a core sample consisting of Soultz granite would help to calibrate the thermodynamic and kinetic models of *FRACHEM*. Since the Soultz reservoir conditions (high temperature, pressure and fluid flow) are very difficult to simulate in the laboratory, some compromises have to be found.

The present *FRACHEM* is the first version. Future versions should be further developed to extend the possible applications:

- **Coupling method:** the implemented SNIA method turned out to be very sensitive to time steps both in *FRACHEM* and *SHEMAT*. For the present model with its high injection rate (0.02 l/s), small time steps (100 seconds) have to be chosen to prevent instabilities. This leads to very long calculation times. Therefore, the coupling methodology in has to be developed further to reduce the calculation time. Applying another coupling approach such as the one-step (global implicit) should be envisaged.
- **Porosity-permeability relation:** the fluid circulation in the Soultz system occurs in clusters of fractures and highly altered granite. Therefore, the implemented porosity-permeability relation is a combination of a fracture type porosity model of Northon & Knapp (1977) and a grain model after Bolton et al. (1996). The relation is a first attempt and has not yet been fully tested. Sensitivity analyses should be carried out to size the usability and to help in deciding if a more elaborate relation has to be developed.
- **Integration of other minerals:** at present calcite, dolomite, quartz and pyrite reactions can be modelled with *FRACHEM*. The lack of both a reliable analyses and a theoretical model to determine the aluminium concentration precluded the integration of clays and other minerals containing aluminium. But since clays are very abundant in the altered granite and significantly impact the permeability, an effort has to be made to find a way to integrate aluminium. This would allow taking clays and other aluminium minerals into account. For the sake of completeness other minerals also present in the Soultz granite, such as galena or chlorite, should be integrated.
- **Integration of redox reactions:** due to the absence of a correct model for iron redox reactions in the fluid, no iron oxides and oxy-hydroxides modelling is integrated in *FRACHEM*. However, to determine the impact on the reservoir of several items, such as the well casing, a model for iron oxides and oxy-hydroxides, including the redox state of aqueous iron should be developed.
- **Coupling with rock mechanical processes:** in the presented models, thermo-mechanical effects were neglected, although the comparison with the 1997 circulation test showed that such effects occur. To be able to size these effects, not only thermal and hydraulic but also rock mechanical processes should be coupled

with the chemistry. Since *FRACture* already provides the possibility to simulate thermal, hydraulic and rock mechanical processes, a lot of preparatory work has already been done.

Finally, since thermal, hydraulic and chemical couplings occur not only in HDR systems but also in other systems, *FRACHEM* can be used for a variety of other applications:

- **Radioactive waste disposal:** in many countries, disposal of spent fuel and other radioactive wastes in underground repositories is considered. An important part of the design and performance assessment of the disposal system is to consider the impact of thermal, hydraulic and chemical coupling on rock mass stability, groundwater flow, external stress, heat transfer and contaminant transport.
- **Oil and gas reservoirs:** coupled processes also play a role during oil recovery or may lead to the compaction or subsidence of reservoirs.
- **Geological systems:** reactive fluid flow coupled to thermal and hydraulic processes takes place in many geological systems such as in ore formations, glacial terrains or during compaction, diagenesis and metamorphism.
- **Geotechnical and environmental engineering:** coupled processes have to be accounted for in deep underground injection of liquid wastes, in permafrost and cold region engineering and modelling of dam reservoirs.

REFERENCES

- Anderson, G.M., Crerar, D.A., 1993. Thermodynamics in geochemistry: The equilibrium model. Oxford University Press, New York, 588p.
- Arvidson, R.S., Mackenzie, F.T., 1999. The dolomite problem; control of precipitation kinetics by temperature and saturation state. *American Journal of Science*, 299 (4), 257-288.
- Aquilina, L., Genter, A., Elsass, P., Pribnow, D., 2000. Evolution of fluid circulation in the Rhine Graben: Constraints from the chemistry of present fluids. In: Stober and Bucher (Eds.), *Hydrogeology of crystalline Rocks*, 117-203.
- Azaroual, M., 1992. Modélisation des interactions solutions hydrothermales-granite. Application au futur échangeur géothermique de type roche chaude sèches de Soultz-sous-Forêts, Alsace (France). Doc. BRGM 232, Orléans, France, 202p.
- Baria, R., Garnish, J., Baumgärtner, J., Gérard, A., Jung, R., 1995. Recent development in the European HDR research programme at Soultz-sous-Forêts (France). *World Geothermal Congress 1995*, Florence, Italy, 2631-2637.
- Bartels, J., Kühn, M., Schneider, W., Clauser, C., Pape, H., Meyn, V., Lajczak, I., 2002. Coore flooding laboratory experiment validates numerical simulation of induced permeability change in reservoir sandstone. *Geophysical Research Letters*, 29(9), 10.1029/2002GL014901.
- Bächler, D., Evans, K.F., Hopkirk, R., Kohl, T., Mégel, T., Rybach, L., 2001. Data analysis and controls towards understanding reservoir behaviour and the creation of a conceptual reservoir model. Federal Office for Education and Science, final report, project 98.0008-1, ETH Zurich, Switzerland, 203p.

- Bächler, D., Kohl, T., Rybach, L., 2003. Impact of graben-parallel faults on hydrothermal convection – Rhine Graben case study. *Physics and Chemistry of the Earth*, in press.
- Bear, J., 1979. *Hydraulics of Groundwater*. McGraw Hill.
- Benderitter, Y., Elsass, P., 1995. Structural control of deep fluid circulation at the Soultz HDR site, France: a review. *Geotherm. Sci. & Tech.*, 4(4), 227-237.
- Bethke, C. M., 1996. *Geochemical reaction modeling: Concepts and applications*. Oxford University Press, New York. 397p.
- Bolton, E.W., Lasaga, A.C., Rye, D.M., 1996. A model for the kinetic control of quartz dissolution and precipitation in porous media flow with spatial variable permeability; formulation and examples of thermal convection. *Journal of Geophysical Research, B, Solid Earth and Planets*, 1001 (10), 22, 157-187.
- Brinkmann, R., 1972. *Lehrbuch der Allgemeinen Geologie*, 2. Ferdinand Enke Verlag, Stuttgart.
- Brooks, A.N., Hughes, T.J.R., 1982. Streamline Upwind / Petrov-Galerkin formulations of convective dominated flows with particular emphasis on the incompressible Navier-Stokes equations. *Computer Methods in Applied Mechanics and Engineering*, 32, 199-259.
- Carslaw, H.S., Jaeger, J.C., 1959. *Conduction of Heat in Soils*. Oxford University Press.
- Chiang, W.H., Kinzelbach, W., 2001. *3D-Groundwater Modelling with PMWIN*. Springer Verlag, Berlin.
- Clauser, C., Kiesner, 1987. A conservative, unconditionally stable, second-order three point differencing scheme for the diffusion convection equation. *Geophysical Journal of the Royal Astronomical Society*, 91, 557-568.
- Clauser, C., 1988. Untersuchungen zur Trennung der konduktiven und konvektiven Anteile im Wärmetransport in einem Sedimentbecken am Beispiel des Oberrheintalgrabens. PhD thesis. *Fortschritts-Berichte VDI, Reihe 19, Nr. 28*, VDI Verlag, Düsseldorf.
- Clauser, C., Villinger, H., 1990. Analysis of convective and conductive heat transfer in a sedimentary basin, demonstrated for the Rhinegraben. *Geophys. J. Int.*, 100, 393-414.

- Clauser, C., 2003. SHEMAT and Processing SHEMAT - Numerical simulation of reactive flow in hot aquifers, Springer Verlag, Heidelberg, 332p.
- Davies, C.W., 1962. Ion Association. Butterworths, London.
- Davis, J.C., 1986. Statistics and Data Analysis in Geology. Second Edition. New York: John Wiley.
- Doebli, F., 1970. Die geothermischen Verhältnisse des Oelfeldes Landau/Pfalz. In: Graben Problems. Schweizerbart, Stuttgart, 110-116.
- Dove, P.M., 1994. The dissolution kinetics of quartz in sodium chloride solutions at 25 to 300°C. American Journal of Science, 294 (6), 663-678.
- Durst, P., Vuataz, F.D., 2000. Fluid-rock interactions in hot dry rock reservoirs - a review of the HDR sites and detailed investigations of the Soultz-sous-Forêts system. In: Proc. World Geothermal Congress 2000, Beppu-Morioka, Japan, May-June 2000, 3677-3682.
- Durst, P., Vuataz, F.D., 2001. Geochemical modelling of the Soultz-sous-Forêts Hot Dry Rock system. Brine-rock interactions in a deep hot fractured granite reservoir. 26th Workshop on Geothermal Reservoir Engineering, Stanford University, Stanford, USA, 11-20.
- Durst, P., 2002. Geochemical modelling of the Soultz-sous-Forêts Hot Dry Rock test site: Coupling fluid-rock interactions to heat and fluid transport. PhD thesis, University of Neuchâtel, Switzerland, 127 p.
- Edwards, A.L., 1972. TRUMP: a computer program for transient and steady-state temperature distributions in multidimensional systems. National Technical Information Service, National Bureau of Standards, Springfield, VA.
- Elsass P., Aquilina L., Beauce A., Benderitter Y., Fabriol H., Genter A., Pauwels H. 1995. Deep structures of the Soultz-sous-Forêts HDR site. Proc. World Geothermal Congress, Florence, Italy, 2543-2647.
- Fertl, W.H., Wichmann, P.A., 1977. How to determine static BHT from well-log data. World Oil, 184, 105-108.
- Flores-Marquez, E. L., 1992. Transferts de chaleur et de masse en milieu sédimentaire et fracturé. Modélisation numérique de la convection naturelle autour du site de Soultz (Graben du Rhin). PhD thesis. University of Nancy, INPL.

- Flores-Marquez, E.L., Royer, J.J., 1993. Convective heat transfer around the Soultz-s-Forêts geothermal site (Rhine Graben). Doc. BRGM 223, 5th International Symposium on Continental Scientific Drilling Programs, Paris, April 1992, 155-170.
- Gautelier, M., Oelkers, E.H., Schott, J., 1999. An experimental study of dolomite dissolution rates as a function of pH from -0.5 to 5 and temperature from 25 to 80°C. *Chemical Geology*, 157 (1-2), 13-26.
- Geiger, S., Matthai, S., Roberts, S., 2001. Complex Systems Platform: CSP3D3.0. <http://e-collection.ethbib.ethz.ch/cgi-bin/show.pl?type=bericht&nr=239>.
- Genter, A., 1990. Géothermie roche chaudes sèches.. Le granite de Soultz-sous-Forêts (Bas-Rhin, France). Fracturation naturelle, altérations hydrothermales et interaction eau-roche. Doc. BRGM 185, Orléans, France, 201 p.
- Genter, A., Traineau, H., 1992. Borehole EPS1, Alsace, France: Preliminary geological results from granite core analysis for HDR research. *Sci. Dril.*, 3, 205-214.
- Genter, A., and Traineau, H. 1996. Analysis of macroscopic fractures in granite in the HDR geothermal well EPS-1, Soultz-sous-Forets, France, *J. of Volcanology & Geothermal Res.*, Vol.72 (1-2), 121-141.
- Genter, A., Traineau, H., Artignan, D., 1997. Synthesis of geological and geophysical data at Soultz-sous-Forêts (France). Rapport BRGM R 39440, 36p.
- Gérard, A., Menjot, A., Schwoerer, P., 1984. L'anomalie thermique de Soultz-sous-Forêts. *Géothermie Actualités*, 3, 35-42.
- Gérard, A., Kappelmayer, O., 1989. Project Européen Roches Chaudes Sèches de Soultz-sous-Forêts. Résultats majeurs au 15 février 1989.
- Gérard A., and Kappelmayer, O. 1991. European HDR Project at Soultz-sous-Forêts, *Geothermal Sc. & Tech.*, 3(1-4), Gordon & Breach Science Publishers, New York, USA, 308p.
- Gérard, A., Baumgärtner, J., Baria, R., 1997. An attempt towards a conceptual model derived from 1993-1996 hydraulic operations at Soultz. NEDO Int. Geothermal Symposium, Sendai, Japan, 329-341.
- Greenberg, J.P., Moller, N., 1989. The prediction of mineral solubilities in natural waters: a chemical equilibrium model for the Na-K-Ca-Cl-SO₄-H₂O system to high concentration from 0 to 250°C. *Geochimica et Cosmochimica Acta*, 53, 2503-2518.

- Harvie, C.E., Moller, N., Weare, J.H., 1984. The prediction of mineral solubilities in natural waters: the Na-K-Mg-Ca-H-Cl-SO₄-OH-HCO₃-CO₃-CO₂-H₂O system to high ionic strengths at 25°C. *Geochimica et Cosmochimica Acta*, 48, 723-751.
- He, S., Morse, J.W., 1993. The carbonic acid system and calcite solubility in aqueous Na-K-Ca-Mg-Cl-SO₄ solutions from 0-90°C. *Geochimica et Cosmochimica Acta*, 57, 3533-3554.
- Helgeson, H.C., 1969. Thermodynamics of hydrothermal systems at elevated temperatures and pressures. *American Journal of Science*, 267 (7), 729-804.
- Helgeson, H.C., Kirkham, D.H., Flowers, G.C., 1981. Theoretical prediction of the thermodynamic behaviour of aqueous electrolytes by high pressures and temperatures; IV, Calculation of activity coefficients, osmotic coefficients, and apparent molal and standard and relative partial molal properties to 600°C and 5kb. *American Journal of Science*, 281 (10), 1249-1516.
- Horton, C.W., Rogers, F.T., 1945. Convective currents in a porous medium. *J. Appl. Phys.*, 16, 367-370.
- Hughes, T.J.R., 1987. *The finite element method*. Prentice Hall.
- Illies, J.H., 1965. Bauplan und Baugeschichte des Oberrheingrabens. *Oberrheinische Geologische Abhandlungen*, 20, 1-54.
- Jacquot, E., 1998. Description of the geothermal HDR site of Soultz-sous-Forêts (Bas-Rhin, France) based on data collected during previous stimulation and circulation experiments for a modelling purpose. Draft Proceedings of the 4th Int. HDR Forum, Strasbourg, 1998.
- Jacquot, E., 2000. Modélisation thermodynamique et cinétique des réactions géochimiques dans les réservoirs profonds. Application au site européen de recherche en géothermie profonde (Soultz-sous-Forêts, Bas-Rhin, France). PhD thesis, University Louis Pasteur, Strasbourg, France, 202 p.
- Katto, Y., Matsuoka T., 1967. Criterion for the onset of convection in porous medium. *Int. J. Heat Mass Transfer*, 10, 297-309.
- Kohl, T., 1992. Modellsimulation gekoppelter Vorgänge beim Wärmeentzug aus heissem Tiefengestein. PhD thesis. ETH Zürich, 149 p.
- Kohl, T., Medici, F., Rybach, L., 1994. Numerical simulation of radon transport from subsurface to buildings. *Journal of Applied Geophysics* (31) 145-152.

- Kohl, T., Hopkirk, R.J., 1995. "FRACTure" – A simulation code for forced fluid flow and transport in fractured, porous rock. *Geothermics*. 24 (3), 333-343.
- Kohl, T., 2000. FRACTure (V.3.1) Finite element program with WinFra (V.0.59) mesh generator, internal report.
- Kohl, T., Bächler, D., Rybach, L., 2000. Steps towards a comprehensive thermo-hydraulic analysis of the HDR test site Soultz-sous- Forêts. *Proc. World Geothermal Congress 2000, Kyushu-Tohoku, Japan, May-June 2000*, 2671-2676.
- Kohl, T., Signorelli, S., Rybach L., 2001. Three-dimensional thermal investigation below high Alpine topography. *Physics of the Earth and Planetary Interiors* (126) 195–210.
- Kohl, T., Brenni, R., Eugster, W., 2002. System performance of a deep borehole heat exchanger. *Geothermics* (31) 687-708.
- Krauskopf, K.B., Bird, D.K., 1995. *Introduction to geochemistry*. McGraw-Hill, Inc. New York, America, 647p.
- Kühn, M., 2003. Chemical Equilibrium Speciation for Brines at High Temperatures and Ionic Strength. In: Clauser, C., (ed). *SHEMAT and Processing SHEMAT - Numerical simulation of reactive flow in hot aquifers*, Springer Verlag, Heidelberg, 153-170.
- Lachenbruch, A.H., Brewer, M.C., 1959. Dissipation of the temperature effect of drilling a well in Arctic Alaska. *Geological Survey Bulletin*, 1083C, 73-109.
- Lapwood E.R., 1948. Convection of fluid in a porous medium. *Proc. Cambridge Phil. Soc*, 44, 508-521.
- Leblanc, Y., Lam, H.L., Pascoe, L.J., Jones, F.W., 1982. A comparison of two methods of estimating static formation temperature from well logs. *Geophys. Prosp.*, 30, 348-357.
- Le Carlier, Ch.; Royer, J-J., Flores, E. L., 1994. Convective heat transfer at the Soultz-sous-Forets geothermal site; implications for oil potential. *First Break*, 12 (11), 553-560.
- Lichtner, P.C., 1984. Continuum model for simultaneous chemical reactions and mass transport in hydrothermal systems. *Geochimica et Cosmochimica Acta*. 49.
- Meier, R., Hurtig, E., Ludwig, A., 1979. Fault tectonics and heat flow in Europe. In: V. Cermak and L. Rybach, *Terrestrial Heat Flow in Europe*. Springer Verlag, 112-118.

- Menjoz, A., Cautru, J.P., Criaud, A., Genter, A., 1988. Stimulation des réservoirs géothermiques en milieu cristallin. Caractérisation des réservoirs fracturés. In: Rapport Annuel d'Activités 1988. BRGM, France, 35-42.
- Murphy, H.D., 1979. Convective Instabilities in Vertical Fractures and Faults. *J. Geophys. Res.*, 84(B11), 6121-6130.
- Narashiman, T.N., Witherspoon, P.A., 1976. An integrated finite difference method for analysing fluid flow in porous media. *Water Resources Research*, 14(2), 255-261.
- Northon, D., Knapp, R., 1977. Transport phenomena in hydrothermal systems; the nature of porosity. *American Journal of Science*, 277 (8), 913-936.
- Pape, H., Clauser, C., Iffland, J., 1999. Permeability prediction for reservoir sandstones based on fractal pore space geometry. *Geophysics*, 64(5), 1447-1460.
- Pauwels, H., Fouillac, C., Criaud A., 1992. Water-rock interactions during experiments within the geothermal Hot Dry Rock borehole GPK1, Soultz-sous-Forêts, Alsace, France. *Applied Geochemistry*, 7, 243-255.
- Pauwels, H., Fouillac, C., Fouillac, A.M., 1993. Chemistry and isotopes of deep geothermal saline fluids in the Upper Rhine Graben; origin of compounds and water-rock interactions. *Geochimica et Cosmochimica Acta*, 57(12), 2737-2749.
- Parini, M., 1981. Geothermische Untersuchungen im Erdölfeld Landau/Pfalz (Oberrheingraben/Deutschland). PhD thesis. ETH Zürich.
- Pitzer, K.S., 1973. Thermodynamics of electrolytes. I. Theoretical basis and general equations. *Journal of Physics and Chemistry*, 12, 268-277.
- Pitzer, K.S., 1975. Thermodynamics of electrolytes. V. Effects of higher-order electrostatic terms. *Journal of Solution Chemistry*, 4, 249-265.
- Pitzer, K.S., 1991. Ion interaction approach: theory and data correlation. In: Pitzer, K.S. (ed), *Activity Coefficients in Electrolyte Solutions*, 2nd Edition, CRC Press, Boca Raton, 76-153.
- Plummer, L.N., Parkhurst, D.L., Fleming, G.W., Dunkle, S.A., 1988. A computer program incorporating Pitzer's equations for calculation of geochemical reactions in brines: U.S. Geological Survey Water-Resources Investigations Report, 88-4153, Reston Virginia.

- Pribnow, D., 1994. Ein Vergleich von Bestimmungsmethoden der Wärmeleitfähigkeit unter Berücksichtigung von Gesteinsgefügen und Anisotropie. Fortschritt-Berichte VDI. Reihe 19, Wärmetechnik/Kältetechnik, Nr. 75. PhD thesis. Düsseldorf.
- Pribnow, D., Kohl, T., Jung, R., Rybach, L., Clauser, C., 1999. The European HDR project in Soultz: an unconventional reservoir type? *Geothermal Research Council Transactions*, 18, 431-438.
- Pribnow, D., Schellschmidt, R., 2000. Thermal tracking of upper crustal fluid flow in the Rhine Graben. *Geophysical Research Letters*, 27(13), 1957-1960.
- Pruess, K., 1991. TOUGH2, a general-purpose numerical simulator for multiphase fluid and heat flow. Report LBL-29400. 102p.
- Rickard, D., 1997. Kinetics of pyrite formation by the H₂S oxidation of iron (II) monosulfide in aqueous solutions between 25 and 125°C; the rate equation. *Geochimica et Cosmochimica Acta*, 61 (1), 135-147.
- Rickard, D., Luther, G.W., 1997. Kinetics of pyrite formation by the H₂S oxidation of iron (II) monosulfide in aqueous solutions between 25 and 125°C; the mechanism. *Geochimica et Cosmochimica Acta*, 61 (1), 115-134.
- Rimstidt, J.D., Barnes, H.L., 1980. The kinetics of silica-water reactions. *Geochimica et Cosmochimica Acta*, 44 (11), 1683-1700.
- Rousset, D., Bayer, R., Guillon, D., Edel, J.B., 1992. Structure of the southern Rhine Graben from gravity and reflection seismic data (ECORPS-DEKORP Program). *Tectonophysics*, 221, 135-153.
- Sauty, J. P., 1981. Du comportement thermique des réservoirs aquifères exploités pour le stockage d'eau chaude ou la géothermie basse enthalpie. Thèse d'état, Grenoble.
- Schad, A., 1962. Das Erdoelfeld Landau. *Abh. Geol. Landesamt Baden-Wuerttemberg*, 4, 81-101.
- Schellschmidt, R., Schulz, R., 1991. Hydrogeothermic Studies in the Hot Dry Rock Project at Soultz-sous-Forêts. *Geothermal Science and Technology*, 221, 135-153.
- Schellschmidt, R., Pribnow, D., 2000. GGA Temperature Logs from the HDR Site in Soultz-sous-Forêts. Inst. für Geowissenschaftliche Gemeinschaftsaufgaben GGA Hannover. Internal report Nr. 0 120 448.

- Schulz, R., Schellschmidt, R., 1991. Das Temperaturfeld im südlichen Oberrheingraben. *Geol. Jahrbuch*, E 48, 153-165.
- Shiraki, R., Brantley, S.L., 1995. Kinetics of near-equilibrium calcite precipitation at 100°C; an evaluation of elementary reaction-based and affinity-based rate laws. *Geochimica et Cosmochimica Acta*, 59 (8), 1457-1471.
- Sjoberg, E.L., Rickard, D.T., 1984. Temperature dependence of calcite dissolution kinetics between 1 and 62°C at pH 2.7 to 8.4 in aqueous solutions. *Geochimica et Cosmochimica Acta*, 48 (3), 485-493.
- Smith, L., Chapman D.S., 1983. On the Thermal Effects of Groundwater Flow –1. Regional Flow Systems. *Journal of Geophysical Research*. 88(B1), 593-608.
- Steeffel, C.I., MacQuarrie, K.T.B., 1996. Approaches to modeling of reactive transport in porous media. In: Lichtner, P.C., Steefel, C.I., Oelkers, E.H. (EDS.), *Reactive transport in porous media. Reviews in Mineralogy*. 34, 83-129.
- Swenson, D., Hardeman, B., Butler, S., Persson, C., Thornton, C., 2002. Using the PetraSim pre- and post-processor for tough2, tetrad, and star. *Proceedings, Twenty-Seventh Workshop on Geothermal Reservoir Engineering*, Stanford University, Stanford, California.
- Traineau, H., Genter, A., Cautru, J.P., Fabriol, H., Chevremont, P., 1991. Petrography of the granite massif from drill cutting analysis and well log interpretation in the geothermal HDR borehole GPK1 (Soultz, Alsace, France). *Geothermal Science and Technology*, 3(1-4), 1-29.
- Trescott, P.C., Larson, S.P., 1977. Solution of the three-dimensional groundwater flow equation by using the strongly implicate procedure. *Journal of Hydrology* 35, 49-60.
- Werner, D., Parini, M., 1980. The Geothermal Anomaly of Landau/Pfalz: An Attempt of Interpretation. *J. Geophys.*, 48, 28-33.
- Werner, D., 1975. Probleme der Geothermik am Beispiel des Rheingrabens. PhD thesis. University Karlsruhe.
- White, S.P., 1995. Multiphase nonisothermal transport of systems of reacting chemicals. *Water Resources Research*. 31 (7), 1761-1772.
- Williamson, M.A., Rimstidt, J.D., 1994. The kinetics and electrochemical reate-determining step of aqueous pyrite oxidation. *Geochimica et Cosmichimica Acta*, 58 (24), 5443-5454.

- Wyllie, M.R.J., 1963. The fundamentals of well log interpretation. Academic Press, New York. 238 p.
- Xu, T., Pruess, K., 1998. Coupled Modelling of Non-Isothermal Multi-Phase Flow, Solute Transport and Reactive Chemistry in Porous and Fractured Media: 1. Model Development and Validation. Internal report, LBNL-42050, Lawrence Berkeley National Laboratory, Berkeley.
- Zhang, Y., Dawe, R.A., 2000. Influence of Mg^{++} on the kinetics of calcite precipitation and calcite crystal morphology. Chemical Geology, 163 (1-4), 129-138.

APPENDIX A

FRACHEM MANUAL

To run a model with *FRACHEM* three input files are required: *Input.dat*, *chem_input.dat* and *chem_dat*. The input and output files described below represent the format for *FRACHEM* version 1.0. Since *FRACHEM* is still in development, the input and output files may change in future versions.

FORMAT AND BUILDING OF FRACHEM INPUT FILES

Input.dat

Input.dat is the input file for the *FRACt*ure part of *FRACHEM* and is generated by *WinFra*. It contains the main information to run *FRACHEM*: execution control information, model geometry, element neighbourhood, solver information, time sequences, time steps, coupling information, boundary and initial conditions, load-time functions and sources. Table 1 lists an example of an *Input.dat* file. The file was partly chopped to save space. The points within the file such as in the third line after ‘COORDINATES’ show the places where the file was shortened. A detailed description of the *input.dat* format as well as the creation of *input.dat* by *WinFra* is given in Kohl (2000). To run a thermal, hydraulic and chemically coupled model the parameter ‘illinh’ (third line after ‘ELEMENT CONTROL CARD’) has to be set to 3.

chem.dat

chem.dat is the input file for the *CHEMTOUGH* part of *FRACHEM*. It contains all geochemical information. Table 2 illustrates an example of a *chem.dat* file. Since *chem.dat* is described in detail in Durst (2002), only a brief overview is given here.

The three entries in the first line are the maximum relative concentration variations allowed for a chemical species, the number of chemical outputs and the coupling parameter. If the coupling parameter is true (.T.), the porosity and permeability variation calculated in the chemical module is passed to *FRACture*. In contrast, if the coupling parameter is false (.F.), *FRACture* will not take into account these variations. In the second line the number of reactions, of species and of gas reactions are listed. However, gas reactions are not yet included in *FRACHEM*.

The following block (from H₂O to CO₃²⁻) contains the electrical charge, phase of species (L for liquid and S for solid), concentration in mol/kg, molecular weight in g/mol, volume mass of solid in kg/m³ and the coefficients for the calculation of the activity coefficients for each species in the system.

In the next block, the information on the reactions is listed (from CO₃²⁻ to INJ). The name of the reaction is indicated followed by the stoichiometric coefficients of the basis species in the reaction and the type of reaction on the next line. '1' indicates aqueous species, '4' solid species at equilibrium and '5' kinetic reactions. The following line lists the coefficients for the calculation of logK. On the last line, five rate data parameters for non-equilibrium reactions are listed: the reaction surface area (is calculated by *FRACHEM*), the proportion of mineral in grain type porous space, the ratio between grain permeability and fracture permeability, and the mineral number ('1' for quartz, '2' for calcite, '3' for dolomite and '4' for pyrite). The fifth parameter is not used in the current version and therefore set to zero.

The last block contains the information on the injection, production and surface installation volume. The first line after INJ and PROD indicates the number of injection and production wells, respectively. The following lines list the element number of the wells and the injection or production rates in m³/s. By setting a negative index for the injection rate, the rates are determined from the *FRACture* fluid velocities. After SURF the volume of the surface element, temperature and pressure are set. ENDFI indicates the end of *chem.dat*.

chem_input.dat

chem_input.dat is a file generated by WinFra. It contains the geometrical information the interface uses to calculate the fluid flow from element to element. Table 3 shows an example of a *chem_input.dat* file. The points within the file show the places where the file was shortened.

The first block lists the element numbers and their mid points. In the following, the element neighbourhood is indicated. The first two numbers are the connected elements. pt1x to pt3z are the co-ordinates of three points on the interface area.

FORMAT OF FRACHEM OUTPUT FILES**output.dat**

Contains a summary of the model set up as well as debugging information. Whenever a simulation fails to run, an error message is printed into *output.dat*. At the end of a successful simulation the computation time is printed. *Output.dat* is described in detail in Kohl (2000).

disX.dat

disX.dat contains for each node the co-ordinates, temperature and pressure at specified time steps. The first number in the TITLE indicates the number of the file (here X=3165) and the second the time in seconds. The temperature is given in °C and the pressure in Pa. The second block lists the element-node connections so that the file format is readable by the visualisation software *Tecplot*. Table 4 shows an example of a *disX.dat* file.

advX.dat and hflX.dat

The *advX.dat* and *hflX.dat* files contain the x-, y- and z-component of the velocity and the x-, y- and z-component of the heat flow at each element mid point, respectively. Again, the first number in the TITLE indicates the number of the file and the second number the time in seconds. The velocity is given in m/s and the heat flow in W/m². Also these files are readable by *Tecplot*. Table 5 and Table 6 illustrate examples of *advX.dat* and *hflX.dat* files.

chem_output.dat

The *chem_output.dat* lists the chemical results at specified time steps. The first line lists the time in seconds, the time in days, the number of chemical and transport iterations. Further, for all active elements and the surface element (element 0) the temperature in °C, pressure in Pa, porosity, permeability in m^2 , pH, Ca^{2+} concentration in mol/kg, Mg^{2+} concentration in mol/kg, HCO_3^- concentration in mol/kg and the reaction rates for quartz, calcite, dolomite and pyrite in $\text{mol/m}^3\text{s}$ are printed. Table 7 shows an example of a *chem_output.dat* file.

mon_node_elX.dat

To monitor the temporal evolution of the parameters for all active elements a *mon_node_elX.dat* is printed. The files contain the time in seconds, pressure in Pa, porosity, permeability in m^2 , pH, Ca^{2+} concentration in mol/kg, Mg^{2+} concentration in mol/kg, H_4SiO_4 concentration in mol/kg, HCO_3^- concentration in mol/kg, calcite concentration in mol/kg, dolomite concentration in mol/kg, quartz concentration in mol/kg, pyrite concentration in mol/kg and the quartz, calcite, dolomite and pyrite reaction rate in $\text{mol/m}^3\text{s}$. The file format is readable by *Tecplot*. Table 8 shows an example of a *mon_node_elX.dat* file. Unfortunately, the lines of the file are too long to be printed on one line.

Table 1: Example of an Input.dat file

```

0
* EXECUTION CONTROL CARD
* iexec iacode idebug irank ireadr iprtin iprtut iprtec
* 1 0 0 0 0 0 1
* DIMENSION CONTROL CARD
* numseq ndhist nsd numnp ngdof nlvect nltftn nptslf
* 3 0 3 238 2 2 2
* SOLUTION ALGORITHM CONTROL CARD
* ipcg isym ifact itmax tol
* 1 1 25 400 1.0E-08
* COUPLING CONTROL CARD
* numegh numegt numege iterh epsh itert epst itere epse
* 1 1 0 0 1.0E-02 0 1.0E-02 0 0
* TIME SEQUENCE CARDS
* n nstep ndprt nsprt nhplt dt
* 1 1 1 1 1 0.0E+00
* 2 1 0 1 1 0.0E+01
* 3 315360 315360 0 315360 1.0E+02 ! 1y
* HYDRAULIC COUPLING SEQUENCE CARDS
* n nthyd niter alpha beta gamma iterj relaxj epsil
* 1 0 1 0.0 0.0 0.0 0 0.8 1.0E-06
* 2 -1 1 0.0 0.0 0.0 0 0.8 1.0E-06
* 3 -1 1 0.0 0.0 0.0 0 0.8 1.0E-06
* TRANSPORT COUPLING SEQUENCE CARDS
* n nttrans niter alpha beta gamma iterj relaxj epsil
* 1 -1 1 0.0 0.0 0.0 0 0.8 1.0E-06
* 2 0 1 0.0 0.0 0.9 0 0.8 1.0E-06
* 3 1 1 0.0 0.0 0.9 0 0.8 1.0E-06
* MONITOR NODES
* Knr dof Spez
***** WINFRA DOESN'T CREATE MONITOR NODES YET ! *****
* COORDINATES
* Knr gen x(1,n) x(2,n) x(3,n)
* 1 0 245.50 0.00 0.00
* IDENTIFICATION OF BOUNDARY CONDITIONS
* n ne ng id1 id2 ...
* 15 15 1 1 1
* VALUES OF BOUNDARY CONDITIONS 1
* Knr gen f(1,n) f(2,n) ...
* 53 0 0 165
* VALUES OF BOUNDARY CONDITIONS 2
* Knr gen f(1,n) f(2,n) ...
* 15 0 2000000 165
* LOAD-TIME FUNCTION #1
* time Factor1 ...
* 0 1 1 0 0
* 1 1 1 0 0
* LOAD-TIME FUNCTION #2
* time Factor1 ...
* 0 1 1 0 0
* 1 1 0.39 0 0
* INITIAL CONDITIONS OF PRIMARY VARIABLES
0
* INITIAL CONDITIONS OF 1ST TIME DERIVATIVE OF PRIMARY VARIABLES
0
* HYDRO-THERM. ELEMENT GROUP #1
* 1100000012420000
* ELEMENT CONTROL CARD
* ntype numel numat iopt istprt nicode imass impexp nen
* 42 198 2 0 0 0 0 0 4
* nsurf1 ntran1 nvol1 nsout1 lfsur1 lfvoll ibuooy ilinh
* 0 0 0 0 1 1 0 3
* nsurf2 ntran2 nvol2 nsout2 lfsur2 lfvoll iadv nthema ilint
* 0 0 0 0 1 1 -1 0
* HYDRO - THERM. material properties
* Mat h-Cond1 h-Cond2 h-Cond3 St.coef. Poros. area
* xy-pitch xz-roll yz-yaw mol.Konz.
* Mat t-Cond1 t-Cond2 t-Cond3 rhocpf rhocpm Disp.x1 Disp.x2 area
* xy-pitch xz-roll yz-yaw Absorpt
* fracture
* 1 8.5E-08 8.5E-08 8.5E-08 0 1.0E-01 10
* 1 2.9E+00 2.9E+00 2.9E+00 4200000 2690000 0 0 10
* matrix
* 2 1.0E-15 1.0E-15 1.0E-15 0 0 10
* 2 3 3 3 4200000 2650000 0 0 10
* Z-COMPONENT
0 1 0
* ELEMENT CARDS
* El-nr Mat ien ...
* 1 1 1 2 3 4 0
* MONITOR ELEMENTs
* Eln Intp Komp.
***** WINFRA DOESN'T CREATE MONITOR ELEMENTS ! *****
+end

```

Table 2: Example of a chem.dat file

```

CHEM
10.0 5000. .T.
10 22 0
H2O      0.00 L 5.55000E+01 1.80000E+01 0.00000E+00
0.955608E+00 -0.268621E-04 0.389146E-06 -0.125171E-08 0.257202E-11
Na+      1.00 L 0.993      23.0000E+00 0.00000E+00
0.180993E+01 -0.411519E-01 0.544797E-03 -0.298645E-05 0.568416E-08
K+       1.00 L 80.8E-3    39.0000E+00 0.00000E+00
0.148302E+01 -0.316001E-01 0.419182E-03 -0.229938E-05 0.437243E-08
Ca++     2.00 L 0.159516415286035 40.0000E+00 0.00000E+00
0.137038E+01 -0.424256E-01 0.543639E-03 -0.292164E-05 0.552984E-08
H+       1.00 L 2.076904758232369E-005 1.00000E+00 0.00000E+00
0.294133E+01 -0.744534E-01 0.949630E-03 -0.508025E-05 0.956790E-08
Cl-      -1.00 L 1.460      35.45000E+00 0.00000E+00
0.171669E+01 -0.449296E-01 0.574913E-03 -0.308265E-05 0.581276E-08
HCO3-    -1.00 L 1.955364800518221E-003 61.0000E+00 0.00000E+00
0.149635E+01 -0.444200E-01 0.571479E-03 -0.308008E-05 0.583848E-08
SO4--    -2.00 L 1.158056567216048E-003 96.0000E+00 0.00000E+00
0.313601E+00 -0.104143E-01 0.131810E-03 -0.703870E-06 0.133359E-08
H4SiO4   0.00 L 2.169993588292079E-003 96.0000E+00 0.00000E+00
0.193092E+01 -0.268539E-01 0.337269E-03 -0.178498E-05 0.334362E-08
FE++     2.00 L .501E-3      55.8500E+00 0.00000E+00
0.343449E+00 -0.201020E-02 0.448980E-05 0.000000E+00 0.000000E+00
MG++     2.00 L 5.427374303509602E-003 24.3000E+00 0.00000E+00
0.396939E+00 -0.314796E-02 0.108163E-04 0.000000E+00 0.000000E+00
HS-      -1.00 L 7.203158217478084E-004 33.0000E+00 0.00000E+00
0.210969E-03 -0.507186E-05 0.877067E-07 -0.609429E-09 0.136579E-11
CO3--    -2.00 L 2.408319328817235E-007 60.0000E+00 0.00000E+00
0.205858E+00 -0.681574E-02 0.854205E-04 -0.452599E-06 0.852881E-09
OH-      -1.00 L 8.067465138890718E-007 17.0000E+00 0.00000E+00
0.163025E+01 -0.481896E-01 0.619779E-03 -0.333916E-05 0.632716E-08
Ca(HCO3)+ 1.00 L 2.648730012659696E-004 101.000E+00 0.00000E+00
0.137701E+01 -0.345803E-01 0.446597E-03 -0.240895E-05 0.455247E-08
CO2(aq)   0.00 L 3.800017250727105E-002 44.0000E+00 0.00000E+00
0.167784E+01 -0.131991E-01 0.170756E-03 -0.931070E-06 0.180041E-08
CaCO3(aq) 0.00 L 2.807560399191191E-006 100.000E+00 0.00000E+00
0.100000E+01 0.000000E+00 0.000000E+00 0.000000E+00 0.000000E+00
CASO4(AQ) 0.00 L 3.119885501764850E-004 136.000E+00 0.00000E+00
0.100000E+01 0.000000E+00 0.000000E+00 0.000000E+00 0.000000E+00
QUARTZ    0.00 S 167.0E+00    60.0000E+00 2.65000E+03
0.100000E+01 0.000000E+00 0.000000E+00 0.000000E+00 0.000000E+00
CALCITE   0.00 S 12.1E+00    100.0000E+00 2.71000E+03
0.100000E+01 0.000000E+00 0.000000E+00 0.000000E+00 0.000000E+00
DOLOMITE  0.00 S 1.63E+00    184.3000E+00 2.71000E+03
0.100000E+01 0.000000E+00 0.000000E+00 0.000000E+00 0.000000E+00
PYRITE    0.00 S .83E+00     119.8500E+00 5.00000E+03
0.100000E+01 0.000000E+00 0.000000E+00 0.000000E+00 0.000000E+00
CO3--     0.00 0.00 0.00 0.00 -1.00 0.00 1.00 0.00 0.00 0.00 0.00 0.00 1
0.106210E+02 -0.141799E-01 0.119948E-03 -0.377598E-06 0.563170E-09
OH-       1.00 0.00 0.00 0.00 -1.00 0.00 0.00 0.00 0.00 0.00 0.00 0.00 1
0.149397E+02 -0.427928E-01 0.221928E-03 -0.752711E-06 0.129450E-08
Ca(HCO3)+ 0.00 0.00 0.00 1.00 0.00 0.00 1.00 0.00 0.00 0.00 0.00 0.00 1
-0.009172E+01 0.377718E-02 -0.100084E-03 0.355916E-06 -0.566154E-09
CO2(aq)   -1.00 0.00 0.00 0.00 1.00 0.00 1.00 0.00 0.00 0.00 0.00 0.00 1
-0.657655E+01 0.122524E-01 -0.143343E-03 0.466424E-06 -0.666853E-09
CaCO3(aq) 0.00 0.00 0.00 1.00 -1.00 0.00 1.00 0.00 0.00 0.00 0.00 0.00 1
0.750075E+01 -0.218770E-01 0.865748E-04 -0.237638E-06 0.206620E-09
CASO4(AQ) 0.00 0.00 0.00 1.00 0.00 0.00 0.00 1.00 0.00 0.00 0.00 0.00 1
-0.207040E+01 -0.255960E-03 -0.654052E-04 0.314719E-06 -0.770838E-09
QUARTZ    -2.00 0.00 0.00 0.00 0.00 0.00 0.00 0.00 1.00 0.00 0.00 0.00 5
-0.450127E+01 0.230740E-01 -0.136254E-03 0.554763E-06 -0.955384E-09
0 .1 .1 1 0
CALCITE   0.00 0.00 0.00 1.00 -1.00 0.00 1.00 0.00 0.00 0.00 0.00 0.00 5
0.222690E+01 -0.154277E-01 0.866480E-05 0.164848E-07 -0.126807E-09
0 .1 .1 2 0
DOLOMITE  0.00 0.00 0.00 1.00 -2.00 0.00 2.00 0.00 0.00 0.00 0.00 0.00 5
0.340778E+01 -0.370318E-01 0.430942E-04 -0.191080E-07 -0.215571E-09
0 .1 .1 3 0
PYRITE    -1.00 0.00 0.00 0.00 0.25 0.00 0.00 0.25 0.00 1.00 0.00 0.00 5
-0.265025E+02 0.836345E-01 -0.427566E-03 0.142557E-05 -0.247958E-08
0 .1 .1 4 0
INJ
1
5 -1
PROD
1
21 -1
SURF
1000.0 65.0d0 0.0e6
ENDFI

```

Table 3: Example of a chem_input.dat file

CHEM.INPUT.DAT file: Created through WinFra									
Element mid points									
ENr.	1	0	ptx	pty	ptz				
	2	0	270.50	0.03	0.00				
	3	0	120.50	0.03	0.00				
			61.50	0.03	0.00				
198	0	543.25	83.05	.	0.00				
neighbourhood-----									
enr.1	enr.2	interface	ptlx	ptly	ptlz	pt2x	pt2y	pt2z	pt3x
1	11	5.0E-01	2.455E+02	0.0E+00	0.0E+00	2.455E+02	0.0E+00	1.0E+00	2.455E+02
1	14	5.0E-01	2.955E+02	0.0E+00	0.0E+00	2.955E+02	0.0E+00	1.0E+00	2.955E+02
1	22	5.00E+02	2.955E+02	5.0E-02	0.0E+00	2.455E+02	5.0E-02	0.0E+00	2.955E+02
195	196	3.40E+02	5.065E+02	6.605E+01	0.0E+00	5.065E+02	1.0005E+02	0.0E+00	5.065E+02
									6.605E+01
									1.0E+00

Table 4: Example of a disX.dat file

TITLE = " ein 3156 3.154E+07"									
VARIABLES= x, y z									
ZONE	T="	2-D Gitter	"n=	238,	e=	198,	et=quadrilateral,	f=fepoint	TEMP
2.45500000E+02				0.00000000E+00		0.00000000E+00	1	1.13111063E+06	1.31297778E+02
2.95500000E+02				0.00000000E+00		0.00000000E+00	2	9.08889227E+05	1.40087445E+02
2.95500000E+02				5.00000000E-02		0.00000000E+00	3	9.08889227E+05	1.40206635E+02
2.45500000E+02				5.00000000E-02		0.00000000E+00	4	1.13111063E+06	1.31446586E+02
9.55000000E+01				5.00000000E-02		0.00000000E+00	5	1.79777620E+06	9.15777066E+01
9.55000000E+01				0.00000000E+00		0.00000000E+00	6	1.79777620E+06	9.13337401E+01
1.45500000E+02				0.00000000E+00		0.00000000E+00	7	1.57555384E+06	1.07021006E+02
1.45500000E+02				5.00000000E-02		0.00000000E+00	8	1.57555384E+06	1.07235595E+02
5.75000000E+01				5.00000000E-02		0.00000000E+00	9	1.96666620E+06	7.00621408E+01
5.75000000E+01				0.00000000E+00		0.00000000E+00	10	1.96666620E+06	6.97808789E+01
5.50000000E+02				1.00050000E+02		0.00000000E+00	238	2.19437952E+05	1.65000000E+02

1	2	4
5	6	8
9	10	12
13	10	9
15	16	17
17	19	20
20	19	13
21	22	6
11	22	21
8	7	23
		24
226	179	181
		238

Table 5: Example of an *advX.dat* file

```

TITLE = " ein      2 0.00E+00"
VARIABLES = x,      y,
2.70500000E+02      2.50000000E-02
1.20500000E+02      2.50000000E-02
6.15000000E+01      2.50000000E-02
5.55000000E+01      2.50000000E-02
5.02500000E+01      2.50000000E-02
5.10000000E+01      2.50000000E-02
5.25000000E+01      2.50000000E-02
8.25000000E+01      2.50000000E-02
7.05000000E+01      2.50000000E-02
5.43250000E+02      8.30500000E+01

elemno,      adv1,      adv2,      adv3,
1      3.77776384E-03      -1.46925449E-12      0.00000000E+00
2      3.77778019E-03      7.53151253E-12      0.00000000E+00
3      3.77781620E-03      3.63957137E-11      0.00000000E+00
4      3.77782581E-03      4.75512818E-11      0.00000000E+00
5      3.77784252E-03      8.49381089E-11      0.00000000E+00
6      3.77783852E-03      1.30484998E-10      0.00000000E+00
7      3.77783298E-03      7.31587410E-11      0.00000000E+00
8      3.77779530E-03      1.31409615E-11      0.00000000E+00
9      3.77780629E-03      2.25264579E-11      0.00000000E+00
198      1.50861268E-13      -3.94017997E-13      0.00000000E+00

```

Table 6: Example of a *hflX.dat* file

```

TITLE = " ein      1 0.00E+00"
VARIABLES = x,      y,
2.70500000E+02      2.50000000E-02
1.20500000E+02      2.50000000E-02
6.15000000E+01      2.50000000E-02
5.55000000E+01      2.50000000E-02
5.02500000E+01      2.50000000E-02
5.10000000E+01      2.50000000E-02
5.25000000E+01      2.50000000E-02
7.05000000E+01      2.50000000E-02
1.70500000E+02      2.50000000E-02
5.43250000E+02      8.30500000E+01

elemno,      hfl1,      hfl2,      hfl3,
1      2.48975285E-08      8.71375505E-06      0.00000000E+00
2      1.42758687E-06      -7.36729362E-06      0.00000000E+00
3      1.06777241E-05      3.02399940E-05      0.00000000E+00
4      -8.89824854E-06      3.23111180E-05      0.00000000E+00
5      -3.11125234E-05      7.23014182E-06      0.00000000E+00
6      1.17661244E-05      -1.38609039E-05      0.00000000E+00
7      8.65010392E-06      5.08378207E-05      0.00000000E+00
8      -9.14802101E-07      -5.47928039E-05      0.00000000E+00
9      -6.32901163E-06      1.24491635E-06      0.00000000E+00
10      -2.16748488E-06      -2.52603286E-05      0.00000000E+00
198      8.71409611E-08      3.46016549E-08      0.00000000E+00

```

Table 7: Example of chem_output.dat file

Time =		10000			15112			110000		
El	Temp	Pressure	Porosity	Ca	Mg	Quartz	Calcite	Dolomite	Pyrite	HCO3-
0	65.000000	0.000000E+00	0.900000E+00	0.160096E+00	0.542737E-02	0.972289E-11	0.483636E-09	0.433350E-15	0.170166E-14	0.195549E-02
1	165.000000	0.102000E+07	0.100000E+00	0.160096E+00	0.542738E-02	0.966985E-11	0.485931E-09	0.433795E-15	0.169834E-14	0.195549E-02
2	165.000042	0.168667E+07	0.100000E+00	0.160096E+00	0.542738E-02	0.979564E-09	0.922567E-06	0.112413E-07	0.128540E-13	0.195559E-02
3	164.856628	0.194889E+07	0.100000E+00	0.160096E+00	0.542738E-02	0.278844E-08	0.171156E-05	0.884898E-07	0.181547E-13	0.195733E-02
4	162.446010	0.197556E+07	0.100001E+00	0.160096E+00	0.542737E-02	0.282164E-08	0.408275E-05	0.138441E-06	0.529876E-14	0.217099E-02
5	86.228921	0.199889E+07	0.100002E+00	0.160096E+00	0.542737E-02	0.971934E-08	0.237917E-05	0.87252E-07	0.124471E-13	0.204749E-02
6	125.282814	0.199556E+07	0.100001E+00	0.160096E+00	0.542738E-02	0.987294E-08	0.183280E-05	0.810448E-07	0.323971E-13	0.197198E-02
7	151.326174	0.198889E+07	0.100001E+00	0.160096E+00	0.542738E-02	0.102673E-10	0.47332E-09	0.429710E-15	0.173709E-14	0.195549E-02
8	164.999540	0.184222E+07	0.100000E+00	0.160096E+00	0.542738E-02	0.924061E-12	0.697634E-09	0.436762E-15	0.113182E-14	0.195549E-02
9	165.007385	0.190889E+07	0.100000E+00	0.160096E+00	0.542738E-02	0.973187E-11	0.484231E-09	0.43340E-15	0.170232E-14	0.195549E-02
10	164.999990	0.146444E+07	0.100000E+00	0.160096E+00	0.542738E-02	0.973187E-11	0.484231E-09	0.43340E-15	0.170232E-14	0.195549E-02
11	165.000002	0.124222E+07	0.100000E+00	0.160096E+00	0.542738E-02	0.971885E-11	0.484121E-09	0.433404E-15	0.170144E-14	0.195549E-02
12	165.000000	0.313335E+06	0.100000E+00	0.160096E+00	0.542738E-02	0.972507E-11	0.482330E-09	0.433253E-15	0.170167E-14	0.195549E-02
13	165.000000	0.555557E+06	0.100000E+00	0.160096E+00	0.542738E-02	0.972415E-11	0.482740E-09	0.433281E-15	0.170166E-14	0.195549E-02
14	165.000000	0.797779E+06	0.100000E+00	0.160096E+00	0.542738E-02	0.972304E-11	0.483236E-09	0.43323E-15	0.170163E-14	0.195549E-02
15	165.000000	0.511111E+05	0.100000E+00	0.160096E+00	0.542738E-02	0.972608E-11	0.482034E-09	0.433246E-15	0.170168E-14	0.195549E-02
16	165.000000	0.157779E+06	0.100000E+00	0.160096E+00	0.542738E-02	0.972571E-11	0.482177E-09	0.433252E-15	0.170168E-14	0.195549E-02
17	165.000000	0.911121E+05	0.100000E+00	0.160096E+00	0.542738E-02	0.972596E-11	0.482099E-09	0.433250E-15	0.170168E-14	0.195549E-02
18	165.000000	0.244448E+05	0.100000E+00	0.160096E+00	0.542738E-02	0.972617E-11	0.482003E-09	0.433245E-15	0.170168E-14	0.195549E-02
19	165.000000	0.111113E+05	0.100000E+00	0.160096E+00	0.542738E-02	0.972624E-11	0.481987E-09	0.433245E-15	0.170169E-14	0.195549E-02
20	165.000000	0.444452E+04	0.100000E+00	0.160096E+00	0.542738E-02	0.972628E-11	0.481979E-09	0.433244E-15	0.170169E-14	0.195549E-02
21	165.000000	0.000000E+00	0.100000E+00	0.160096E+00	0.542738E-02	0.972630E-11	0.481975E-09	0.433244E-15	0.170169E-14	0.195549E-02
Time =		110000			15112			110000		
El	Temp	Pressure	Porosity	Ca	Mg	Quartz	Calcite	Dolomite	Pyrite	
0	65.000000	0.000000E+00	0.900000E+00	0.160096E+00	0.542739E-02					
1	164.999835	0.102000E+07	0.100000E+00	0.160097E+00	0.542740E-02	0.987953E-11	0.422311E-08	0.836155E-15	0.163482E-14	0.195640E-02

Table 8: Example of mon_node_elX.dat file

VARIABLES=	time,	temperature,	pressure,	porosity,	permeability,	pH,	Ca++,	Mg++,	H4SiO4,	calcite,	dolomite,
quartz,	pyrite,	rate_quartz,	rate_calcite,	rate_dolomite,	rate_pyrite,	rate_pyrite,	HCO3-				
10000	165.000000	0.55557E+06	0.100000E+00	0.138889E-10	4.790066	4.790066	0.160096	0.005427	0.002170	12.100000	1.630000
0.167000E+03	0.830000E+00	-0.97241E-11	-0.482740E-09	-0.433281E-15	-0.170166E-14	-0.170166E-14	0.195549E-02				
110000	164.999996	0.55557E+06	0.100000E+00	0.138889E-10	4.790272	4.790272	0.160097	0.005427	0.002170	12.100000	1.630000
0.167000E+03	0.830000E+00	-0.96891E-11	-0.420913E-08	-0.835910E-15	-0.162274E-14	-0.162274E-14	0.195639E-02				
210000	165.000023	0.55557E+06	0.100000E+00	0.138889E-10	4.790503	4.790503	0.160097	0.005427	0.002170	12.100000	1.630000
0.167000E+03	0.830000E+00	-0.959768E-11	-0.127539E-07	-0.148639E-14	-0.153370E-14	-0.153370E-14	0.195741E-02				
310000	164.999926	0.55557E+06	0.999999E-01	0.138888E-10	4.790973	4.790973	0.160098	0.005427	0.002170	12.100000	1.630000
0.167000E+03	0.830000E+00	-0.963108E-11	-0.423126E-07	-0.340769E-14	-0.140653E-14	-0.140653E-14	0.195948E-02				
410000	164.999990	0.55557E+06	0.999996E-01	0.138887E-10	4.791372	4.791372	0.160099	0.005428	0.002170	12.100000	1.630000
0.167000E+03	0.830000E+00	-0.945343E-11	-0.814571E-07	-0.583884E-14	-0.129084E-14	-0.129084E-14	0.196125E-02				
510000	165.000183	0.55557E+06	0.999992E-01	0.138886E-10	4.791747	4.791747	0.160100	0.005428	0.002170	12.100000	1.630000
0.167000E+03	0.830000E+00	-0.910574E-11	-0.129717E-06	-0.883902E-14	-0.113327E-14	-0.113327E-14	0.196292E-02				
610000	165.000148	0.55557E+06	0.999987E-01	0.138884E-10	4.792098	4.792098	0.160101	0.005428	0.002170	12.100000	1.630000
0.167000E+03	0.830000E+00	-0.901507E-11	-0.184616E-06	-0.122912E-13	-0.101465E-14	-0.101465E-14	0.196449E-02				
710000	164.999853	0.55557E+06	0.999979E-01	0.138881E-10	4.792438	4.792438	0.160102	0.005428	0.002170	12.100000	1.630000
0.167000E+03	0.830000E+00	-0.922079E-11	-0.246413E-06	-0.162414E-13	-0.909310E-15	-0.909310E-15	0.196601E-02				
810000	164.999573	0.55557E+06	0.999968E-01	0.138877E-10	4.792891	4.792891	0.160103	0.005428	0.002170	12.100000	1.630000
0.167000E+03	0.830000E+00	-0.939917E-11	-0.341321E-06	-0.224529E-13	-0.753749E-15	-0.753749E-15	0.196804E-02				
910000	164.999557	0.55557E+06	0.999954E-01	0.138871E-10	4.793301	4.793301	0.160104	0.005428	0.002170	12.100000	1.630000
0.167000E+03	0.830000E+00	-0.925231E-11	-0.443347E-06	-0.293037E-13	-0.591980E-15	-0.591980E-15	0.196989E-02				
1010000	164.999863	0.55557E+06	0.999916E-01	0.138864E-10	4.793657	4.793657	0.160105	0.005428	0.002170	12.100000	1.630000
0.167000E+03	0.830000E+00	-0.871380E-11	-0.542657E-06	-0.361416E-13	-0.423771E-15	-0.423771E-15	0.197151E-02				

Dominique Bächler

Beckenhofstrasse 61, CH-8006 Zürich, Switzerland
 phone: +41 1 363 45 89
 Institute of Geophysics, HPP P 3
 ETH Hönggerberg, CH-8093 Zürich, Switzerland
 phone: +41 1 633 20 74
 e-mail: baechler@ig.erdw.ethz.ch
<http://www.gtr.geophys.ethz.ch/baechler/baechler.htm>
 Date of Birth: 13. July 1975
 Nationality: Swiss

Education

1988 - 1994	College: Kantonsschule Oerlikon Zürich, Matura (Type B, Latin)
1994 - 1999	Student at ETH Zürich, Earth Sciences, major subjects: Applied and Environmental Geophysics, Seismology, Geodynamics and Technical Mineralogy & Mineral Resources
11/1998 - 4/1999	Diploma thesis: 'The Use of Geographical Information Systems (GIS) in Aeroradiometrics: A Pilot Study'
4/1999	Diploma in Geophysics (Dipl. Natw. ETH)
4/1999 – 3/2003	PhD student at ETH Zürich, thesis: 'Coupled Hydraulic-Thermal-Chemical Modelling at the Soultz-sous-Forêts HDR Reservoir (France)'.

Publications

- Bächler, D.**, Evans, K., Hopkirk, R., Kohl, T., Mégel, T. and Rybach, L., 2001. Data analysis and controls towards understanding reservoir behaviour and the creation of a conceptual reservoir model. Federal Office for Education and Science, final report, project 98.0008-1, ETH-Zürich, Switzerland, 203p.
- Bächler, D.**, Kohl, T., Rybach, L., 2003. Impact of graben-parallel faults on hydrothermal convection – Rhine Graben case study. Physics and Chemistry of the Earth, in press.
- Kohl, T., **Bächler, D.**, Rybach, L., 2000. Steps towards a comprehensive thermo-hydraulic analysis of the HDR test site Soultz-sous-Forêts. In: Proc. World Geothermal Congress 2000, Kyushu-Tohoku, Japan, pp. 3459-3464
- Rybach, L., **Bächler, D.**, Bucher, B., Schwarz, G., 2002. Radiation doses of Swiss population from external sources. Journal of Environmental Radioactivity, 62, pp. 277-286.